The molecular landscape of developmental pausing in mammals

Inaugural-Dissertation
to obtain an academic degree
Doctor of Philosophy in Natural Science

Ph.D. in Natural Science

submitted to the Department of Biology, Chemistry, Pharmacy of Freie Universität Berlin

by
Dhanur Prakash Iyer

Berlin 2023

The work was performed at the Max Planck Institute for Molecular Genetics in Berlin between October 2018 and September 2023 under the supervision of Dr. Aydan Bulut- Karslioglu.

1st reviewer:
Dr. Aydan Bulut-Karslioglu
Department of Genome Regulation
Max Planck Institute for Molecular Genetics Ihnestraße 63-73, 14195 Berlin

2nd reviewer:
Prof. Dr. Sigmar Stricker
Department of Chemistry and Biochemistry Freie Universität Berlin
Thielallee 63, 14195 Berlin

Date of defense: 15/05/2024

Declaration of Independence:

Herewith I certify that I have prepared and written my thesis independently and that I have not used any sources and aids other than those indicated by me.

I have marked as such all statements that are taken literally or in content from other writings. This dissertation has not yet been presented to any other examination authority in the same or a similar form and has not yet been published.

Summary:

Many mammals can control the timing of birth by temporarily suspending development which is marked by a reduction of metabolic activity. This interruption in the development process is called diapause is specific to blastocyst-stage embryos and is an apparent response to tide over adverse environmental and nutritional conditions. The establishment of diapause is an active process involving extensive rewiring of the epigenetic, transcriptomic and metabolic landscape of the embryo. How the above three cellular processes are coordinately re-wired during dormancy entry is not known. Here I show that the regulatory function of miRNAs is indispensable for the mouse embryos entering into the diapause state. Without the miRNA function mouse ESCs and embryos suffer developmental collapse upon mTORi-mediated diapause induction. Small RNA sequencing of single mouse embryos showed specific miRNAs to be upregulated during diapause induction. *In silico* miRNA-protein network of diapause was developed by the integration of small RNA sequencing data together with computationally predicted miRNA targets. The network showed miRNA-mediated regulation of nuclear and cytoplasmic bodies along with RNA splicing which are perturbed in miRNA null mouse ESCs. The study also shows nutrient and autophagy regulator TFE3 to be the upstream regulator for the expression of dormancy-associated miRNAs, linking cytoplasmic mTOR activity to nuclear miRNA biogenesis.

It is unknown whether the capacity to pause is a conserved trait across mammals, more specifically in humans. Mouse and humans show similar patterns of mTOR expression during pre-implantation development, suggesting the involvement of the primordial pathway in blastocyst development and timing in both species. Here I show human blastoids and pluripotent cells in naïve and naïve-like states retain the capacity to pause via mTOR inhibition and the pausing is functionally reversible even at the molecular level.

Taken together the above findings suggest that the development of human embryos may be controllable and that miRNAs play a critical regulatory role in bringing transcriptional re-wiring in mouse embryos for successful entry into dormancy.

Zusammenfassung:

Viele Säugetiere können den Zeitpunkt der Geburt kontrollieren, indem sie die Entwicklung vorübergehend unterbrechen, was durch eine Verringerung der Stoffwechselaktivität gekennzeichnet ist. Diese Unterbrechung des Entwicklungsprozesses, die Diapause genannt wird, ist spezifisch für Embryonen im Blastozystenstadium und ist eine offensichtliche Reaktion auf die Überwindung ungünstiger Umwelt- und Ernährungsbedingungen. Die Etablierung der Diapause ist ein aktiver Prozess, der eine umfassende Neuverdrahtung der epigenetischen, transkriptomischen und metabolischen Landschaft des Embryos beinhaltet. Wie die oben genannten drei zellulären Prozesse beim Eintritt in die Ruhephase koordiniert neu verkabelt werden, ist nicht bekannt. Hier zeige ich, dass die regulatorische Funktion von miRNAs für den Übergang der Mausembryonen in den Diapause-Zustand unverzichtbar ist. Ohne die miRNA-Funktion erleiden Maus-ESCs und -Embryonen einen Entwicklungszusammenbruch bei der mTORi-vermittelten Diapause-Induktion. Kleine RNA-Sequenzierungen einzelner Mausembryonen zeigten, dass spezifische miRNAs während der Diapause-Induktion hochreguliert werden. In silico wurde das miRNA-Protein-Netzwerk der Diapause durch die Integration kleiner RNA-Sequenzierungsdaten zusammen mit rechnerisch vorhergesagten miRNA-Zielen entwickelt. Das Netzwerk zeigte eine miRNA-vermittelte Regulierung von Kern- und Zytoplasmakörpern sowie RNA-Spleißen, die in miRNA-Null-Maus-ESCs gestört sind. Die Studie zeigt auch, dass der Nährstoff- und Autophagieregulator TFE3 der vorgelagerte Regulator für die Expression von Ruhe-assoziierten miRNAs ist und die zytoplasmatische mTOR-Aktivität mit der nuklearen miRNA-Biogenese verknüpft.

Es ist nicht bekannt, ob die Fähigkeit zum Innehalten ein konserviertes Merkmal bei Säugetieren, insbesondere beim Menschen, ist. Maus und Mensch zeigen ähnliche Muster der mTOR-Expression während der Entwicklung vor der Implantation, was auf eine Beteiligung des primordialen Signalwegs an der Entwicklung und dem Timing der Blastozysten bei beiden Arten schließen lässt. Hier zeige ich, dass menschliche Blastoide und pluripotente Zellen in naiven und naiv-ähnlichen Zuständen über die mTOR-Hemmung die Fähigkeit behalten, eine Pause einzulegen, und dass die Pause sogar auf molekularer Ebene funktionell reversibel ist.

Zusammengefasst deuten die oben genannten Ergebnisse darauf hin, dass die Entwicklung menschlicher Embryonen kontrollierbar sein könnte und dass miRNAs eine entscheidende regulatorische Rolle bei der Neuverdrahtung der Transkription in Mausembryonen für den erfolgreichen Eintritt in den Ruhezustand spielen.

Abbreviations	Definations
TE	Trophectoderm
ICM	Inner cell mass
ZGA	Zygotic genome activation
PKC	Phospho kinase C
TF	Transcription factor
FGF	Fibroblast growth factor
YAP	Yes-associated protein
ESC	Embryonic stem cell
LIF	Leukemia inhibitory factor
GSK3	Glycogen synthase kinase 3
TGF	Tramsforming growth factor
IGF	Insulin growth factor
MAPK	Mitogen activated protein kinase
PSC	Pluripotent stem cell
mTORC	Mammalian target of rapamycin complex
RNA	Ribonucleic acid
DNA	Deoxyribonucleic acid
PKA	Protein kinase C
PKG	Protein kinase G
PI3K	Phosphotidylinositol-3-kinase
TSC2	Tuberous Sclerosis complex 2
TNF	Tumor necrosis factor
IVF	In vitro fertilization
GFP	Green fluroscent protein
IF	Immunofluorcence
DGCR8	DiGeorge Critical Region 8
EU	Ethyluridine
WB	Western blot
DE	Differential expression
PCA	Principal component analysis
GO	Gene ontology
EDG	Equivalent day of gesteation
PPI	Protein-protein interaction
PML	Promyelocytic leukemia
DDX6	Dead-Box helicase

PrE/PE	Primitive endoderm
TSS	Trnascription start site
TFBS	Transcription factor binding site
MEF	Mouse embryonic fibroblast

Table of Contents

Introduction

A. Mouse preimplantation development

Mammalian development starts from a fertilized egg called a zygote which through a series of cell divisions forms a blastocyst[1] **(Figure 1)**. Since development starts from a single-cell zygote, it has to perform a few important tasks 1) to increase cell numbers 2) to give rise to different cell types and 3) to induce cell polarity for lineage specification. The series of cell divisions undergone by the zygote gives rise to cells called blastomeres. The blastomeres undergoing cleavage divisions have longer S-phase and short variable G1 and G2 phases[2]. The blastomeres follow very tightly regulated lineage-specific events which lead to the formation of blastocysts at embryonic day (E) 3.5 **(Figure 1)**. The cells of the blastocyst go on to form either the trophectoderm (TE) cells, or inner cell mass (ICM) from which the epiblast and primitive endoderm (PrE) cells are derived. The fact that the zygotes give rise to both embryonic and extraembryonic cells demonstrates that they are totipotent[1,3].

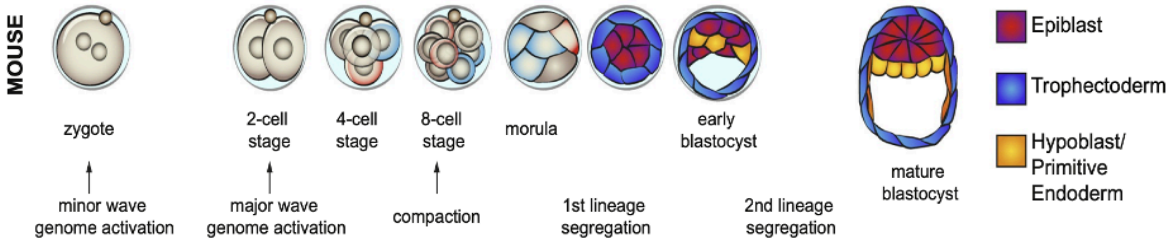

Figure 1. Early preimplantation development in mouse
Developmental journey of mouse embryo from single cell zygote to mature blastocyst. A major wave of ZGA occurs at the 2-cell stage (E1.5). Compaction and polarization take place at 8-cell stage (E2.5). The first lineage segregation between outer cells (future trophectoderm) and inner cells (future ICM) occurs at E3.5. At E4.5 the mouse embryo has matured into a blastocyst consisting of inner cell mass, primitive endoderm cells surrounding the ICM, outer trophectoderm cells and a blastocoel (Mole, Weberling and Zernicaka-Goetz., 2019).

A.1 Inside-outside polarity sets the stage for lineage specification in mouse embryo

The 8-cell stage embryo undergoes an event called compaction where there is an increase in cell-cell contact which promotes cellular adhesion[1,4]. This compaction event gives rise to apical-basal polarity in the 8-cell stage embryo (Figure 2A). The proteins that are responsible for the establishment of apical-basal polarity get asymmetrically localized either to the apical or basolateral ends of the embryo. Proteins such as Ezrin, atypical PKC (aPKC), protein kinase C (PKC), Par 3 (partitioning defective; Pard3), Par 6 (partitioning defective; Pard6a) are localized to the apical side of the compacted morula. E- cadherin and Par1 (partitioning defective 1b; Mark2) localize to the basolateral side of the cells[5–7] **(Figure 2B)**. Based on the orientation of the mitotic spindle with respect to apical-basal polarity, the cells of the morula

can undergo symmetric or asymmetric divisions which results in inside cells and outside cells of the blastocyst[8].

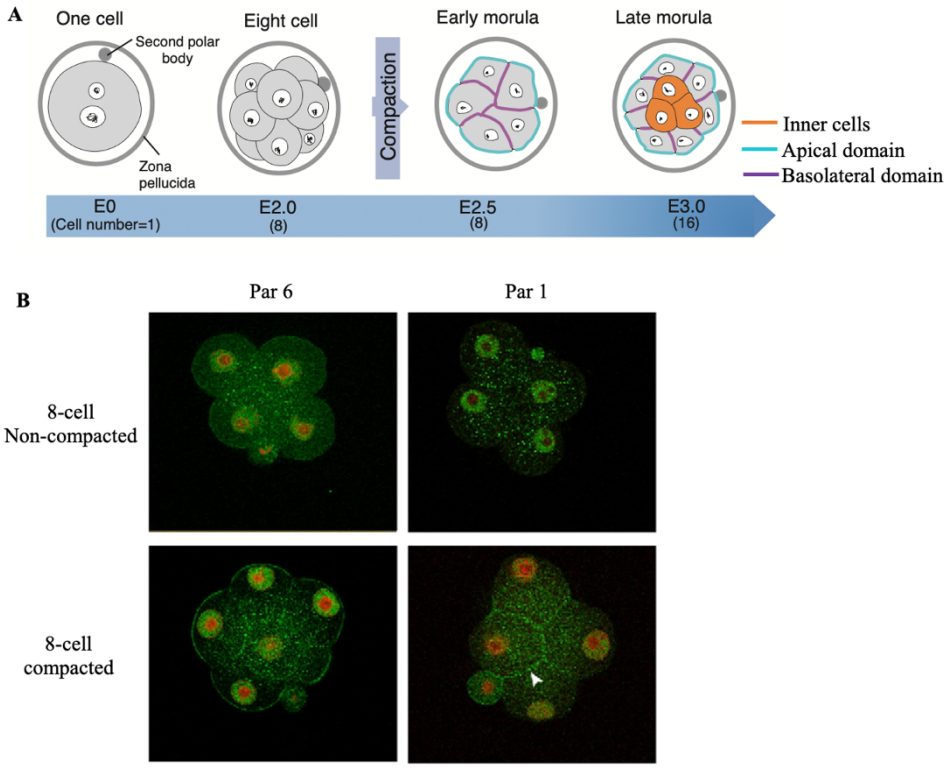

Figure 2. The compaction of early morula set the stage for the first lineage segregation
A. Compaction in early morula sets the apical-basal polarity. After a series of asymmetrical divisions, the apical-basal polarity generates inner cells and outer cells. Modified figure from (Takaoka and Hamada., 2012).
B. Immunofluorescence showing par 6 (green) and par 1(green) localized to the apical and basal side of the 8-cell compacted morula respectively. The nucleus is stained with propidium iodide (red) (Vinot et al., 2005).

A.2 Differential Hippo signaling in the inside cell and outside cell confers the start of lineage-specific gene expression

The above inside-outside leads to differential Hippo signaling which further contributes to cell fate specification. Hippo is a serine-threonine kinase that controls cell contact inhibition-mediated proliferation **(Figure 3)**. Hippo signaling is only active in the inside cell. Its activation leads to the phosphorylation of Yap1 which prevents its migration into the nucleus. In the absence of nuclear Yap1, its partner TEA domain family transcription factor 4 (Tead 4) is unable to activate its target genes. In the outside cells where the Hippo signaling is inactive, the unphosphorylated Yap1 is free to translocate into the nucleus, binds to Tead4 and activates TE-specific genes such as caudal-related homeobox 2 (*Cdx2*). Genetic ablation of Tead4 in mouse embryos prevents TE cell specification [9–13].

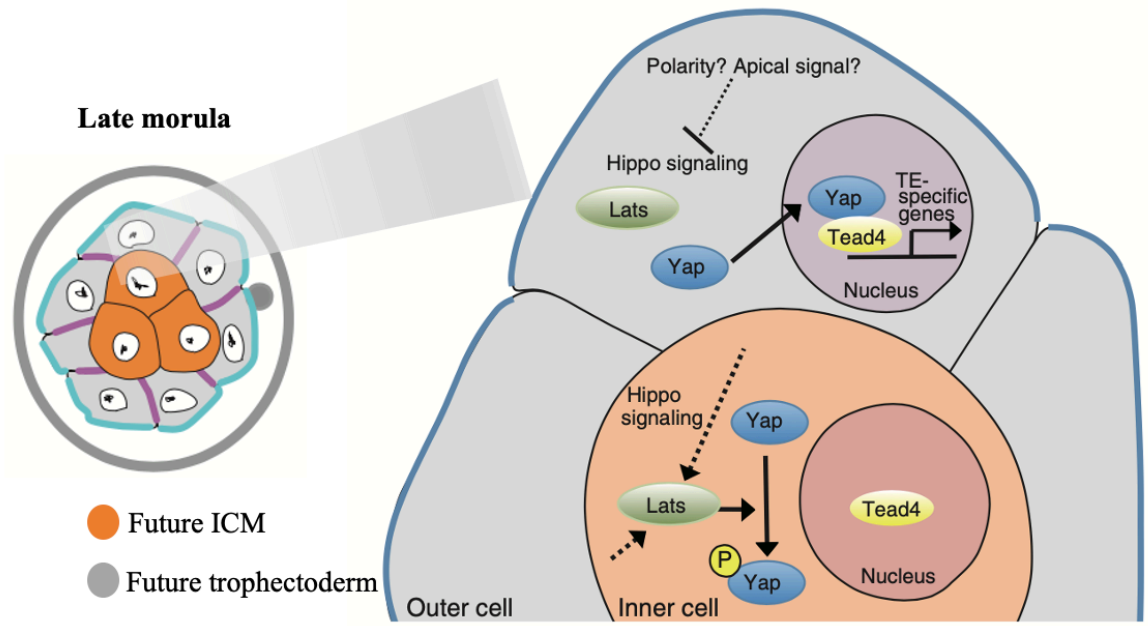

Figure 3. Cell position-dependent activation of Hippo signaling mediates lineage specification. The inside-outside polarity activates Hippo signaling only in the inside cell which phosphorylates Yap1 and prevents Tead4 from functioning inside the nucleus. In the outside cells, Hippo signaling is suppressed. Unphosphorylated Yap1 translocates into the nucleus, binds to Tead4 and activates TE-specific gene *Cdx2*. This defines inner cells as future ICM and outer cells as future trophectoderm in mouse embryos. Modified figure from (Takaoka and Hamada., 2012).

A.3 The reciprocal expression pattern of Cdx2 and Oct3/4 segregates TE and ICM cell fate

The embryo by E3.5 develops into a blastocyst having the outer TE and inner ICM. *Cdx2* is the TE cell marker. *Oct3/4* and *Nanog* marker for ICM. These transcription factors (TFs) show dynamic expression patterns between morula and blastocyst stages[14,15] **(Figure 4A)**. *Cdx2* expression is restricted to the outer cells from early morula until the blastocyst stage. Whereas *Oct3/4* is expressed throughout in early and late morula stage embryo. Until this stage, there is no reciprocal relationship between these 2 TFs. As development proceeds, *Cdx2* remains restricted to the outer cells which is future TE. The *OCT3/4* expressions become confined to inner cells which becomes the future ICM. This reciprocal expression pattern of *Cdx2* and *Oct3/4* is achieved by the operation of double negative- feedback loops that are mediated by the transcription factors **(Figure 4B)**. Zygotic *Cdx2* mutants in embryos give rise to cells that express *Oct3/4* but morphologically resemble TE cells[16]. Similarly, downregulation of *Oct3/4* or ectopic overexpression of *Cdx2* results in cells differentiating into TE lineage[15].

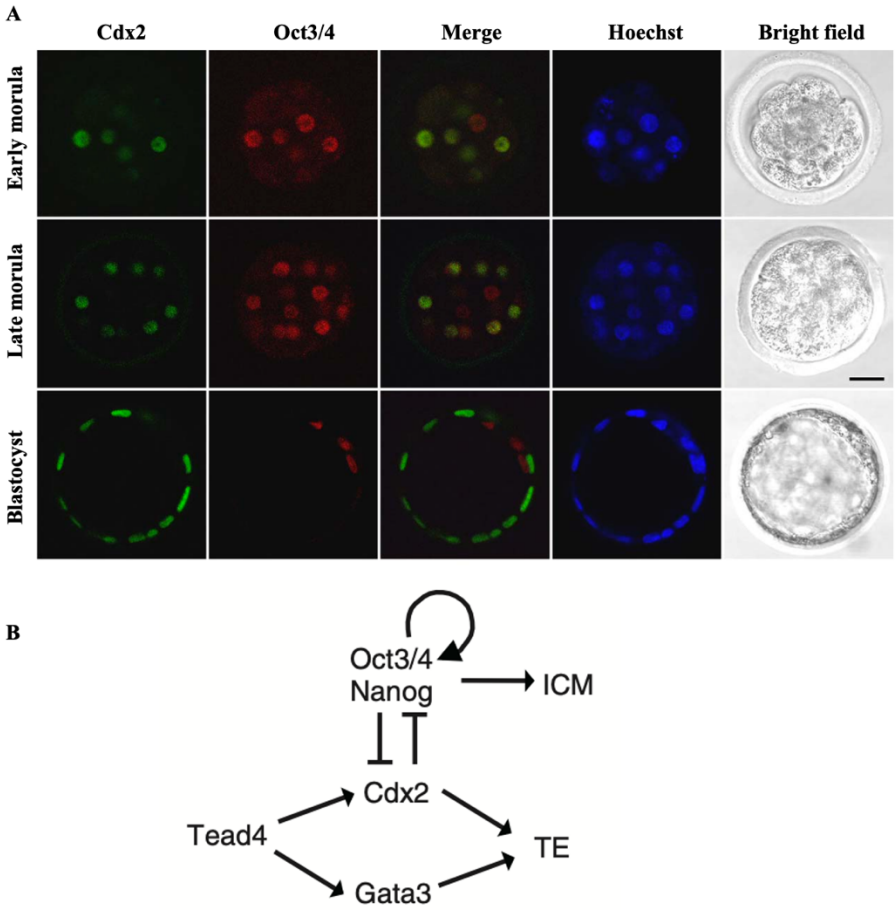

Figure 4. Determination of trophectoderm cell fate. A. Confocal images of mouse embryos from the early morula stage till the blastocyst stage. Oct3/4 (red) expression is dynamic and is expressed throughout early to late morula stage embryos, whereas Cdx2 (green) is restricted to outside cells. The dynamic Oct3/4 expression seen in morula stage embryos is lost when the embryos develop into a blastocyst. Oct3/4 is expressed by the inside cells and Cdx2 is expressed only in the outside cells (Niwa et al., 2005) **B.** A schematic of a double negative feedback loop between Oct3/4-Nanog and Cdx2 ensures that Cdx2 expression is restricted to trophectoderm cells, while the expression of Oct3/4-Nanog is progressively confined to the cells of the ICM (Takaoka and Hamada., 2012).

At E3.5, the TE and ICM cells show differences in histone methylation. In the ICM cells the levels of H4K8ac and H3K4me3 – epigenetic marks associated with active chromatin are enriched in the promoter region of Oct3/4 and the promoter region is less enriched for H3K9me2. This is inverse in TE cells where the promoter of Cdx2 is enriched for the above 2 activation marks[17]. The levels of H3R17me and H3R26me are different in TE and ICM cells. Cells that show higher H3R17me and H3R26me tend to acquire ICM cell fate while those cells that show lower expression of the above 2 marks tend to go towards TE specification[18,19].

A.4 Segregation of ICM into epiblast and primitive endoderm

In early E3.5 blastocyst embryos, the ICM cells express both the markers for epiblast (*Oct3/4* and *Nanog*) and PrE (Gata6). Even the transcriptome of these individual cells is indistinguishable[20]. In late-stage E4.5 embryos, the ICM cells segregate into 2 distinct populations. This lineage segregation is driven by FGF signaling[21,22]. PrE cells express FGFR2/3/4 receptors and are receptive to FGF signaling that drives its specification. On the other hand, the cells that form the epiblast are unresponsive to FGF signaling[20]. Loss of the above FGFR2 receptor compromises PrE formation[23,24] and loss of FGFR4 exhibits a mosaic pattern of expression of PrE markers Gata6 and Sox17[25].

FGF signaling has a strong influence on PrE specification. Modulating the FGF signaling in early blastocyst culture influences ICM cell fate specification. Pharmacological inhibition of FGF/Erk signaling specifies ICM cells towards epiblast lineage. On the other hand, exogenous supplementation of the culture with FGF2/4 directs the ICM cells toward PrE fate[20,26]. The start of PrE specification from ICM cells is not random. During the first wave of asymmetric cell division, the cells that get internalized are biased for epiblast specification.

In the second wave of asymmetric division, the internalized cells specify *Gata6* and *Sox17* and are biased for PrE specification[27]. A different study showed via lineage tracing that the cells that originate in the first and second wave of asymmetric division are bipotent and have the ability to acquire epiblast or PrE cell fates[28].

There is a regulatory mechanism at exists between PrE cells and cells of the epiblast. The cells that receive the FGF signal when they get committed to PrE fate, that cell induce a later inhibitory effect on their neighboring cell **(Figure 5)**. *Fgf4* expression is predominantly shown by epiblast cells and *Fgf2r* expression increases in cells with PrE fate[29]. The mechanism of relocation of PrE cells in late E4.5 blastocyst to the surface of the ICM facing the blastocoel remains unknown. Studies show that *Dab2* (disabled homolog 2) mutant embryos are unable to sort the PrE cells to the surface of the ICM[30]. It is speculated that Dab2 and Lrp2 which are expressed in the apical surface of PrE cells get polarized according to embryonic-abembryonic position which allows for cell-autonomous cell sorting[31]. Apart from the described scenario, there are other positional signals that emanate from the cells surrounding the blastocoel cavity that direct the positioning of the cells. Wnt9a which is expressed from the surrounding cells of the blastocoel cavity facilitates the sorting or repositioning of Gata4 cells[32,33]. The cells that do not reposition correctly undergo apoptosis.

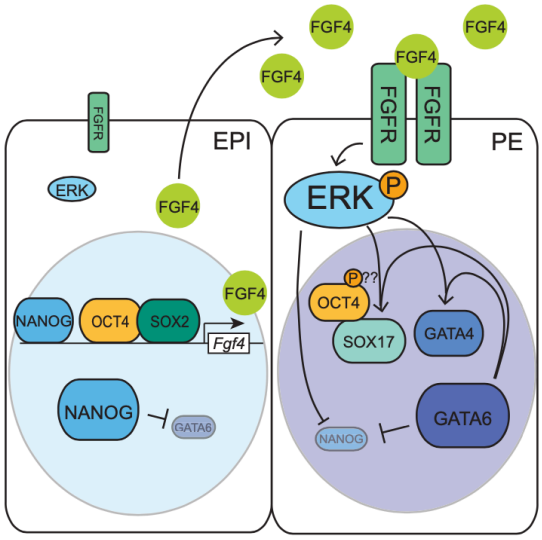

Figure 5. Specification of primitive endoderm (PE) cells by FGF4 signaling. The epiblast cells express high levels of FGF4 which suppresses GATA6 expression in these cells. The secreted FGF4 binds to FGF receptors of neighboring cells and upregulates GATA6. FGF signaling together with GATA6 cooperatively activates downstream target genes SOX17 and GATA4 (Chazaud and Yamanaka., 2016).

B. Differences in preimplantation development in mice and humans

The preimplantation development in mouse and humans is relatively similar with the zygote undergoing a series of cleavage divisions leading to an increase in cell number, while an overall constant volume is retained. Although the preimplantation stages are similar, there is a slight delay in the timing of development of human embryos when compared to that of a mouse **(Figure 6)**. The difference can also be seen in the timing of zygotic genome activation (ZGA). In mouse, the minor wave occurs in the late zygotic stage and the major wave happens in the 2-cell stage. In humans, the minor wave happens at the 4-cell stage and the major wave happens in the 8-cell stage[34,35]. In mouse although the blastomeres appear morphologically similar, their heterogeneity in cell fate can be seen in the 2-cell stage[36–38] and 4-cell stage[39]. This heterogeneity has been seen at the epigenetic level[18] and relates to changes in gene expression that influence cell fate specification. In humans, whether the above heterogeneity is exhibited in blastomeres remains to be addressed. Another difference between mouse and human preimplantation development is the timing of blastomere compaction. In mouse, the compaction starts at the 8-cell stage. Whereas in humans this process occurs asynchronously at the 8-16 cell stage[40] **(Figure 6)**.

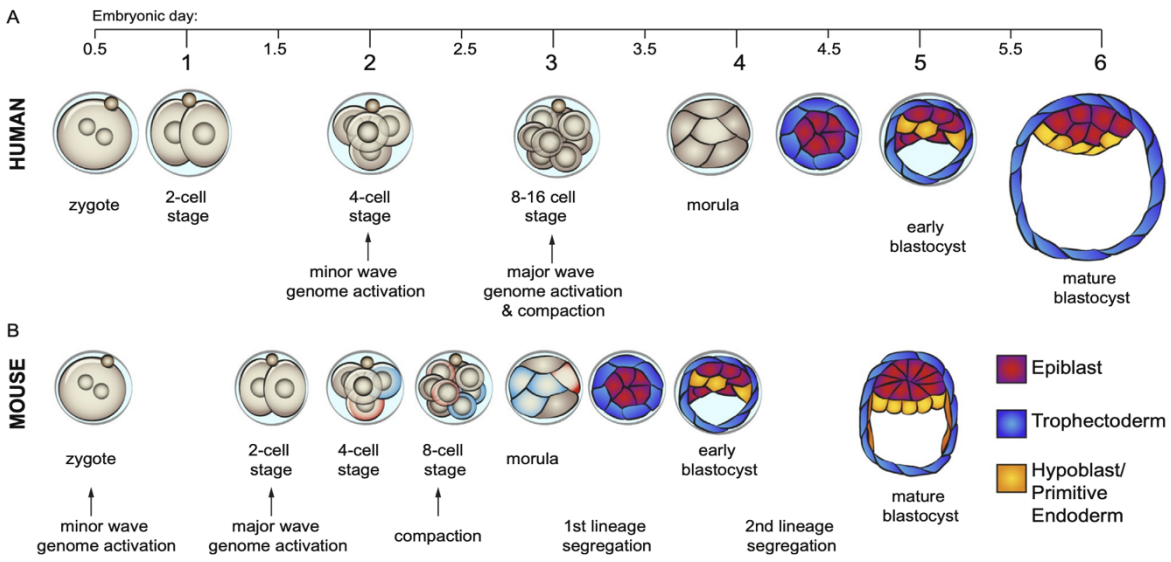

Figure 6. Pre-implantation development in human and mouse embryos. There is a delay in preimplantation development in humans when compared to mouse. Between the two species, there is a difference in the timing of ZGA activation and compaction of morula where in humans it's delayed and occurs in the 8-cell stage and 8-16 cell stage respectively. Due to this initial delay, the following events of lineage segregation proceed slowly in comparison to mouse embryos (Mole, Weberling and Zernicaka-Goetz., 2019).

B.1 Differences during first lineage segregation

In mouse, the lineage specification of trophectoderm and ICM is dependent on the differential Hippo/YAP signaling in the outer and inner blastomeres. The outer cells inhibit Hippo signaling that localizes YAP in the nucleus to induce the expression of *Cdx2* – a trophoblast marker. The inner cells sequester YAP in the cytoplasm that drives the expression of key pluripotent genes – *Oct4*, *Nanog* and *Sox2*. In humans, whether such regulatory signaling exists, remains to be investigated. In humans, it has been shown that Oct4 is the main driver not only for epiblast specification but also for driving Cdx2 expression. In humans, the initiation of trophoblast occurs independently of Cdx2 expression and only gets upregulated after the formation of blastocyst[41,42]. This is in sharp contrast to mouse pre-implantation development, suggesting a differential mechanism from the one in the mouse may govern first lineage segregation in human embryo.

B.2 Difference during second lineage segregation

A major difference exists during the second lineage segregation in mouse and human embryos. In mouse the initial waves of cell internalization bring heterogeneity in ICM cells. The cells internalized during the first wave express high FGF4 ligands and the cells internalized in the second wave express high FGF receptors. The FGF4 ligands activate FGF/ERK signaling in cells expressing FGF receptors. Thus, specifying PrE cells expressing *Gata6*. In humans, the distinct profile of epiblast and hypoblast (equivalent of mouse PrE) appears to arise after blastocyst formation. The separation of mature hypoblast is more evident only in the late human blastocyst upon initiation of implantation, where they downregulate *Oct4* and upregulate

hypoblast marker *Sox17*.[43] Inhibition of FGF/ERK signaling in human embryos does not prevent hypoblast formation. Indicating that different molecular signaling exists in specifying hypoblast cells[44,45].

C. Differences in early post-implantation development events in mouse and human embryo

Upon implantation, the blastocyst establishes contact with the maternal epithelium. This attachment to the maternal epithelium is mediated by the trophoblast cells. During this time two major trophectoderm populations can be distinguished. The trophectoderm in direct contact with ICM is the polar trophectoderm and the trophectoderm surrounding the blastocoel cavity is called mural trophectoderm.

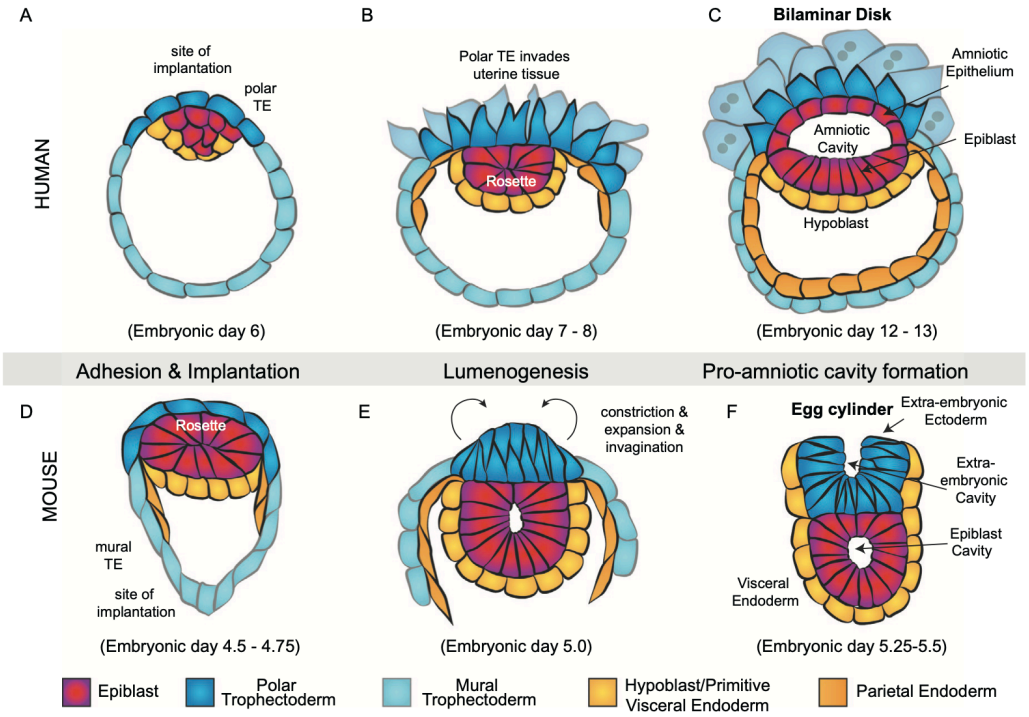

Figure 7. Post-implantation morphogenesis in human and mouse embryos. The first step of post-implantation is the same in human and mouse where the epiblast undergoes epithelialization and adopt a rosette configuration **(B and D)**. A central cavity forms within the epiblast cells of the human which later forms an amniotic cavity surrounded by squamous amniotic epithelium and columnar-shaped epiblast. The embryo acquires a bilaminar disk shape morphology with epiblast on top and hypoblast at the bottom **(C)**. In mouse, the epiblast cavity expands. The polar trophectoderm acquires a columnar shape and invaginates to form the extra-embryonic trophectoderm **(E)**. The extra-embryonic trophectoderm further expands forming an extra-embryonic cavity. Both the extraembryonic cavity and epiblast cavity expand further and eventually unite to form an egg cylinder **(F)** (Mole, Weberling and Zernicaka-Goetz., 2019).

In mouse the blastocyst implantation to the maternal epithelium is mediated by the mural trophectoderm and takes place at E4.5-4.75 **(Figure 7)**. At this time Cdx2 in the mural TE gets downregulated in contrast to polar TE. As a result, the mural TE loses its multipotency and undergoes epithelial-to-mesenchymal transition. The mural TE differentiates into trophoblast giant cells and acquires an invasive character[46]. In humans, the above process of blastocyst

attachment is mediated by polar trophectoderm and occurs between E7 and 8[47,48]. After attachment, the polar trophectoderm proliferates and differentiates into cytotrophoblast and multinucleated syncytiotrophoblast cells that penetrate the maternal endothelium[49,50]. In contrast to humans, the mouse polar trophectoderm does not participate in implantation and retains its multipotent characteristic due to the activation of FGF signaling secreted by the epiblast cells[51].

As the embryo implants, there is a major transcriptional and morphological changes that take place within the embryonic compartment. The epiblast transitions from naïve pluripotency to a state of primed pluripotency[52]. This transition in pluripotency is required for induction of epithelization and lumen formation[53,54]. Formation of the pro-amniotic cavity in mouse is a two-step process and differs significantly from human embryos. The first step is conserved between mouse and human and involves rosette configuration within the epiblast[53]. The second step occurs only in mouse and involves the formation of a second cavity where there is an apical invagination of the extra-embryonic ectoderm at the proximal site of the embryo **(Figure 7 E and F)**. The two cavities, one in the extra-embryonic ectoderm and the other in the epiblast expand further and eventually unite into a single pro-amniotic cavity[55].

These different patterns lead to different configurations between post-implantation mouse and human embryo. The human epiblast adopts a flat disc-like structure with a single cavity covered with amniotic epithelium **(Figure 7 C)**. In contrast, the mouse embryo gives rise to a concave configuration of an egg cylinder **(Figure 7 F)**. This is believed to be the physical pressure imposed on the epiblast by the invagination of the polar trophectoderm to form the ExE. This does not happen in humans, where the polar trophectoderm mediates implantation, in contrast to the formation of ExE in mouse. Thus, the epiblast is pushed inside the mouse blastocoel cavity and resembles a cup-shaped configuration, resembling a cylinder rather than a flat disc as seen in humans.

D. Gene expression and signaling pathways that determine the pluripotent state of human and mouse ESCs

The culture condition used to propagate hESCs namely FGF2 and activin can be used to establish pluripotent stem cell lines from post-implantation mouse and rat epiblast[56]. The above culture condition keeps hESCs in a primed state. In contrast, mESC can be derived from the pre-implantation ICM in the presence of leukemia inhibitory factor (LIF) or defined culture condition in the presence of inhibitors for FGF/Erk and glycogen synthase kinase3 (GSK3). Genome-wide transcriptional profiles of human ICM and hESCs indicate differences in the set of gene expression and signaling pathways such as TGF beta, insulin growth factor (IGF) and MAPK pathways, which are uniquely expressed in human ICM but not in hESCs. This shows that *in vitro* hESCs do not reflect the *in vivo* pluripotency of human ICM (cite). *In vitro* culturing of hESCs resembles properties of post-implantation mouse epiblast cells.

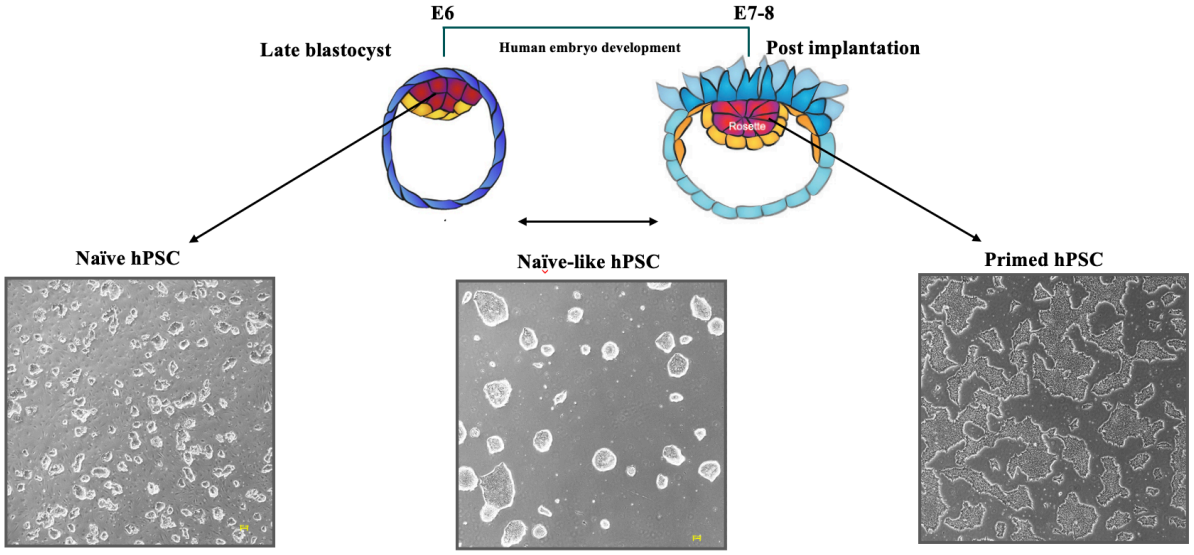

Figure 8. Human embryonic stem cells across the pluripotent spectrum. Based on the pluripotent state and the media in which they are cultured, human embryonic stem cells are of 3 types: Naïve, Naïve-like and primed. Naïve hPSCs have the capacity to give rise to trophectoderm cells by in vitro reprogramming assay either by over-expressing Cdx2 or by inhibiting the genes specifying for epiblast identity. The naïve-like and primed hPSCs cannot be reprogrammed to trophectoderm cells although like the naïve hPSCs they can differentiate to give rise to ectoderm, mesoderm and endoderm cell lineages. Modified figure from (Mole, Weberling and Zernicaka-Goetz., 2019).

Human pluripotent stem cells (hPSCs) are of three types based on their pluripotent state and the media in which they are cultured.

Naïve hPSCs: hPSCs when cultured in chemically defined medium containing FGF/activin, resemble the pluripotent state of a post-implantation epiblast. There are methods by which hPSCs can be reprogrammed to more naïve conditions resembling the ICM of the pre-implantation blastocyst. PXGL culture is one of the many naïve cultures that is used to maintain hPSCs in a more naïve state. The culture employs the use of human LIF with three inhibitors (3i) that block MEK, Wnt and PKC pathways. These cells resemble the ICM cells of pre-implantation human embryos where both the X-chromosomes remain active **(Figure 8)**. Naïve hPSCs express naïve markers like KLF17, KLF4 TFCP2L, DNMT1, DNMT3B, DNMT3L, DPPA3, DPPA5 Rex1, OCT4, NANOG and SOX2. The colonies of naïve hPSCs are compact, and dome-shaped with shiny borders. These cells have the ability to differentiate into ectoderm, mesoderm and endoderm.

Naïve-like hPSCs: Primed hPSCs can be reprogramed to a more naïve-like state by growing them in a commercially available media called RSeT. The media has been developed in the Weizmann Institute and marketed by StemCell technologies. These cells express both markers of naïve (KLF17, KLF4, TFCP2L, DPPA3, DNMT3L) and primed state of pluripotency (ZIC2, OTX2 CD24, THY1 and XIST). The colonies of naïve hPSCs are compact, and dome-shaped with shiny borders. These cells have the ability to differentiate into ectoderm, mesoderm and endoderm **(Figure 8)**.

Primed hPSCS: The culture condition used to propagate hESCs namely FGF2 and activin can be used to establish pluripotent stem cell lines which resemble cells coming from the post-implantation human embryo **(Figure 8)** They grow as compact flat colonies and express markers such as ZIC2, OTX2 CD24, THY1 and XIST. In my thesis, I used mTeSR media for culturing of primed hPSCs. These cells do not have the ability to differentiate into trophoblast lineage.

E. In vitro stem cell models

Many research groups have established embryo-like model systems to recapitulate various steps of embryonic development. These models allow us to study not only embryonic development but also prenatal defects and tissue regeneration. The various in vitro stem cell-based embryo models give an advantage of scalability by reproducing them in large numbers which is advantageous for high throughput screenings for developing stem cell or drug therapies. In addition, one can study human embryonic development in great mechanistic detail. Pre-implantation embryo-like models such as blastoids[57] enable the investigation of the first steps of lineage specification, lineage segregation and implantation. Post-implantation models like ETX embryo[58], gastruloids[59] or TLS models[60,61] provide flexibility in studying gastrulation mechanism, cellular dynamics and signaling pathways that coordinate the process of self-organization.

Using human blastoid models can help us investigate whether humans have the ability to pause development. Human blastoids are human blastocyst-like structures that have 97% transcriptional similarity to human embryos **(Figure 9)**. It is a high throughput system and allows one to interrogate the possibility of human dormancy without going through stringent ethical approvals. The blastoids mimic a human embryo by having an ICM which is surrounded by trophectoderm cells and having an intact blastocoel. These are formed when naïve human PSCs cultured in PXGL media are inhibited for Hippo, TGFβ and Erk pathways to form blastoids which resemble a human blastocyst in having all the three germ layers that are formed according to the sequence and timing of blastocyst development. The blastoid ICM shows markers for pluripotency and also is positive for TE marker CDX2 **(Figure 9)**. The epiblast of the blastoids also induces the maturation of polar trophectoderm, allowing blastoids to implant on hormonally stimulated endometrial cells. The blastoid system has been used in my present Ph.D. thesis to interrogate the possibility of dormancy occurring in humans.

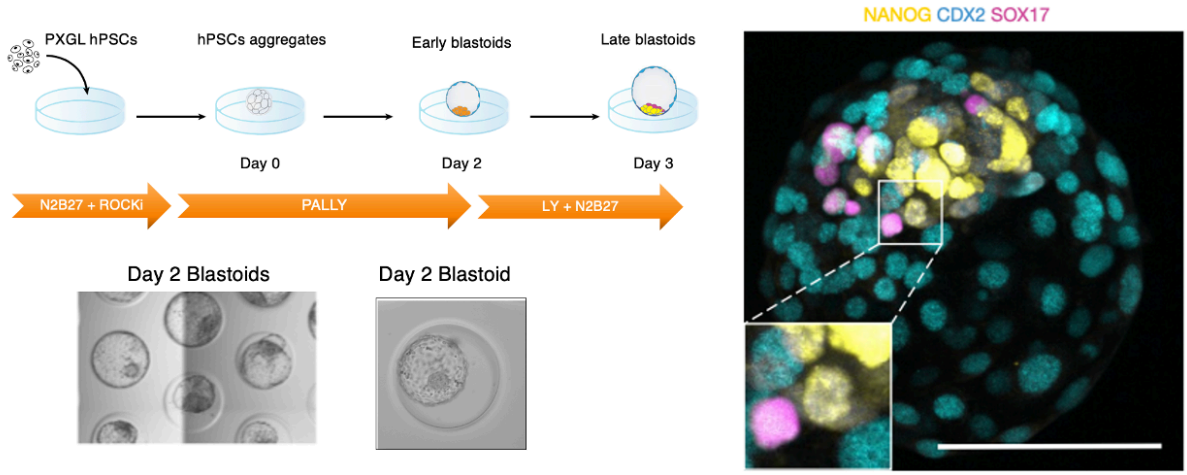

Figure 9. Naïve hPSCs or PXGL cells efficiently form blastocyst-like structures showing analogs of the three founding lineages. Human stem cells can form blastocyst models called blastoids. These are formed when naïve human PSCs cultured in PXGL media are inhibited for Hippo, TGFβ and Erk pathways to form blastoids which resemble a human blastocyst in having all the three germ layers that are formed according to the sequence and timing of blastocyst development. The epiblast of the blastoids also induces the maturation of polar trophectoderm, allowing blastoids to implant on hormonally stimulated endometrial cells (Kagava et al., 2021)

F. mTOR and its role in growth and metabolism

The mechanistic target of rapamycin (mTOR) influences cell growth and metabolism in response to environmental stimuli such as nutrients and growth factors. mTOR influences many cellular processes such as glucose homeostasis, protein synthesis, and autophagy among others and is also implicated in many diseases such as cancer, diabetes and aging.

mTOR is a serine/threonine protein kinase that functions via two distinct protein complexes – mTOR complex I (mTORC1) and mTOR complex II (mTORC2) (figure – mTOR pathway). mTORC1 has 3 core components – mTOR, Raptor (regulatory protein associated with mTOR) and mLST8 (mammalian lethal with Sec13 protein 8)[62,63]. Raptor facilitates substrate recruitment to mTORC1 through binding to the TOR signaling (TOS) motif found on several canonical mTORC1 substrates is required for correct subcellular localization of mTORC1. mLST8 by contrast associates with the catalytic domain of mTORC1 and may stabilize the kinase activation loop[64]. The mTORC1 also contains inhibitory subunits PRAS40 (proline-rich Akt substrate of 40 kDa) and DEPTOR (DEP domain containing mTOR interacting protein)[65–68] **(Figure 10)**. Like mTORC1, mTORC2 also contains mTOR and mLST8. Instead of Raptor, mTORC2 contains Rictor (rapamycin insensitive companion of mTOR). mTORC2 also contains DEPTOR as well as the regulatory subunit mSin1 and Protor1/2[69–72] **(Figure 10)**.

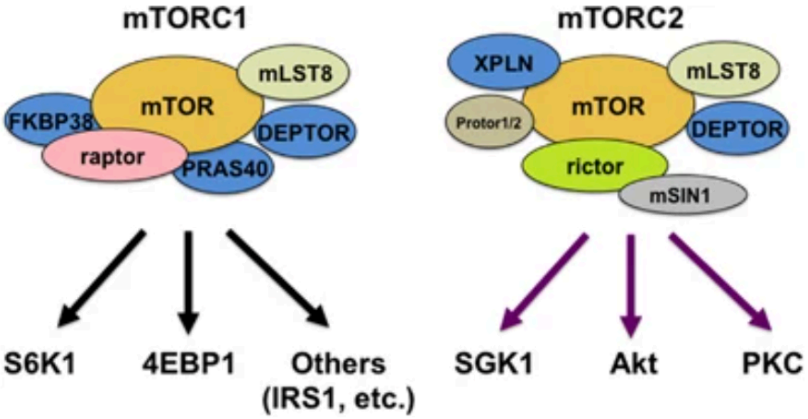

Figure 10. Components of the mTORC1 and mTORC2 complexes. Raptor and Rictor are the major subunits of TORC1 and TORC2 complexes respectively. mLST8 which is present in both the complexes is concerned with the kinase activity. Subunits depicted in blue are inhibitors of mTOR activity (Yoon and Choi., 2016).

F.1 mTORC1 downstream signaling

mTORC1 plays a central role in balancing anabolism and catabolism based on the surrounding environmental conditions. This complex aids in cell growth by increasing the production of proteins, lipids and nucleotides and suppressing processes such as autophagy.

Protein synthesis: mTORC1 directly phosphorylates S6K1 which in turn phosphorylates and activates many substrates that promote mRNA translation. S6k1 phosphorylates PDCD4 which is an inhibitor of 4IF4B[73] which is a positive regulator of the 5'cap binding eIF4F complex **(Figure 11)**. mTORC1 phosphorylates 4EBP at multiple sites to trigger its dissociation from eIF4E[74,75], allowing 5'cap-dependent mRNA translation to occur.

Lipid, nucleotide and glucose metabolism: Growing cells require sufficient for new membrane formation. mTORC1 promotes lipid synthesis through the sterol-responsive element binding protein (SREBP). which control the expression of metabolic genes involved in fatty acid and cholesterol biosynthesis **(Figure 11)**. When mTOR is active SREBP gets phosphorylated by S6K1[76]. Lipin inhibits SREBP expression when mTOR is inactive **(Figure 11)**. Studies have shown that mTORC1 also plays a role in nucleotide synthesis required for DNA replication and ribosome biogenesis for the growth and proliferation of cells[77]. mTORC1 increases the ATF4-dependent expression of MTHFD2, a key component of the mitochondrial tetrahydrofolate cycle that provides one-carbon units for purine synthesis. S6K1 also phosphorylates and activates carbomyl-phosphate synthetase (CAD) for de novo pyrimidine synthesis[78,79]. mTORC1 also promotes the growth of cells by promoting a shift from oxidative phosphorylation to glycolysis. mTORC1 increases the translation of HIF1 alpha which drives the expression of many glycolytic enzymes such as phospho-fructo kinase (PFK)[76]. mTORC1

through SREBP increases the pentose phosphate pathway for the generation of NADPH and other intermediates required for the growth and proliferation of cells.

Regulation of protein turnover: mTOR promotes the growth of the cell by suppressing protein catabolism **(Figure 11)**. Autophagy is suppressed during cell growth and proliferation. The main player of autophagy ULK1, forms autophagosomes by partnering with ATG13, FIP2000, ATG101. In nutrient-abundant conditions, mTORC1 phosphorylates and inactivates ULK1 thereby preventing autophagy[80]. mTORC1 also phosphorylates transcription factor EB (TFEB) which drives the expression of lysosomal genes and genes involved in autophagy[81–83]. Another major pathway for protein turnover is the ubiquitin-proteosome system (UPS). In this system proteins that are ubiquitinated are selectively degraded by 20S proteosomes. Studies have shown acute inhibition of mTOR leads to rapid proteosome-dependent proteolysis through either in increase of protein ubiquitination[84] or by increase in the abundance of proteasomal chaperones via inhibition of Erk[85]. A new study has shown that there is a dynamic movement of the proteasome complex between the nucleus and cytoplasmic compartments during cellular stress which is dictated by the activity of mTORC1[86].

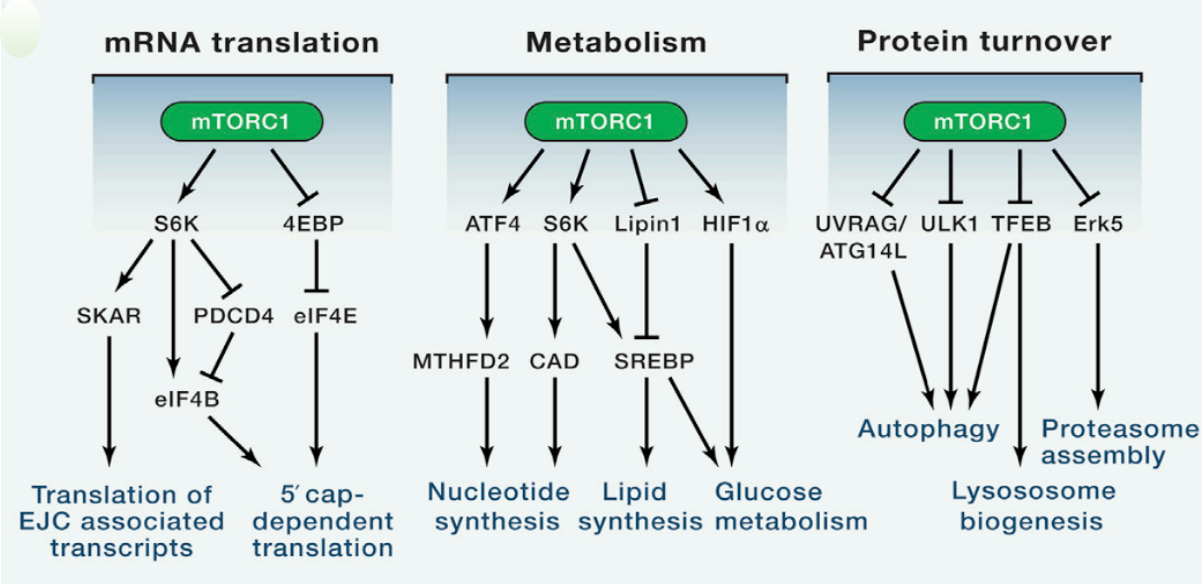

Figure 11. Major pathways downstream of mTORC1 signaling. Depending on environmental signals, the mTORC1 complex balances the anabolic and catabolic functions of the cells in providing the growing proliferating cells with essential nutrients such as protein, lipids and nucleotides (Saxton and Sabatini., 2017).

F.2 mTORC2 downstream signaling

mTORC2 controls cell proliferation and survival by phosphorylating members of AGC (PKC/PKA/PKG) family of protein kinase **(Figure 12)**. The first mTORC2 substrate to be identified was PKCα, a regulator of the actin cytoskeleton[87,88]. More recently, mTORC2 has also been shown to phosphorylate several other members of the PKC family, including PKCδ[89],

PKCζ[90], as well as PKCγ and PKCε[91], all of which regulate various aspects of cytoskeletal remodeling and cell migration. The most important role of mTORC2 is phosphorylation and activation of AKT – a key effector of insulin/PI3K signaling. Once active, Akt promotes cell survival, proliferation, and growth through the phosphorylation and inhibition of several key substrates, including the FoxO1/3a transcription factors, the metabolic regulator GSK3b, and the mTORC1 inhibitor TSC2. mTORC2 also phosphorylates and activates SGK1, another AGC-kinase that regulates ion transport as well as cell survival[92].

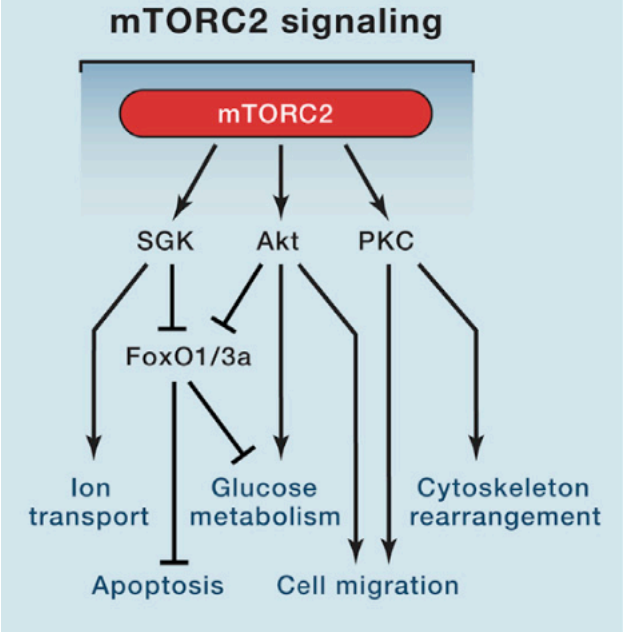

Figure 12. Major pathways downstream of mTORC2. The complex is a major organizer of the cytoskeleton and also promotes the survival and growth of cells via phosphorylation of AKT (Saxton and Sabatini., 2017).

F.3 Upstream regulation of mTORC1

Growth factors and morphogen signaling

Many growth factors and mitogen signaling pathways are known to be upstream of mTORC1, which inhibits the TSC complex – a negative regulator of mTORC1[93]. the growth factors activate small GTPase Rheb which binds and activates mTORC1. Other growth signaling pathways like IGF1, trigger AKT-dependent phosphorylation of TSC which inhibits TSC function[94,95]. Similarly, receptor tyrosine kinase-dependent Ras signaling activates mTORC1 via the MAP Kinase Erk and its effector $p90^{RSK}$, both of which also phosphorylate and inhibit TSC2[96]. Wnt and TNFα activate mTORC1 through the inhibition of TSC complex[97]. Precisely how the TSC integrates these numerous signals and their relative impact on mTORC1 activity in various contexts, however, remains an open question.

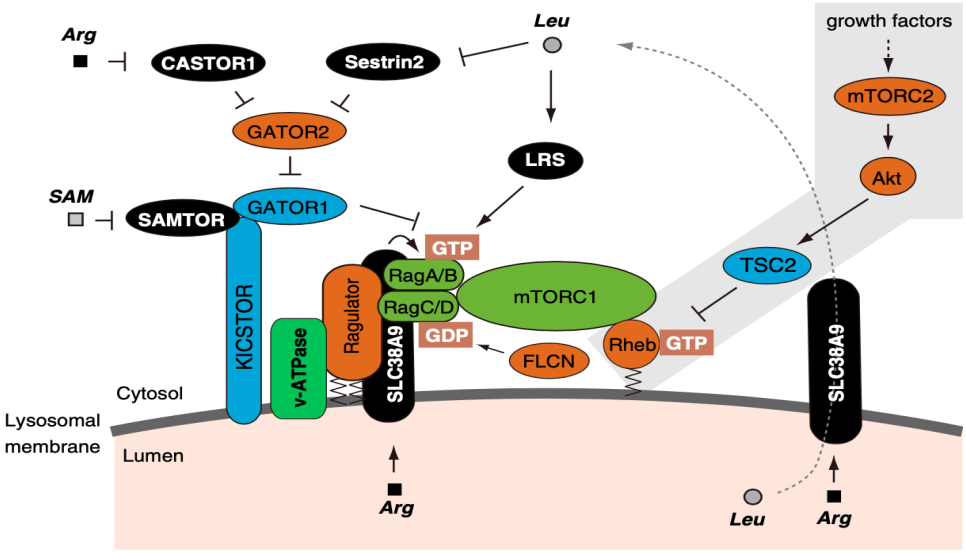

Figure 13. Schematic showing activation of mTORC1 by growth factors and amino acids. Amino acids like Q, L and R and growth factors like IGF1, Wnt, and TNFα act upstream of mTORC1 and activate it via inhibition of the TSC complex. These upstream factors activate Rags and Rheb. Both the upstream components converge at TSC by an unknown mechanism. Gator 2 acts as a central node in the activation of mTORC1 in the presence of amino acids whose activity is regulated by amino acid sensors Sestrin2 and CASTOR1 (Takahara et al., 2020)

Amino acids

Amino acids from dietary intake activate Rags which bind to Raptor and recruit them to the lysosomal surface where Rheb is located. mTORC1 gets activated only when both Rags and Rheb is activated. This explains both growth factors and amino acids are required for mTORC1 activation. mTORC1 senses both lysosomal and cytosolic amino acids. The lysosomal amino acid transported by SLC38A9 interacts with the Rag-Regulator-v-ATPase complex and is required for arginine to activate mTORC1[98,99]. Cytosolic leucine and arginine signal to mTORC1 through a distinct pathway comprising the GATOR1 and GATOR2 complexes[100]. GATOR1 consists of DEPDC5, Nprl2, and Nprl3 and inhibits mTORC1 signaling by acting as a GAP for RagA/B. GATOR1 is necessary for control of mTORC1 activity by nutrients[101]. On the other hand, GATOR2 is a positive regulator of mTORC1 activity[100]. Cytosolic amino acid sensing by mTORC1 is regulated by Sestrin2 which is a leucine sensor. In the absence of leucine, Sestrin2 binds to GATOR2 and inactivates mTORC1 activity[102]. Studies have shown that Sestrin2 is transcriptionally induced upon prolonged starvation. In such conditions, Sestrin2 binds to GATOR1 and inhibits mTORC1 activity[103]. Like Sestrin2, another amino acid sensor CASTOR1, binds to GATOR2 and inhibits mTORC1 function when arginine is unavailable[104]. Thus, both leucine and arginine stimulate mTORC1 activity at least in part by releasing inhibitors from GATOR2, establishing GATOR2 as a central node in the signaling of amino acids to mTORC1. Another study has found that glutamate activates mTORC1 via Arf family GTPase[105] **(Figure 13)**.

F.4 Upstream regulation of mTORC2

mTORC2 activation depends primarily on insulin/PI3K signaling. mTORC2 subunit mSin1 contains a phosphoinositide-binding PH domain that is critical for the insulin-dependent regulation of mTORC2 activity. The mSin1 PH domain inhibits mTORC2 catalytic activity in the absence of insulin, and this autoinhibition is relieved upon binding to PI3K-generated PIP_3 at the plasma membrane[106]. mSin1 also gets phosphorylated by AKT suggesting the presence of a positive-feedback loop, where partially activated AKT promotes activation of mTORC2, which in turn fully activates and phosphorylates AKT[107]. mTORC2 signaling is also regulated by mTORC1, due to the presence of a negative feedback loop between mTORC1 and insulin/PI3K signaling. mTORC1 phosphorylates and activates Grb10, a negative regulator of insulin/IGF-1 receptor signaling upstream of Akt and mTORC2[108], while S6K1 also suppresses mTORC2 activation through the phosphorylation-dependent degradation of insulin receptor substrate 1 (IRS1)[109].

Thus, by modulating the upstream or downstream pathways of mTOR, one can dissect the molecular mechanism by which diapause is triggered in embryos.

G. Embryonic diapause

Embryonic diapause or delayed implantation is a process where the developing embryo suspends its growth at the blastocyst stage **(Figure 14)**. The embryo either ceases cell division such that the size and number of cells remain constant or the embryo enters a state of slow growth with minimal cell division and expansion. Many mammals delay their embryonic development and this strategy is employed by over 100 mammalian species to adjust the timing of birth such that the offspring and mother will have better chances of survival during challenging environmental conditions or during a period of energetically demanding lactational stress.

Development of a mammalian embryo is a complex process that requires constant interaction with the uterus. Acknowledging the significance of this process, yet it is unknown the critical signals that are exchanged between the uterus and the fetus. The period or the process of diapause provides an invaluable tool for researchers to understand maternal control over the developing embryo. Diapause involves three phases: 1) Induction or entry into diapause where there is arrest in cell division, 2) Maintenance of diapause where there rewiring of genome, transcriptome and metabolome and 3) Reactivation from diapause where a normal state is reestablished.

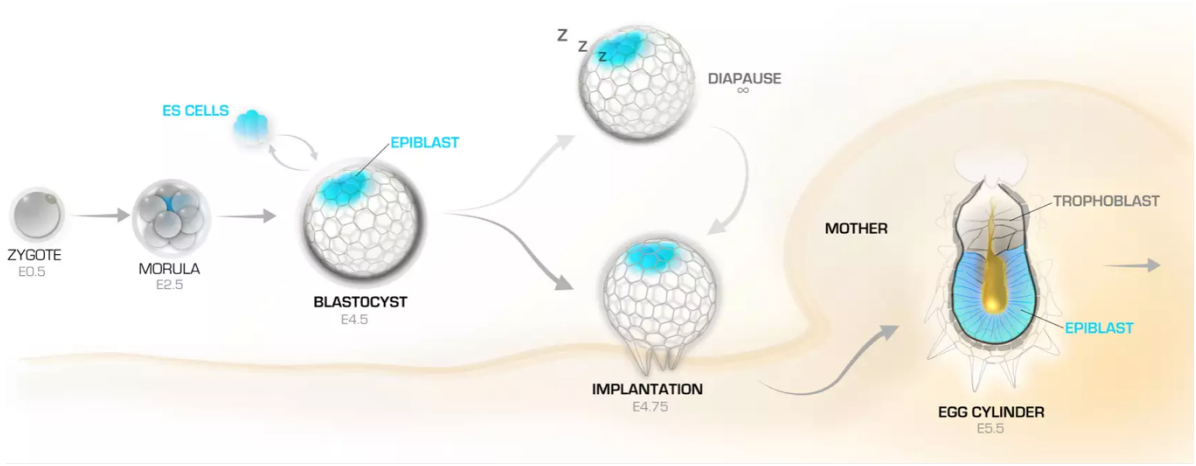

Figure 14. Schematic showing mouse embryonic diapause. It's a reproductive phenomenon employed by mammals to temporally uncouple conception from delivery until conditions are favorable for survival for the mother and newborn. While the maternal endocrine milieu has been shown to be important for the process, the local molecular mechanism by which the uterus and embryo achieve quiescence, maintain blastocyst survival and plasticity and later its activation with subsequent implantation in response to endocrine cues remains unclear (Bedzhov,2023).

Diapause triggered by changing environmental conditions, termed obligate diapause is employed by American mink where the diapause is according to the timing of the mating[110]. Exit from diapause is triggered by increasing daylight in the northern hemisphere[111]. House mouse undergo facultative diapause where the blastocyst undergoes diapause when pregnancy and lactation happen at the same time. Mice have been extensively used as a diapause model because of their relatively short gestation period and their embryos are amenable to genetic modifications and also amenable to *in vivo* and *ex vivo* culture. Diapause in mice can be artificially triggered by ovariectomy at E3.5 or by injection of estrogen antagonist[112]. In addition to this progesterone supplementation is required to sustain pregnancy. Diapausing mouse embryos can be sustained for a period of 36 days or longer in vivo, however, embryo loss occurs over time[113]. Exit from diapause is triggered by increased uterine receptivity or when lactation ends or can be experimentally induced by injection of estradiol. *Ex vivo* mouse blastocysts can be brought to diapause by pharmacological inhibition of mTOR[114] where blastocysts can survive up to 30 days. Mouse embryos can be brought to diapause by over-expression of let7 (up to 14 days)[115] or by overexpression of miR-92 (up to 18 days) (Iyer and Lambert., et al unpublished).

G.1 Dynamics and features of diapausing mouse embryos

The mouse embryo reaches complete dormancy after five days in diapause[116]. The TE and ICM cells have different dormancy dynamics in response to diapause. During diapause, the mural TE (TE surrounding the blastocoel cavity) ceases proliferation after day 1 of diapause induction. The polar TE and ICM cells slowly cease proliferation after four days in diapause culture[116]. Upon reactivation, the polar side of the embryo reactivates first followed by the mural side[116]. The diapaused blastocyst is about 4 times the size of a normal E4.5 embryo[116] and has about 140 cells. The epiblast and PrE do not grow during dormancy and can shrink by

40-50% [117]. The mural TE does not proliferate but the polar TE continues to increase in number and the cells assume a stretched position which gives the diapausing mouse embryo the characteristic elongated shape.

G.2 Conservation of diapause in non-diapausing species

To test the capacity of diapause in non-diapausing species, interspecies transfer experiments have been performed. Embryos from closely related species mink (shows diapause) and ferret (does not naturally diapause) were reciprocally transferred[118]. Ferret embryos showed delayed development and did not implant in the mink uterus under diapause, while normally diapausing mink embryos activated and implanted into the ferret uterus. An independent study showed sheep embryos undergoing diapause in the mouse uterus under diapause conditions, which upon activation and retransfer were able to give rise to live-born lambs[119]. These studies point to uterine control of diapause induction and maintenance and the conservation of diapause pathways, at least in mammals that have been studied. These experiments show that diapausing uterine fluid has factors that trigger diapause in embryos and alter various cellular processes for the maintenance of dormancy.

G.3 Possibility of diapause in humans

To date, there is no evidence that shows human embryos can diapause. If there is a possibility of diapause existing in humans, it could only be detected by pregnancies following the transfer of IVF embryos. Naturally conceived human embryos implant 7–11 days after ovulation, although a range of 6–18 days was observed[120]. Late implantation of human embryos is associated with a high rate of pregnancy loss. Although the question has been raised in the past, a convincing case of functional and molecular reversibility of diapause with intact morphology has never been shown yet. External factors such as smoking can cause implantation delays and pregnancy loss. Taken together, there is currently no evidence that humans might use natural diapause as a reproductive strategy. If diapause were to occur in humans it would be triggered by exogenous stress such as malnutrition, work pressure, untimely sleep patterns or anxiety. Testing the capacity of human embryos to undergo diapause is possible only by ex vivo testing of IVF embryos that have been donated by patients. Human blastocysts were reported to undergo diapause when coated with a mucin-mimicking synthetic gel, however, these did not retain the characteristic blastocyst morphology[121].

G.4 Molecular regulation of diapause

G.4.1 Cell cycle

Diapause is associated with reduced cell proliferation. Cell cycle-related genes are most altered between diapause and activated blastocyst. In mice, it has been suggested that cell cycle arrest is estrogen-mediated and thus controlled maternally via downregulation of the tumor repressor Brca1 and upregulation of the anti-proliferation gene Btg1[122]. Mouse ESCs upon mTOR inhibition reduce the rate of proliferation and show a modest change in cell cycle

distribution[114]. In contrast, Myc inhibition, which also leads to a diapause-like state, enriches G0/G1 cells and depletes the S phase[123]. This suggests that in *in vitro* and *in vivo* diapause have certain differences in cell cycle control and should be further studied to understand the establishment of paused pluripotency.

G.4.2 Genome regulation during dormancy

Dormancy involves changes in genome wiring. The change is reflected by gene expression changes during diapause and is associated with altered pathway function. DNA replication and cell proliferation are repressed during the period of dormancy, which is later restored upon exit from dormancy. This dynamic regulation of cellular processes points towards the direction of rapid chromatin reorganization. Ultrastructural observation by transmission electron microscopy in diapausing embryos shows extensive chromatin reorganization with an increase in heterochromatic foci at the nuclear periphery accompanied by denser punctuated nucleoli with decreased ribosome RNA synthesis seen in epiblast cells[124,125].

G.4.3 Epigenetic changes during dormancy

Changes in histone modifications reflect on changes in gene expression and hence the pathway function. These changes are the reflection of intense genome rewiring that happens during diapause. Chromatin of ICM cells is particularly sensitive to diapause and shows depletion of histone acetylation such as H4K16ac[114]. Genetic knockout of enzyme that acetylates H4K16 induces dormancy in ES cells, suggesting that depletion of acetylation could induce pausing by a reduction in global transcriptional output[126]. Dormancy is associated with reduced histone acetylation and transcription which results in increased heterochromatin formation[127]. Electron microscopy analysis of diapause vs. active blastocysts revealed more condensed nucleoli and abundant heterochromatin in Epi and TE cells, which decondensed within 12 h of reactivation. Most of the genome is heterochromatinized during dormancy. Polycomb-mediated H3K27me3 deposition might be responsible for transcriptional repression and maintaining diapause in mammals[128]. Additionally, a subset of genes is upregulated and possibly induces or maintains dormancy. How this subset of genes escapes silencing during dormancy remains to be investigated.

G.4.4 Global reduction of transcription and translation during dormancy

Mouse ESCs and epiblast of mouse blastocyst have a high proliferative potential with a shorter cell cycle. This high rate of proliferation is reflected in the high rate of transcription of the genome which is associated with active chromatin marks such as histone acetylation. The openness of the chromatin is responsive to high translational output which in turn is correlated to transcriptional rate[129,130]. Diapausing mESCs proliferate slowly and have inhibited cell growth. These cells have reduced transcription and translation output[131]. The amount of RNA is 2-4-fold less than proliferating ESCs. The impact of less transcription and translation is reflected in cell size where the diapausing ESCs have a smaller size. Upon reactivation, both diapause mESCs and embryo go back to having a high rate of transcription and translation. It

has to be investigated how transcription and translation go back to the previous level with associated chromatin remodeling. One area that can be looked into is the posttranscriptional modification brought about by microRNAs (miRNAs). miRNAs in the context of diapause might act as first responders in bringing quick dynamic changes to protein repertoire by binding to mRNAs and preventing translation. They may act as a pivot to balance nascent regulation to achieve repression during dormancy and on-demand reactivation upon release from dormancy.

G.4.5 Dormancy alters the metabolic signature

Diapausing mESCs and mouse embryos have low metabolic rates and altered pathway usage. The dormant ICM is metabolically more quiescent than TE. Highlighting cell type heterogeneity in response to diapause[132]. ICM cells show altered mitochondrial morphology, reduced mitochondrial respiration, reduced oxidative phosphorylation and increased autophagy rate. Reactivation from diapause shows active mitochondrial respiration and a decrease in autophagy. However, the role of glycolysis is less clear, with studies reporting either increased or decreased glycolysis downstream of mTOR inhibition in ES cells and in diapause embryos[133,134]. Reactivated mouse embryos show a high rate of glucose uptake and high expression of glycolytic genes. In the absence of glucose, reactivation is delayed which points to the importance of glycolysis during dormancy exit. The glutamine transporter Slc38a1 is also upregulated in the ICM during diapause and inhibition of it is detrimental to the embryo's capacity to pause[133]. Although the above insights into changes in metabolic pathways is through RNA and proteomics data, it becomes essential to validate it extensively by Seahorse assay to get real-time information on changes in metabolic activity happening at the time of dormancy entry and exit in mouse ESCs.

It has been shown that dormant embryos utilize lipids as a major energy source . Free fatty acids and phospholipids are in abundance in diapausing embryos compared to their active counterparts[133] which is indicative of a high rate of lipolysis. Removal of lipid droplets from mouse zygotes impairs the survival of the diapause blastocysts, indicating active utilization during diapause[113]. Recently, it has been shown that supplementation of carnitine which transports long-chain fatty acids into the mitochondria for beta oxidation, allows embryos to undergo deeper dormancy for a period of up to 34 days[124].

H. MicroRNA role in diapause

MicroRNAs are small non-coding RNAs that exert their regulatory influence by suppressing gene activity via transcriptional silencing, transcript degradation or translation inhibition[135]. The above modes of regulation are largely based on the extent to which the seed sequence of miRNA matches its target[136]. The promiscuity of the seed sequence allows miRNA to regulate many target genes at once[137]. Combinatorial miRNA activity, i.e., multiple miRNAs controlling a given gene and one miRNA controlling multiple genes, provides pathway-level control[137] allows cell state or fate transition that involves alteration in many cellular processes. Furthermore, miRNAs usually control metabolic, proliferation, apoptosis, and developmental pathways, all of which are essential components of diapause. MicroRNAs are known to play a

role in dormancy where they bring its regulatory effect by fine-tuning gene expression while working with other regulatory elements[137].

The evidence for miRNA function in diapause largely originates from genomic profiling studies. Diapause results in altered miRNA profiles in many mammalian and non-mammalian species[115,138]. Since microRNAs are expressed in a tissue-specific manner, based on cell type it is possible that different microRNAs are involved in bringing dormancy induction, maintenance and reactivation. For example, in *C. elegans* diapause, the miRNA miR-71 suppresses the growth-promoting PI3K/insulin pathway and miR-235 acts downstream of the insulin pathway to arrest development, pointing to the central role of the insulin pathway in diapause control across species. Overexpression of let-7 brings alteration in developmental timing by suppressing mTOR and MYC activities[115]. In mouse diapause, let-7 is of maternal origin and is transferred to the embryo via extracellular vesicles. Showing direct maternal control of the embryonic state[115].

Studying only individual microRNA and how it regulates its downstream target will give a narrow understanding of its mode of action during dormancy. Given the role played by microRNAs in diapause, it becomes necessary to dissect the combinatorial action of miRNAs during dormancy transition. Thus, functional perturbation of microRNAs is necessary to address its complex regulatory activity in the context of diapause. Many miRNAs have oncogenic activity[139] Given the importance of understanding dormancy pathways in cancer, investigating miRNA-mediated dormancy in diapause may enlighten oncogenic miRNA activity. miRNAs are assembled into extracellular vesicles and circulating oncogenic miRNAs are used as cancer biomarkers[139]. It is an intriguing possibility to use circulating miRNAs as potential diapause biomarkers, especially in wildlife species where diapause detection has otherwise not been successful.

Aim of the study

Part 1: Uncovering the molecular mechanism of microRNA-regulated induction of dormancy in mouse embryonic stem cells and embryos.

Despite the recent studies on miRNAs as developmental regulators in lifetime extension in worms and mouse, much of the focus has been on the action of individual miRNAs and its target interaction. This limits our understanding of the combinatorial nature of miRNA activity as a key regulator of dormancy. Here through my thesis, I aimed to give a macroscopic view of the microRNA regulatory network that functions during the onset of dormancy by:

1) Identifying miRNAs that are specifically upregulated during mouse diapause.
2) To develop miRNA-protein network for understanding the combinatorial functioning of miRNAs in regulating the transition into dormancy in mouse embryos and ESCs.
3) Identifying the upstream regulator of miRNA biogenesis.

Part 2: Exploring the hypothesis of whether human PSCs and blastoids regulate their timing of development via the mTOR pathway.

mTOR which is a nutrient-sensing pathway plays a central role in regulating the developmental timing of mouse embryos. Under mTORi, mouse embryos can reliably be maintained in their quiescent state for a prolonged period of time without compromising their developmental identity. Although the role of mTOR inhibition in dormancy induction is well documented in the mouse system, the main question of human PSCs undergoing dormancy still remains to be answered. Through my thesis, I aimed to explore the possibility of human dormancy occurring via mTOR inhibition by:

1) Comparative testing of human PSCs across the pluripotent spectrum.
2) Testing the effect of developmental time on human blastoid.

Results:

Part 1: Uncovering the molecular mechanism of microRNA-regulated induction of dormancy in mouse embryonic stem cells and embryos.

Previous work from Bulut-karslioglu *et.al*[114]shows that successful entry into dormancy requires a global rewiring of transcriptional and translational landscape where the majority of genes are functionally silent. Bulk RNA seq showed that within this transcriptionally repressed genome, some microRNA genes show high transcriptional activity during this period. Leveraging the *in vitro* mouse ESC system, during my doctoral work I aimed to address the microRNA expression profiles that is necessary for the successful entry of mouse ESCs and embryos into dormancy.

1.1 miRNAs are indispensable for the establishment of paused pluripotency in mESCs.

MicroRNAs (miRNAs) are known to fine-tune gene expression at the post-transcriptional level to aid the cellular machinery to adapt to various stressors[140]. With this in view, I hypothesized that miRNAs may act as one of the important regulatory layers in mouse embryonic stem cells (mESCs) for their transition from active proliferative to the less proliferative diapause-like state via mTOR inhibition (mTORi). To put this hypothesis to the test, I took advantage of using mESCs devoid of any canonical mature miRNAs (a gift from Prof. Constance Ciaudo, ETH, Zurich). Mouse ESCs without mature miRNAs are made by knocking out *Dgcr8* (also called PASHA in C.elegans and D.melanogaster) which is part of the nuclear microprocessor complex that processes pre-miRNA from their primary transcripts[141]. *Dgcr8* KO mESCs do not have any proliferative defects under normal culture conditions (serum/LIF) and their proliferation rates are comparable to wild-type mESCs **(Figure 15 A and B)**. The use of the above KO cell line allowed me to know whether miRNAs are critical for the onset of dormancy via mTORi.

I induced a diapause-like dormant state in wild-type and *Dgcr8* KO mESCs via mTOR inhibition. mTOR inhibition greatly reduced the proliferation of wild-type mESCs at the same time I observed that these maintained a domed-shaped morphology with shiny borders – a characteristic of a pluripotent colony. In contrast, Dgcr8 KO mESCs did not respond well to mTOR inhibition. The KO cells progressively died during mTORi where the majority of the cells died within 2-3 days of mTORi **(Figure 15 A and B)**.

Through the above results, I was successful in showing that miRNAs are indispensable for establishing a diapause-like dormant state in mESCs. Without miRNAs, mTORi-mediated diapause induction is detrimental to mESCs.

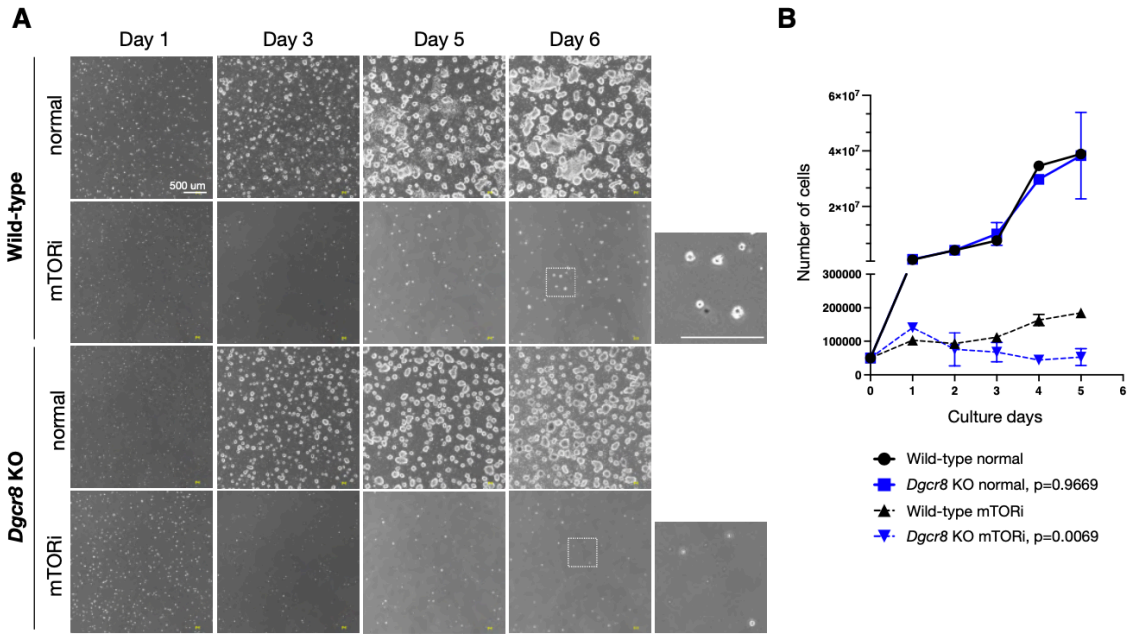

Figure 15. MicroRNAs are indispensable for mouse ESCs to transition into dormancy.
A. Bright field images of wild-type and *Dgcr8* KO mESCs in normal proliferative and dormancy conditions. Dormancy was induced by adding mTOR inhibitor INK128 to the culture media. Both the cell types were allowed to undergo dormancy via mTOR inhibition. Scale bar = 500µm.
B. Graph showing proliferation curves of wild-type and *Dgcr8* KO mESCs in normal proliferative and dormancy conditions. Both the cell types were plated at low density on 6 well culture plates and counted on respective days as shown without splitting. Statistical test non-linear regression (curve fit). *Dgcr8* KO ESCs were compared to wild-type ESCs for normal and mTORi dormant conditions.

1.2 *Dgcr8* is essential for the transition of early mouse embryos into dormancy upon mTOR inhibition.

To further test the essentiality of miRNA for diapause induction in an embryo setting, I leveraged the use of aggregations with the help of my colleague Lars Wittler (head of the transgenic unit at MPIMG). This method employs aggregation of ES cells and microinjecting them in diploid morula stage mouse embryo. The reason for using this technique is **1.** To maintain the natural ploidy of the embryo and **2.** To maintain the cells of the trophectoderm (TE) in a wild-type state - such that only the inner cell mass (ICM) is chimeric with cells contributed from donor injection and cells contributed by the recipient embryo **(Figure 16)**.

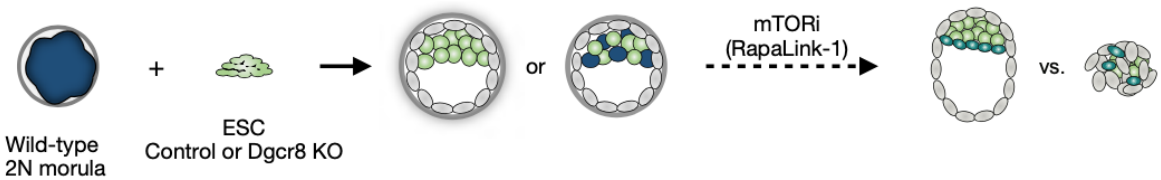

Figure 16. Schematic showing DIPLO morula aggregation experiment.
Wild-type and *Dgcr8* KO mouse ESCs were labeled with EGFP which was randomly integrated into the genome. The donor EGFP mouse ES cells were aggregated with wild-type diploid morulae. These were allowed to develop until the blastocyst stage after which they were treated with DMSO or mTORi (Rapalink-1). The number of intact blastocysts with or without ICM was counted every day. Blastocysts with intact blastocoel and unfragmented TE were considered intact.

To assess the contribution of each of the cell types to chimera formation, I randomly integrated the eGFP reporter into the genome of wild-type and *Dgcr8* KO mESCs. This will allow me to see the contribution of the above two cell lines to chimeras. These eGFP ESCs were microinjected in a morula stage embryo. As expected, both wild-type and *Dgcr8* KO ES cells contributed to the chimera. The contribution of *Dgcr8* KO eGFP donor cells to the ICM was more compared to wild-type eGFP donor cells. The reason for this might be that *Dgcr8* KO ES cells might be more pluripotent as they are stuck in the pluripotent network and have lost the capacity to differentiate[142] **(Figure 17)**.

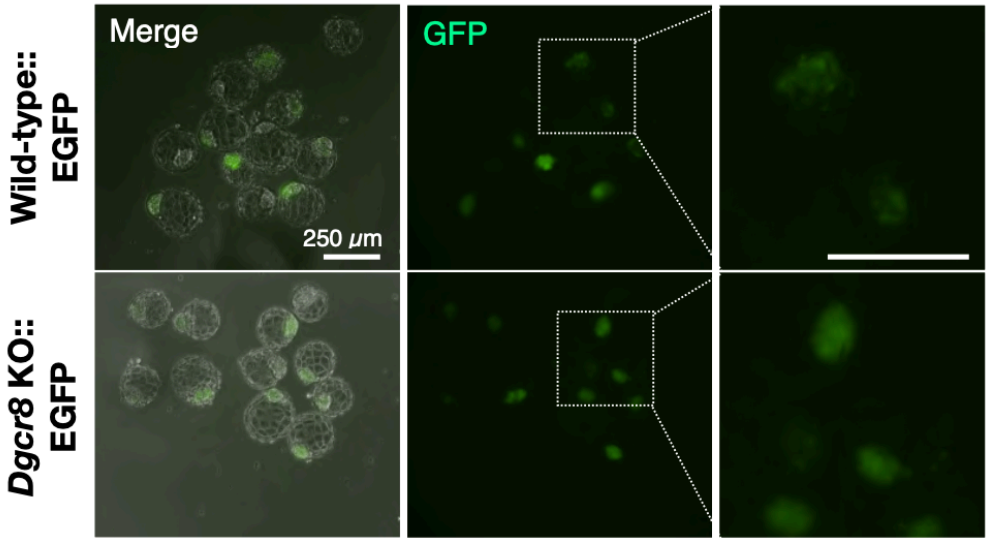

Figure 17. Characterization of wild-type and *Dgcr8* KO chimeric embryos.
Brightfield and/or fluorescence images of wild-type and *Dgcr8* KO chimeric embryos before mTORi (Rapalink-1). EGFP signals show the contribution of ESC to the ICM. Both wild-type and *Dgcr8* KO ESCs contributed to the ICM of the chimeric embryo. The contribution of *Dgcr8* KO ESCs was more to the ICM compared to wild-type ESCs. Right panel shows high magnification image. Scale bar = 250μm.

When the above embryos reached the blastocyst stage, they were divided into 2 groups for treatment with either DMSO (controls) or mTORi and the survival of the blastocysts was scored everyday. Blastocysts with intact blastocoel with no signs of fragmentation were considered intact. As expected, DMSO-treated embryos did not survive for long and collapsed in culture as the culture was not conducive for prolonged blastocyst survival (median survival of 4 days and maximum survival of 5 days after blastocyst expansion) **(Figure 18 Left)**. mTORi-treated wild-type embryos paused development and survived for a maximum of 12 days in culture **(Figure 18 Left)**.

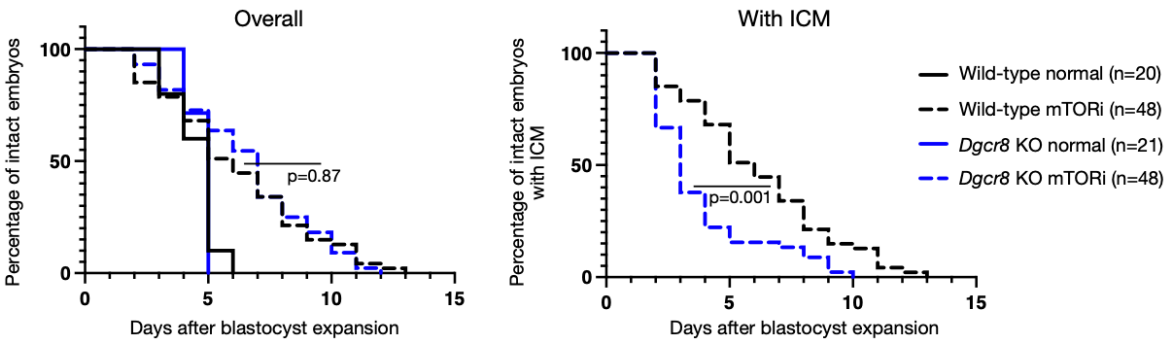

Figure 18. Survival curves of wild-type and Dgcr8 KO chimeric embryos under mTORi-induced pausing condition. Left: all intact embryos. Right: embryos with visible ICM. All the wild-type chimeric embryos undergoing dormancy retained their ICM. Most of the Dgcr8 KO chimeric embryos lost their ICM within 5 days of mTORi-induced pausing. Statistical test is Mantel-Cox test, where wild-type chimeric embryos were used as the reference data set.

Surprisingly, mTORi-paused *Dgcr8* KO embryos had very similar overall blastocyst survival to wild-type embryos **(Figure 18 left)**. Upon close observation of mTORi paused *Dgcr8* KO embryos, I found that about 80% of these embryos lost their ICM within 4 days of mTORi treatment **(Figure 18 Right and Figure 19)**. This phenotype closely resembles the *in vitro* collapse of *Dgcr8* KO cells in culture.

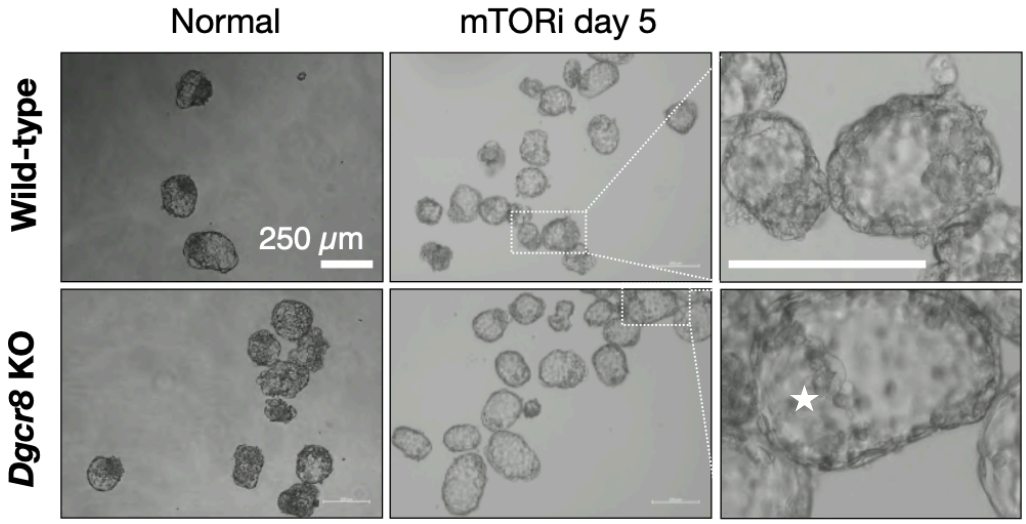

Figure 19. Bright-field images of wild-type and Dgcr8 KO chimeric embryos on day 5 of mTORi-induced pausing. Right panel shows a higher magnification image of the area marked with white boxes. Dgcr8 KO chimeric embryos lack a visibly large ICM area on day 5 of mTORi pausing (see area marked by a star). Scale bar = 250μm.

To confirm the ICM collapse in paused *Dgcr8* KO embryos, I performed immunofluorescence (IF) for Nanog – a marker for pluripotency expressed specifically in ICM cells. IF showed that some *Dgcr8* KO embryos lacked ICM while the others had cells in the ICM region having no Nanog expression **(Figure 20)**. Thus, showing that canonical miRNAs processed by DGCR8 are critical for embryo transition into dormancy. This was evidently seen in the DIPLO embryos where ICM cells devoid of canonical miRNAs fail to undergo diapause upon mTORi and collapse just like the *Dgcr8* KO ES cells in culture. The results also shed light on the differential dynamics of TE with respect to ICM, where the survival of TE is not dependent on the ICM of the embryo during diapause and continues to grow as trophectoderm shells.

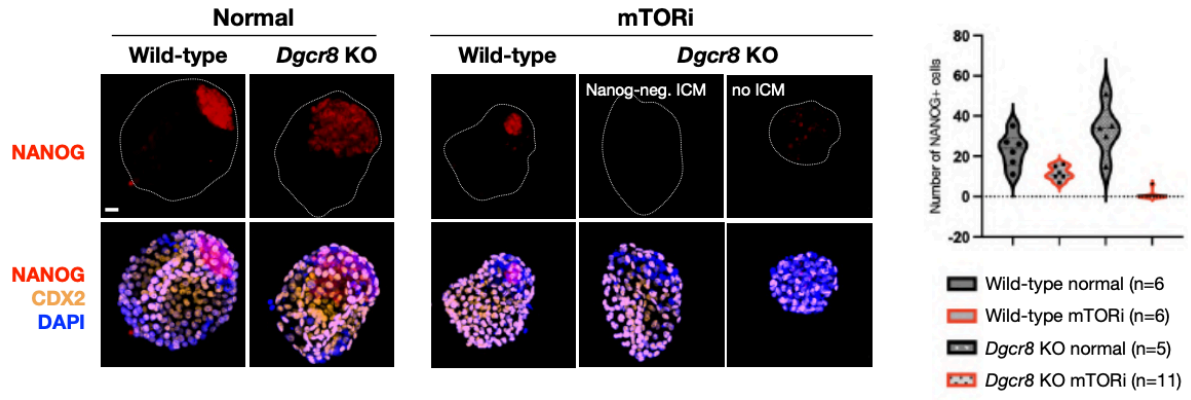

Figure 20. Immunofluorescence staining of wild-type and *Dgcr8* KO chimeric embryos in normal and day 3 mTORi paused conditions. The embryos were stained for epiblast marker NANOG, trophoblast marker CDX2 and the DNA stain DAPI. The right panel shows the number of NANOG+ cells present for each condition. Between 5 and 11 embryos were stained in each group. The wild-type epiblast reorganizes into a more compact state during mTORi pausing. Dgcr8 KO embryos treated with mTORi either lack ICM or have NANOG- cells. Scale bar = 20µm.

1.3 *Dgcr8* KO ESCs show an aberrant transcriptome and differentiation propensity under mTORi-induced dormancy

Through the above data, I was able to phenotypically show the indispensability of miRNA function at the time of entry into dormancy where miRNA null cells compared to their wild-type mESC counterpart collapse under mTORi culture condition. This led me to hypothesize that under mTORi, *Dgcr8* KO cells are unable to suppress their global transcription like the wild-type paused cells. To validate the hypothesis, I performed 5-Ethynyl uridine (EU) incorporation assay in wild-type and *Dgcr8* KO cells under normal ESC culture and after 48h of mTORi treatment (most of the *Dgcr8* KO cells die after this time point). The method employs the incorporation of EU a nucleoside analog in nascent synthesized RNA to measure the global transcription in a given system. The detection of EU is based on click chemical reaction which utilizes a fluorescent azide group that binds to the alkyne moiety in the EU catalyzed by copper to give a fluorescent signal. *Dgcr8* KO cells were able to suppress global transcription just like the wild-type cells under mTORi **(Figure 21)**.

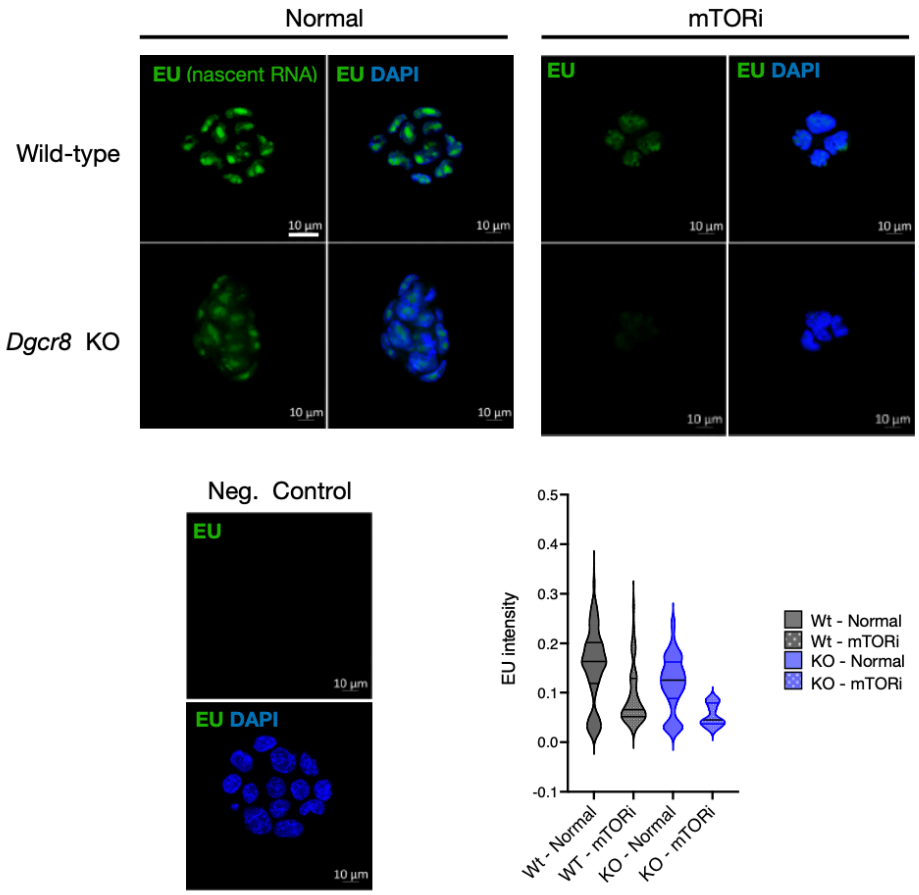

Figure 21. Confocal analysis of nascent RNA levels of wild-type and *Dgcr8* KO ESCs in normal or mTORi-induced pausing conditions. Cells before fixation were labeled with a nucleotide analog EU. After fixation, they were subjected to click chemistry where a fluorescent azide binds to the EU catalyzed by copper to give a fluorescent signal. Negative control in the bottom left panel did not receive EU but was subjected to all the downstream steps. Scale bar = 10µm. The graph on the bottom right panel measures mean fluorescent intensity at single-cell resolution. CellProfiler was used to mark the nuclei using DAPI as reference and EU intensity was measured within the marked nuclei.

The above result then brought me to my second hypothesis – whether the death of *Dgcr8* KO cells under mTORi was mediated by the p53-MDM2 axis[143]. To investigate this, I performed immunofluorescence (IF) for p53 and MDM1 on wild-type and *Dgcr8* KO cells under normal ESC culture and after 48h of mTORi treatment. I chose to do IF over western blot (WB) as this was the fastest way to check for the hypothesis with minimal cell number requirement as it is difficult to collect large cell numbers for 484h Dgcr8 KO cells under mTORi.

IF results did not show any p53-MDM1dependent cell death. In fact, p53 was expressed at a low basal level in *Dgcr8* KO cells compared to wild-type cells **(Figure 22)**.

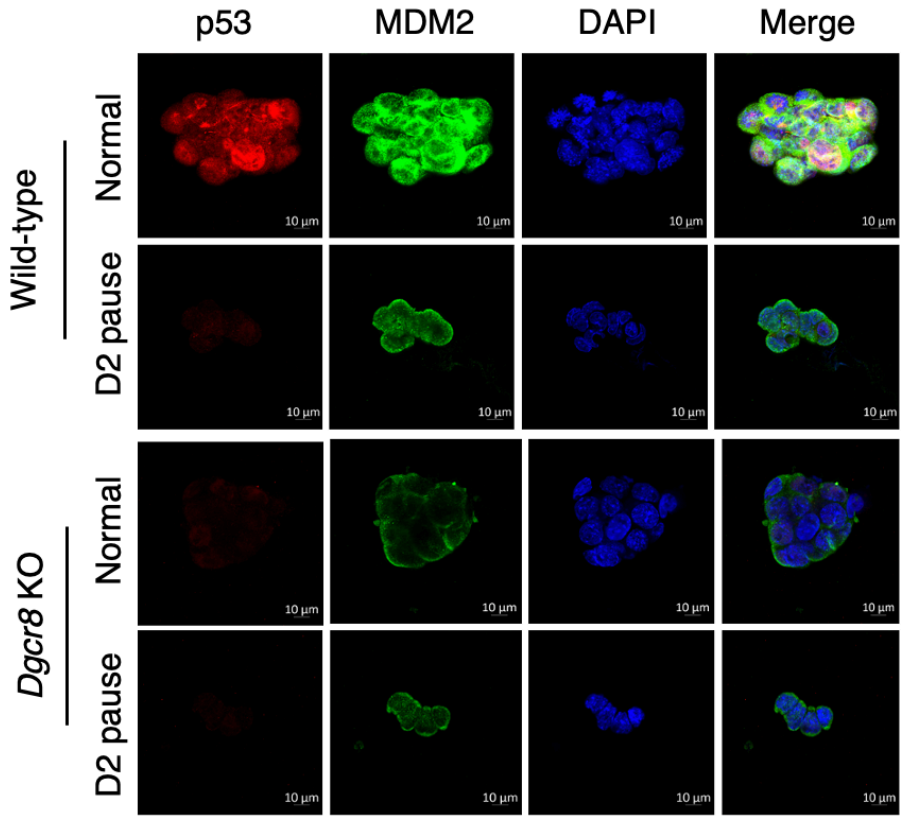

Figure 22. Immunofluorescence of p53 and MDM2 in wild-type and Dgcr8 KO mouse ESCs under normal and mTORi-induced pausing. Wild-type ESCs under normal conditions show high expression of p53 and MDM2 and their expression levels drop in diapause condition. In contrast, *Dgcr8* KO ESCs to begin with have low expression of p53 and MDM2 in normal culture conditions and their expression levels do not change in diapause conditions. Scale bar = 10µm.

In order to get an insight into the collapse of *Dgcr8* KO ESCs under mTORi, I decided to perform bulk RNA-seq on wild-type and *Dgcr8* KO cells under normal ESC culture and after 48h of mTORi treatment, which would tell me how KO of *Dgcr8* affect gene expression changes and different pathways utilized by these cells under mTORi culture conditions. The analysis was done by Francisca Ringeling (Stephan Canzar lab, Pennsylvania State University). Tximport was used to summarize transcript abundance for gene-level analysis. Differential gene expression was performed using DESeq2.

Principal component analysis revealed the genetic background as the primary variable (PC1: 79% variance), and mTORi vs normal conditions as the secondary (PC2: 14% variance) **(Figure 23 A)**. Wild-type and *Dgcr8* KO cells showed a similar distribution of significantly differentially expressed (DE) genes, with KO cells showing more DE genes **(Figure 23 B)**.

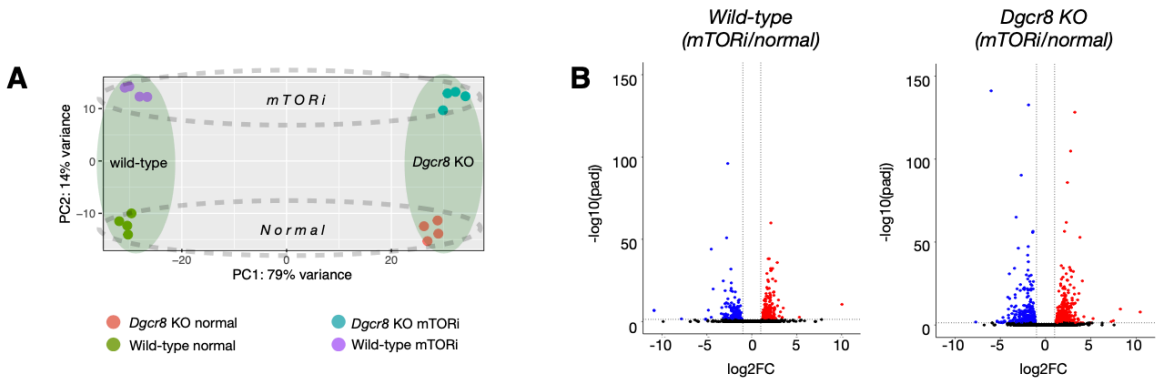

Figure 23. Dgcr8 KO mouse ESCs show aberrant transcriptome.
A. The PCA plot of wild type and Dgcr8 KO ESCs in normal and mTORi (day 2) conditions. Most of the *Dgcr8* KO cells die on day 3 of pausing. The plot shows Dgcr8 KO cells under normal conditions have aberrant transcriptome with PC1 showing 79% of variance.
B. Volcano plot showing differentially expressed (DE) genes in wild-type and *Dgcr8* KO cells under normal and mTORi conditions (padj<0.05, log2FC>1). Dgcr8 KO cells showed more DE genes (738 vs 403 in wild type and 153 common) and an overall higher significance level.

To overcome the strong association of transcriptome with genetic background, a two-step approach was taken to identify biological processes in *Dgcr8* KO cells that are different from wild-type cells under mTORi. For this, first, the DE genes (mTORi/normal) were identified in wild-type and KO cells. Then gene ontology (GO) analysis was performed for the functional allocation of these genes to cellular processes. The GO terms retrieved were then compared and defined as common in both wild-type and *Dgcr8* KO cells or specific to each of the mentioned cell types **(Figure 24)**.

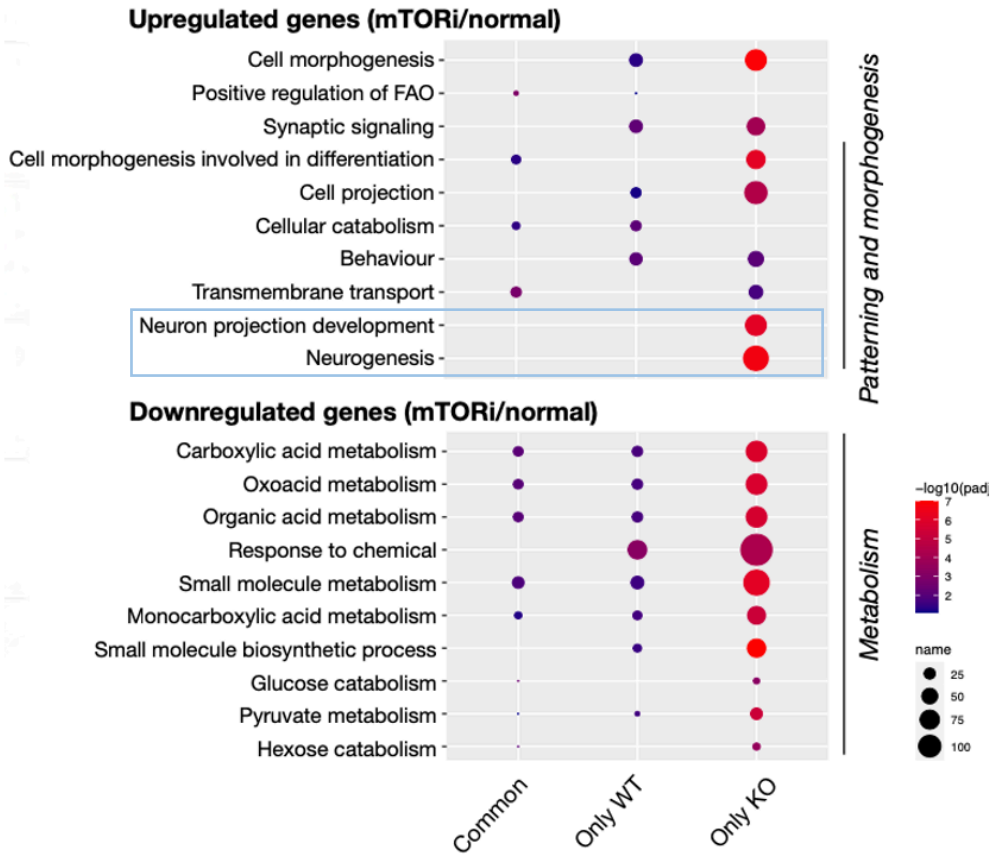

Figure 24. Dgcr8 KO mouse ESCs show aberrant transcriptome.
Gene ontology analysis of significantly upregulated or downregulated in wild-type and *Dgcr8* KO ESCs under normal and mTORi conditions. Pathways that are commonly regulated in both cell types are shown together with the ones that are differentially expressed based on genetic background.

The RNA-seq data revealed aberrant upregulation of genes involved in development progression in *Dgcr8* KO cells. Failure of these cells to rewire their transcriptome correctly because of the absence of miRNAs, results in abnormal expression of differentiation genes along with genes involved in pluripotency which can alter the state and stress response of the cell. These are the probable reasons for the collapse of *Dgcr8* KO cells under mTORi. These analyses thus further revealed a need for miRNAs for fine-tuning gene expression for the transition of pluripotent cells into dormancy **(Figure 24)**.

1.4 Single-embryo profiling reveals rewiring of global miRNA expression in dormancy

Through the above results, it was clear that the fine-tuning role played by miRNAs is essential for successful and efficient entry into diapause by pluripotent stem cells. As revealed in RNA-seq data, with no miRNAs in play, there was a dysregulation of gene expression causing some of the lineage-specific genes to get activated which impedes cells from undergoing quiescence. Ultimately leading to cell death under mTORi condition as seen in *Dgcr8* KO mESCs.

Acknowledging their indispensable role in diapause induction, I set out to profile miRNAs with high sensitivity using ultra-low input small RNA sequencing **(Figure 25)**.

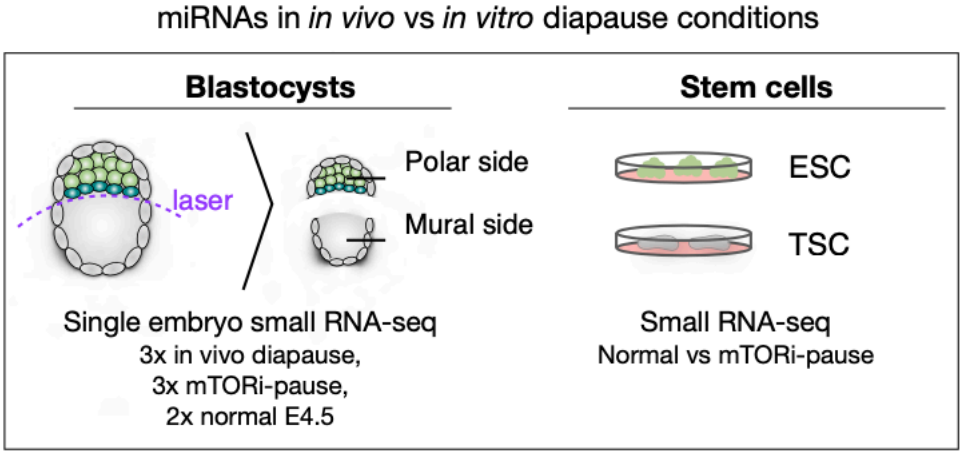

Figure 25. Schematic showing sample preparation for small RNA sequencing.
In vivo, *in vitro* and normal E4.5 mouse blastocysts were laser dissected to separate the polar from the mural side. ESCs and TSCs were cultured under normal conditions and mTORi conditions. Small RNA sequencing for different parts of the embryo was done along with ESCs and TSCs via low-input small RNA sequencing kit.

Diapausing mouse embryos show a large degree of heterogeneity in morphology and survival. This heterogeneity can contribute to differential miRNA expression between individual diapausing embryos. For this reason, I used single embryos for global profiling of miRNAs. Normal late E4.5 mouse blastocysts were used as controls. I included both *in vivo* and *in vitro* paused blastocysts (EDG7.5 – equivalent day of gestation 7.5) for miRNA profiling. The reason is that since dormancy is a complex process, the method by which dormancy is brought about might also reflect on the miRNA expression profile. *In vivo* diapause was induced via ovariectomy, followed by progesterone injections. *In vitro* diapause was induced via mTOR inhibition. Both these types of diapaused embryos were profiled side by side with normal embryos.

Another important thing to be considered is that miRNAs show tissue-specific expression. It is known that the placenta has its own unique miRNA signature[144,145]. Based on this I reasoned that trophectoderm (TE) cells would have a unique set of miRNAs than ICM cells. In addition, TE tissue is not of a uniform state and rather comprises more naive vs committed cells at the polar and mural ends, respectively. Mural TE shows lower mTOR activity and ceases to proliferate sooner than the polar TE in diapause, attesting to the distinct dynamics of the mural and polar TE. Furthermore, mouse embryos implant from the mural end. For these reasons, with the help of the Transgenic Facility of the Max Planck Institute, I chose to dissect the blastocysts into polar and mural parts and profile small RNAs with higher spatial resolution **(Figure 25)**. Blastocysts were laser dissected to separate the ICM and the adjacent polar TE from the mural TE. In addition to blastocysts, I also profiled the ESC and trophoblast stem cells (TSCs) as in vitro derivatives of the ICM and TE respectively of the embryo. With this experimental design, I aimed to address three main questions: **1)** Do in vivo- and in vitro-diapaused embryos show similar miRNA expression profiles? **2)** Do stem cells and embryos

show similar miRNA expression profiles? **3)** Which miRNAs show consistent expression patterns across conditions?

For this small RNA libraries with a size ranging from 15 to 150 nucleotides were selected for downstream sequencing and analysis. miRDeep2 (v2.0.1.2) algorithm was applied for the quantification of miRNAs across samples, using the reference annotations of mature and hairpin miRNAs from miRBase (version 22). Across samples, an average of 44.5% of reads were aligned and considered for downstream miRNA profiling.

To access the similarity of miRNA expression profiles across all samples, my colleague Lambert Moyon (Marsico lab, Helmholtz Zentrum, Munich) performed principal component analysis (PCA) **(Figure 26)**.

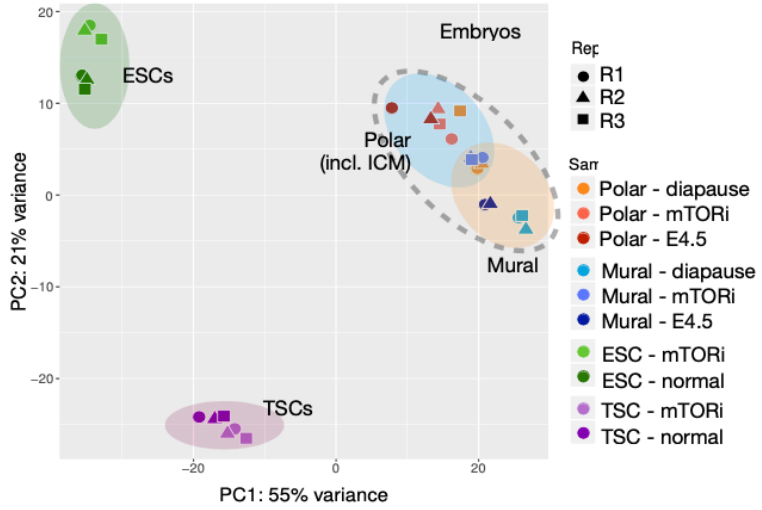

Figure 26. PCA plot showing small RNA data sets. Stem cells and embryos are separated along PC1 (55% variance). The polar embryo which includes ICM clusters closer to ESCs. The mural embryo clusters closer to TSCs. Showing small RNA profiles reflective of tissue of origin.

Embryonic samples were clearly separated from stem cells on PC1 (55% variance), yet ESCs and TSCs were more proximal to their corresponding tissues on PC2 (21% variance). Within the embryonic cluster, the polar and mural profiles clustered separately. Inter-embryo variability was minimal in the mural part and more pronounced in the polar part, hinting at more dynamic regulation. *In vivo* diapaused embryos showed higher variability compared to in vitro diapause **(Figure 26)**.

To identify specific patterns of miRNA expression, differential expression analysis was applied comparing each set of diapause conditions against the control. This differential expression analysis was done separately for cells representing embryonic and extraembryonic fate. miRNAs with a read count of more than 5 in at least 3 replicates were kept and the rest were discarded from the analysis. The read counts were then transformed into log counts for differential gene analysis. DE genes were then identified with threshold log2 $\geq$ 1.5.

Hierarchical clustering was then applied to identify miRNAs that are up or downregulated across conditions and sample types **(Figure 27)**.

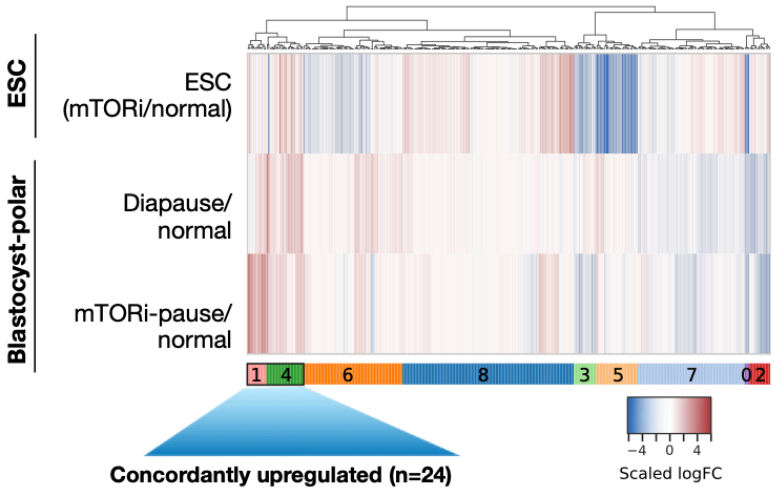

Figure 27. Heat map showing miRNA expression profiles. miRNA expression profile changes in diapaused (*in vivo* and *in vitro*) compared to normal E4.5 blastocysts (polar) and in paused ESCs when compared to normal ESCs. miRNAs were grouped into 9 clusters based on expression levels in three replicates. The clustering is done based on the silhouette score (see methods). Clusters 1 and 4 show 24 miRNAs having concordant upregulated trend.

The analysis showed that miRNA expression profiles in *in vivo* and *in vitro* diapause embryos were closely related when compared to stem cells which showed less similarity. This suggests that tissue complexity and culture conditions might also contribute to the miRNA expression pattern. A total of 35 miRNAs showed positive log2FoldChange. These miRNAs belong to clusters 1 and 4 across comparisons of polar embryos and ESCs **(Figure 27)**. We could not find such a high correlation in the mural part of the embryo or in the TSCs.

Overall, the polar embryo and ESCs show more dynamic changes compared to TSCs and mural embryos in response to dormancy cues and therefore are the focus of the rest of the study.

Amongst the 35 miRNAs in the two clusters, a subset of 24 miRNAs were each concordantly upregulated in all dormant samples **(Figure 28)**. MicroRNAs 200a/b/c, miRNA 141 (miRNA 200 family), miRNA 26b-5p and miRNA 429 among others were highly enriched in the subset of 24 miRNAs. Taken together, these results reveal dynamic miRNA alterations upon dormancy induction and show that in vitro embryonic diapause largely recapitulates the miRNA regulation of the in vivo phenomenon.

Top 15 concordantly upregulated miRNAs (pause/normal)					
	diapause	mTORi-embryo	mTORi-ESC	avg log2FC	cluster
mmu-miR-1839-5p	2.03	1.60	1.63	1.75	4
mmu-miR-205-5p	0.57	3.85	0.74	1.72	1
mmu-miR-26b-5p	0.56	1.46	3.08	1.70	4
mmu-miR-23a-3p	1.31	2.98	0.55	1.61	1
mmu-miR-27b-3p	1.19	2.91	0.71	1.60	1
mmu-miR-676-3p	2.50	1.42	0.71	1.54	4
mmu-miR-200b-5p	1.86	0.39	2.12	1.46	4
mmu-miR-200b-3p	1.23	1.42	1.42	1.36	4
mmu-miR-200c-3p	1.19	0.98	1.87	1.34	4
mmu-miR-30b-5p	1.41	2.20	0.41	1.34	1
mmu-miR-200a-3p	1.52	1.45	0.84	1.27	4
mmu-miR-141-3p	1.58	1.67	0.54	1.26	4
mmu-miR-148a-3p	0.84	1.16	1.73	1.24	4
mmu-miR-30d-5p	1.32	1.13	0.91	1.12	4
mmu-miR-429-3p	1.46	0.45	1.40	1.10	4

Figure 28. Top 15 concordantly upregulated miRNAs and their log2FC values in each condition.

To corroborate the miRNA expression changes in dormancy with an independent approach, we additionally performed Nanostring on ESCs. The amplification-free sample preparation for Nanostring allows us to avoid the artifacts that arise from library preparation for Illumina sequencing. We compared miRNA expression profiles of mTORi-treated vs control ESCs generated by RNA-seq and Nanostring. Both approaches yielded similar expression patterns, with miR-200 family and miR-26b-5p miRNAs among the top upregulated miRNAs in both assays. This multi-tissue, multi-approach characterization thus revealed a common regulatory base of concordant upregulated miRNAs for both *in vivo* and *in vitro* diapause embryos and mESCs **(Figure 29)**.

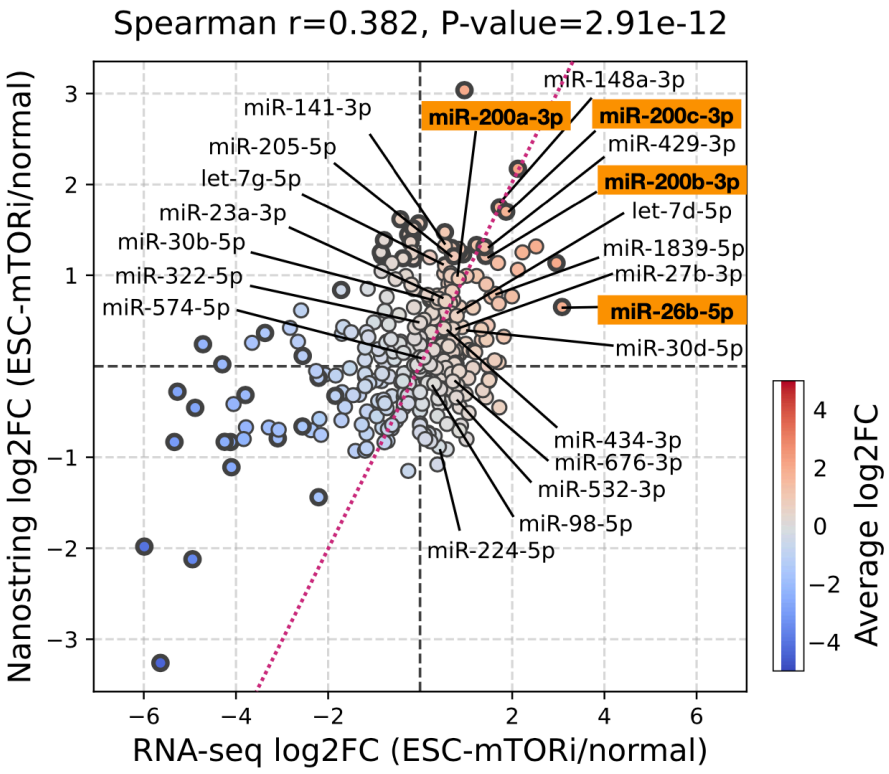

Figure 29. miRNA expression profiles via amplification-free Nanostring analysis.
Comparison of miRNA expression profiles resulting from small RNA seq and Nanostring analysis shows a correlation of miRNA expression between the two assays. miR-200 family showed the highest fold change in both assays.

1.5 Constructing the miRNA-protein network of dormancy

The data from small RNA sequencing sheds light on the miRNAs that are enriched in mouse embryos and mESCs during the transition into dormancy. My curiosity drove me to find out how these miRNAs function and regulate their target genes during the onset of dormancy. It is known that miRNAs have a coordinated function fine-tuning many cellular processes simultaneously. To get a macroscopic view of miRNA-regulated cellular processes, Lambert used an unbiased approach to construct an *in silico* post-transcriptional regulatory network of miRNA and their potential target proteins **(Figure 30)**.

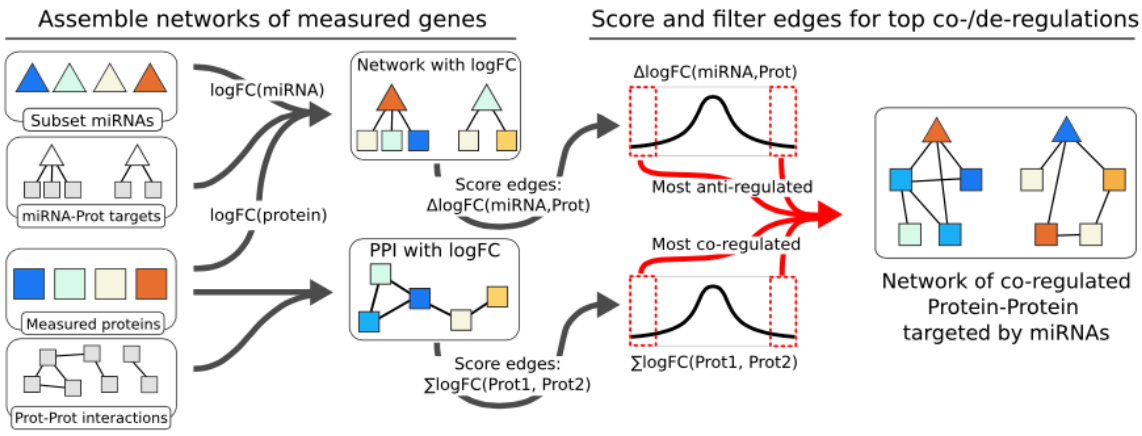

Figure 30. Schematics of the computational analysis to construct the network.
From the measured logFC of proteins and miRNAs, scores are assigned to edges to assess concordant (for protein interactions) or discordant regulation (miRNA-target interactions). Comparison of actual scores to a distribution from random pairings enables the identification of the most extreme edge scores to keep in the final network.

We integrated the proteome data obtained from mTORi-treated and control ESCs with miRNA expression data. miRNA-protein interactions were extracted from miRDB where medium and high confidence interactions were retained and from miRTarBase where experimentally validated functional miRNA-protein interactions were considered. protein-protein interactions (PPIs) were extracted from BioGrid, together with top-scoring interactions from StringDB. High-confidence interactions (see Methods) were exclusively used to connect genes ("nodes"), and the log2FC values of connected genes were used to score connections ("edges") between these genes. Finally, by keeping the highest scoring edges, we were able to extract connections of the highest concordance (protein-protein) or discordance (miRNA-proteins) in terms of expression changes during pausing. Of note, downregulated miRNAs were not included in the network construction, since our goal was to identify miRNAs that are specifically induced at the time of diapause entry and their putative protein targets. To identify the most significant miRNA-mediated changes during dormancy, we established two distinct criteria for scoring miRNA-target interaction and protein-protein interactions. For miRNA-target interaction, the edges are scored such that the changes in target gene expression are inversely correlated or changes are discordant with microRNA expression. In other words, miRNA-target edges are scored by subtracting log2FC of protein target from log2FC of the connected miRNA. This results in high-scoring edges when a positively regulated miRNA is connected to a negatively regulated protein. For scoring PPI edges, the emphasis lies on the co-expression of the interacting proteins. The explanation for the scoring stems from the idea that perturbations caused by miRNA may ripple through protein complexes and cellular pathways.
From an initial network of 24 upregulated miRNAs and 4,346 proteins, we filtered for the top 10% of miRNA-target edges and the top 1% of PPIs, thus extracting a significantly deregulated network comprising 335 PPIs and 196 miRNA-target connections **(Figure 31)**.

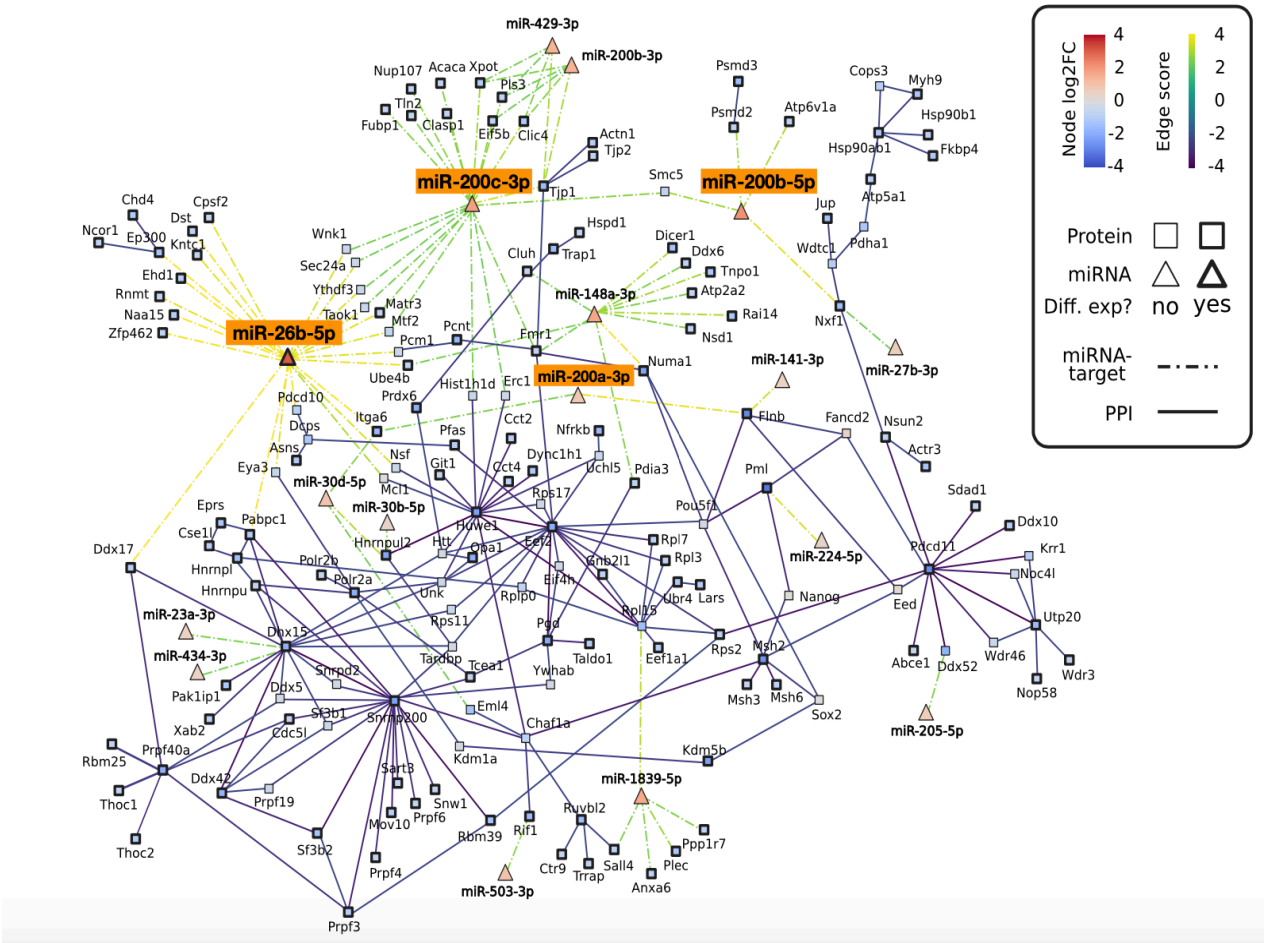

Figure 31. miRNA-protein network showing concordantly upregulated miRNAs and their significantly downregulated proteins. A stringency cutoff is applied to keep the top 10% of miRNA-target edges, and the top 1% of protein-protein interactions. P-value = 1.327e-30 from Fisher exact test (one-sided) for enrichment in differentially expressed protein.

After applying the cutoffs, the network is enriched in significantly differentially downregulated proteins (119 out of the 431 retained proteins, one-way Fisher's Exact test p-value = 1.327e-9), while also capturing the majority (17 out of 24) of miRNAs showing positive change in expression during pausing in both ESCs and embryos. miR-200 family miRNAs emerged as one of the prominent candidate regulators within the network, with miR-200b-5p and miR-200b-3p ranking as second and third highest-scoring miRNA-target. miR-200c-3p is also a prominent regulatory network's hub. Other miR-200 family miRNAs miR-200a-3p, miR-141-3p, and miR-429-3p are also part of the network. The hub node miR-26b-5p is the most up-regulated miRNA in the network and PML among others is one of the most down-regulated proteins **(Figure 31)**.

This network illustrates combinatorial miRNA activity during the dormancy transition, with single miRNAs relating to several target genes (e.g. miR-26b-5p) and multiple miRNAs relating to the same target genes (e.g. Ythdf3). Additionally including the PPIs allows one to visualize how regulatory relationships between miRNA and direct target genes propagate and

affect other proteins belonging to different cellular pathways through protein-protein interactions **(Figure 31)**.

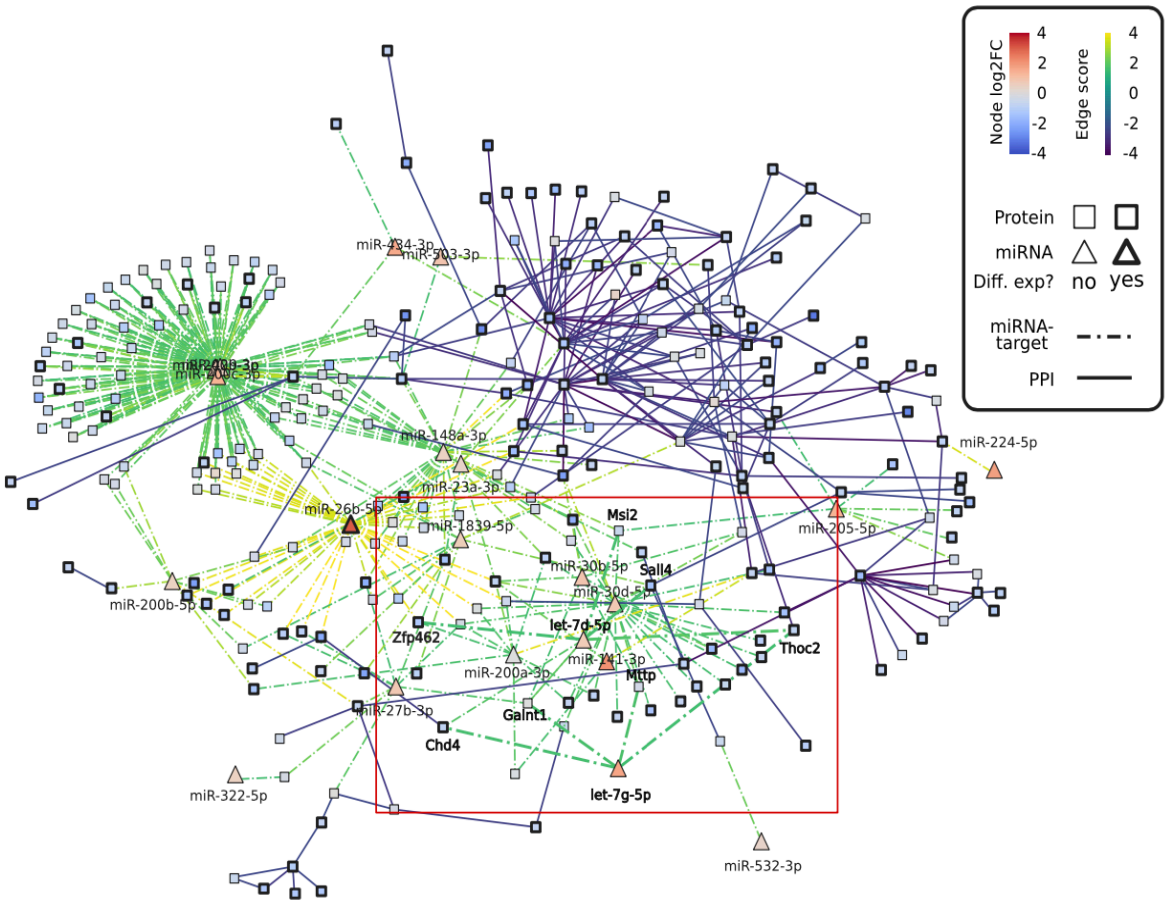

Figure 32. A less stringent miRNA-protein network includes let-7 miRNA.
Let-7, a previously reported miRNA associated with mouse diapause, is visible in this network, however, does not pass the stringency threshold in the main network in Figure 31. A total of 8 target proteins are found, including significantly downregulated proteins Cdh4 (logFC=-1.107, adjusted-P-value=0.0048) and Thoc2 (logFC=-1.048, adjusted-P-value=0.017) targeted by both let-7-d-5p and let-7-g-5p, while Sall4 (logFC=-0.862, adjusted P-value=0.0172) and Zfp462 (logFC=-0.791, adjusted-P-value=0.011) are additionally targeted by let-7-d-5p.

MicroRNA let7 which has been reported to alter development timing in mouse embryos[115]shows up only when we lower the threshold of miRNA-target (nodes) from 10% to 30% cutoff **(Figure 32)**. The upregulation of let7 and downregulation of its targets were less significant when compared to other candidate miRNAs identified in the stringent core network. So, we excluded it from further analysis.

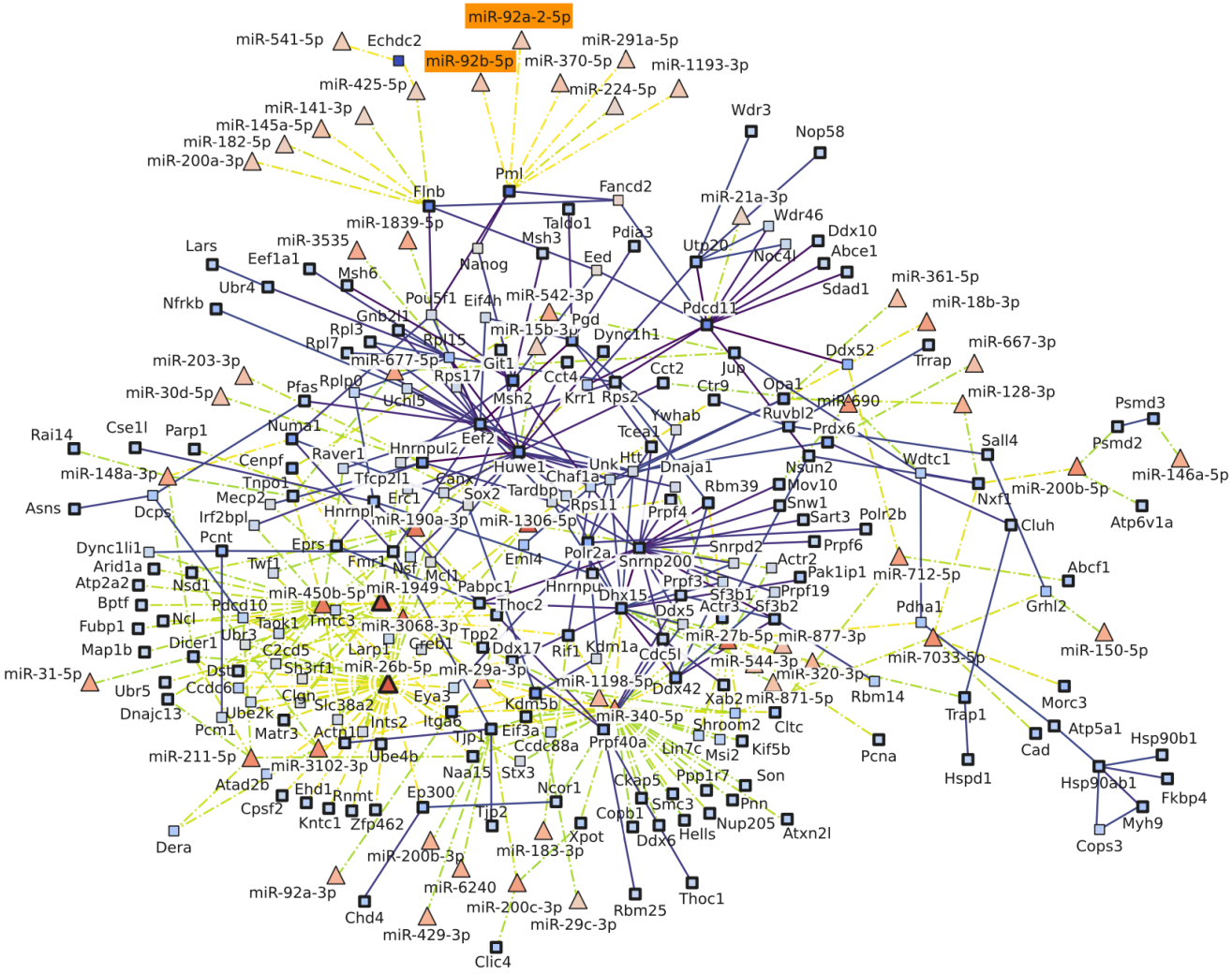

Figure 33. miRNA-protein network in mouse ESCs.
miRNA expression and proteome profiles of mTORi vs normal ESCs were used to construct the ESC-only network. The same stringency cutoff (top 10% of miRNA-target edges, and top 1% of PPIs) as the main network (Figure 31) was applied. In addition to miR-200 family and miR-26, this network also shows an evolutionarily conserved regulator of quiescence, miR-92.

Earlier it was pointed out that tissue complexity and culture conditions might also contribute to the miRNA expression pattern. Based on this we decided to generate a separate miRNA-protein network for the ESC diapause model. The idea was to identify miRNAs that could have been overshadowed in the above-core network. The network showed a unique set of 44 miRNAs and 108 new gene targets. Many of these ESC-specific upregulated miRNAs were found in higher proportion in high-scoring interactions with proteins from the above stringent core network. For example, PML was additionally targeted by miR-370-5p, miR-92b-5p, miR-1193-3p, miR-291a-5p, and miR-92a-2-5p, amongst the top 25 highest scoring connections. Interestingly, miR-92, which is an insulin-dependent regulator of L1 diapause in C.elegans[146], was found upregulated in paused ESCs and is part of the ESC network **(Figure 33)**, suggesting a prominent role in pluripotent cells.

The above miRNA-protein network built on miRNA and protein interaction predicts the underlying molecular mechanism that could function in a diapausing mouse embryo and mESCs. This network could serve as a guide to identify upstream and downstream regulators of miRNA regulation.

1.6 Network perturbation by manipulation of individual nodes leads to loss of pluripotent cells during dormancy transition

Until now I was able to show that miRNAs are important for mouse embryos and ESCs to transition into dormancy via mTOR inhibition. Removing the regulatory miRNA layer brings dysregulation of gene expression which impedes embryos and ESCs under mTORi conditions from undergoing quiescence. Along with Lambert, we shed light on the miRNAs that are enriched in mouse embryos and mESCs during the transition into dormancy and constructed an *in silico* post-transcriptional regulatory network of miRNAs and their potential target proteins.

Having the knowledge of miRNA network that functions during dormancy transition, I was curious to test the functional requirement of these miRNA during this cell state transition. I took advantage of the loss-of-function approach by using miRNA inhibitors to test their requirement during dormancy. The use of miRNA inhibitors was preferred **1)** To reduce the off-target effect caused by the CRISPR-cas9 system and **2)** To inhibit specific miRNAs of interest at the RNA level rather than at the genomic level.

I selected miR-26b-5p and miR-200 family as they are highly expressed during dormancy and predicted to have a large regulatory network **(Refer to figure 31)**. Together with the Transgenic facility at the MPIMG, I injected 2-cell stage embryos with inhibitors against the miR-200 family (pan inhibitor that targets all miR-200 members), miR-200 family together with miR26b-5p, or control inhibitors **(Figure 34)**. The reason for choosing a 2-cell stage embryo is because the rate of transcription is higher compared to zygotic embryos.

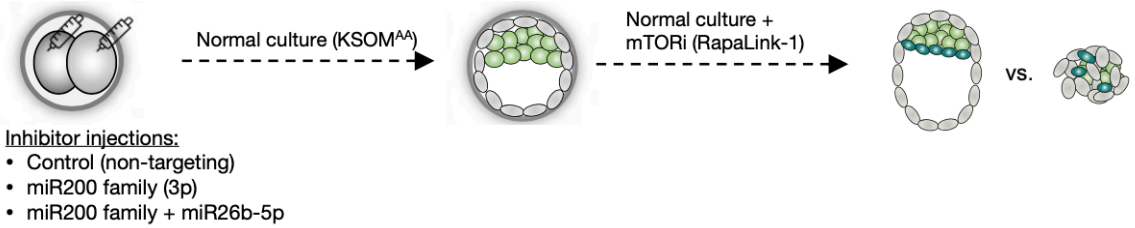

Figure 34. Schematic showing microinjection of antimiRs in 2-cell mouse embryos.
miRNA inhibitors (antimiRs) against miR-200 family and miR-26b-5p or a non-targeting control inhibitor were microinjected in 2-cell embryos. The embryos were allowed to reach the blastocyst stage under normal embryo culture conditions. After which, the blastocysts were treated with DMSO or mTORi (Rapalink-1) to induce *in vitro* diapause.

The injected embryos were allowed to reach the blastocyst stage in normal culture conditions and then treated with mTORi (using Rapalink-1). Survival analysis was done by scoring for intact blastocyst every day. I observed that inhibiting the miR-200 family and miR-26b-5p individually or together significantly reduced embryo survival compared to the control inhibitor. Most of the embryos collapsed within the first 5 days of diapause **(Figure 35 A)**. Immunofluorescence of inhibitor-treated mTORi paused embryos showed fewer NANOG+ positive cells than control embryos **(Figure 35 B)**.

The above results show that microRNAs are critical for the embryos to transcend into dormancy. I show here that, just perturbing a select few microRNAs from the core network can destabilize the dormancy process with specific loss of pluripotent cells and subsequent structural collapse of the embryos. This perturbation effect could further be amplified if more miRNAs from the core network are targeted. Here I also try to highlight the fact about robustness with which the microRNA network was created to give us a strong knowledge foundation of the microRNAs that are responsible for dormancy transition. Perturbing the network from any node could reduce the efficiency of *in vitro* dormancy.

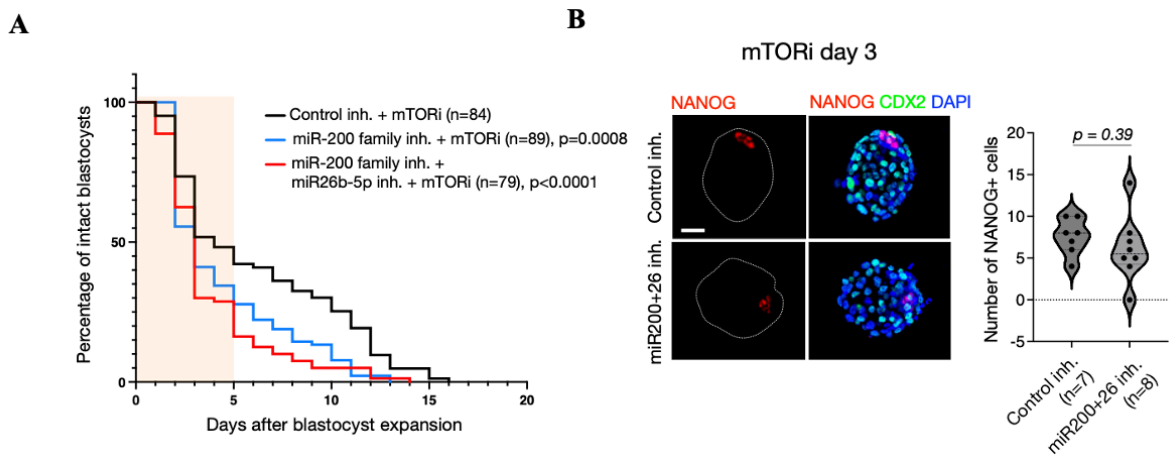

Figure 35. Combinatorial miRNA activity is essential for the transition into dormancy in mouse embryos.
A. Survival curves of embryos receiving target-specific or control antimiRs. The number of intact blastocysts was counted every day. Blastocysts with intact blastocoel and unfragmented TE were considered intact. Statistical test is Mantel-Cox test with control inhibitor+mTORi as the reference dataset. n, number of embryos.
B. Immunofluorescence of control-injected or antimiR-injected embryos on day 3 of mTORi treatment for epiblast marker NANOG, trophectoderm marker CDX2 and nuclear stain DAPI. The right panel shows the number of NANOG+ cells in each condition. n= 7-8 embryos were used. Statistical test is unpaired t test with Welch's correction. Scale bar = 20µm..

1.7 MicroRNAs can induce diapause in embryos independent of mTOR inhibition

Having identified the loss of function of miRNAs in mouse embryos confirms its functional requirement of miRNAs in dormancy transition. I next sought to explore the possibility of miRNAs on themselves bringing embryos into diapause without mTOR inhibition.

I chose miR-92 as a candidate miRNA since its ortholog miR-235 is associated with diapause in C. elegans [147]. miR-92 is transcribed from three distinct loci in the mouse genome on chromosomes 14, X, and 3, as miR-92a-1, 92a-2, and 92b respectively. Constitutively overexpressing miR-92 plasmids were generated by cloning the pre-miR transcripts under the control of the U6 promoter. With the help of the Transgenic facility of MPIMG, these plasmids were linearized and microinjected into the zygotic mouse embryos for stable expression **(Figure 36 A)**. Overexpression and processing of the hairpin into mature miR-92a-3p products were confirmed via Taqman qPCR **(Figure 36 B)**.

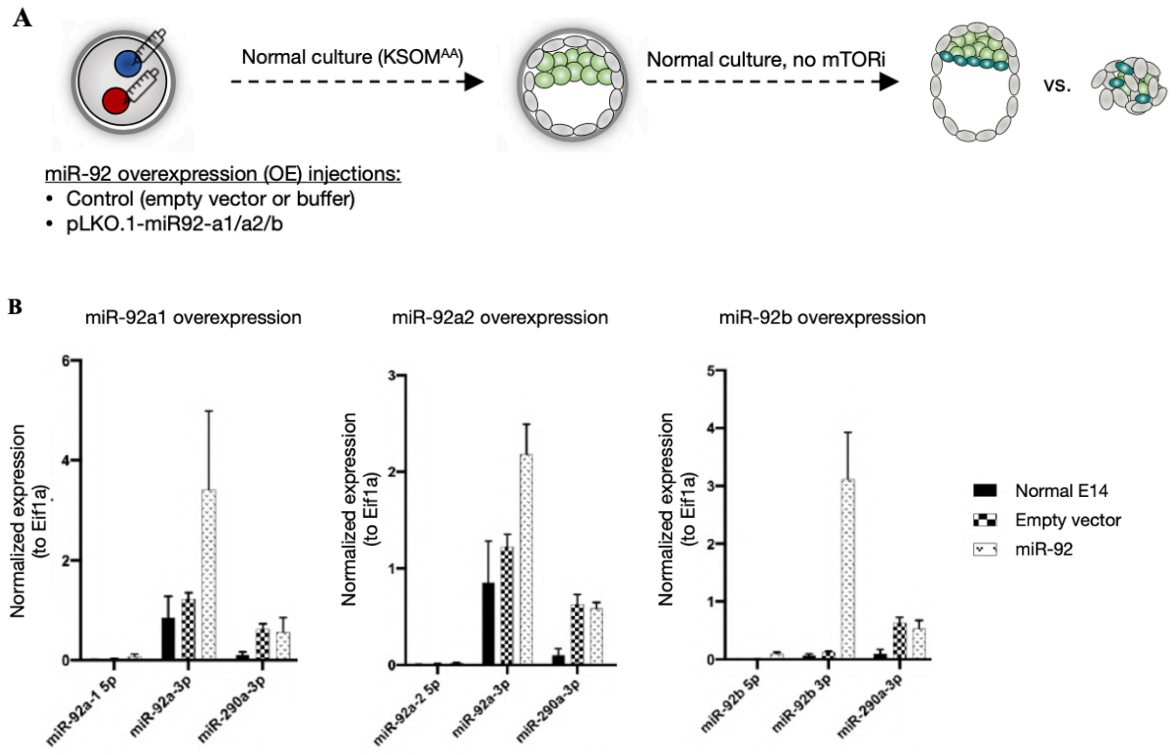

Figure 36. miR-92 can induce diapause independent of mTOR inhibition.
A. Schematic of miR-92 overexpression (OE). Zygotic pronuclei were injected with the linearized miR92 overexpression construct (pLKO.1 background, U6 promoter), empty vector, or injection buffer. The embryos were cultured in a normal embryo medium without mTORi until the end of the assay. The number of intact blastocysts was counted every day. Blastocysts with intact blastocoel and unfragmented TE were considered intact. **B.** qPCR validation of miR-92 overexpression.

Once the embryos reached the blastocyst stage, they were further cultured in base media without mTOR inhibitor and embryo survival was scored. miR-92a-2, miR-92a-1 and miR-92b were able to sustain blastocyst in culture until day 18, 15 and 10 respectively **(Figure 37)**. The above results point out the functional importance of miRNAs in regulating the developmental timing of mouse embryos on their own independent of mTOR inhibition and play a crucial role in stress response.

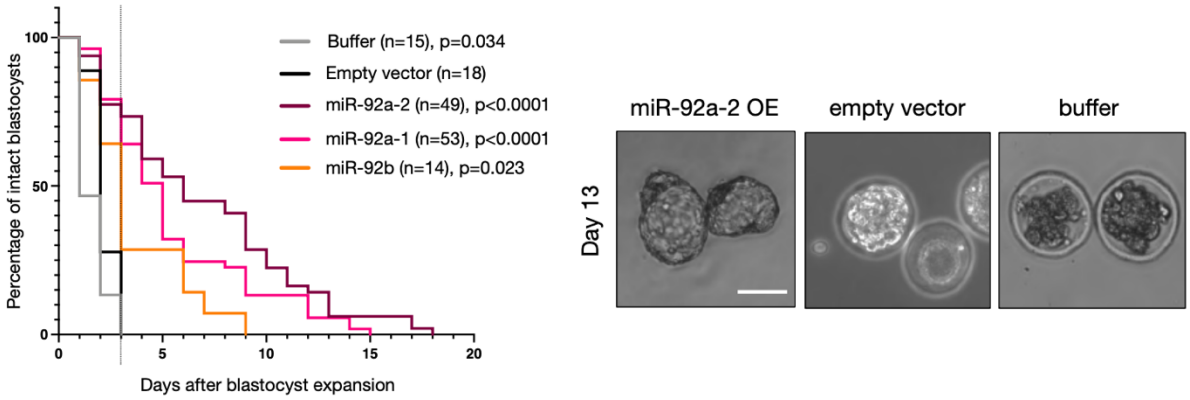

Figure 37. miR-92 can induce diapause independent of mTOR inhibition.
Left panel showing survival curves embryos miR-92 OE or control embryos. n, number of embryos in each group. Statistical test is Mantel-Cox test with empty vector injection as the control dataset. Right panel shows bright field images of miR-92 OE or control embryos on day 13 of in vitro culture without mTORi. Scale bar = 100µm.

1.8 Cellular bodies are downregulated during dormancy in wild-type mouse ESCs

Since I have shown that microRNAs are gatekeepers for dormancy entry in mouse embryos and ESCs and without them, there is aberrant gene regulation causing the embryos and cells to collapse during dormancy transition via mTORi. My next aim was to understand the cellular processes that are regulated by miRNAs during dormancy transition. The network above shows microRNA regulating its downstream protein targets. Instead of using individual nodes and edges to dissect the miRNA's regulatory role, Lambert functionally annotated the proteins via gene ontology analysis **(Figure 38 A)**. The network was strongly enriched for proteins involved in RNA splicing, RNA processing, chromosome organization and cell development. PML (of PML bodies) and DDX6 (of P-bodies) proteins which are major organizers of membrane-less cellular bodies and are involved in RNA splicing were found to be direct targets of miRNA and are predicted to be downregulated during diapause **(Figure 38 B)**.

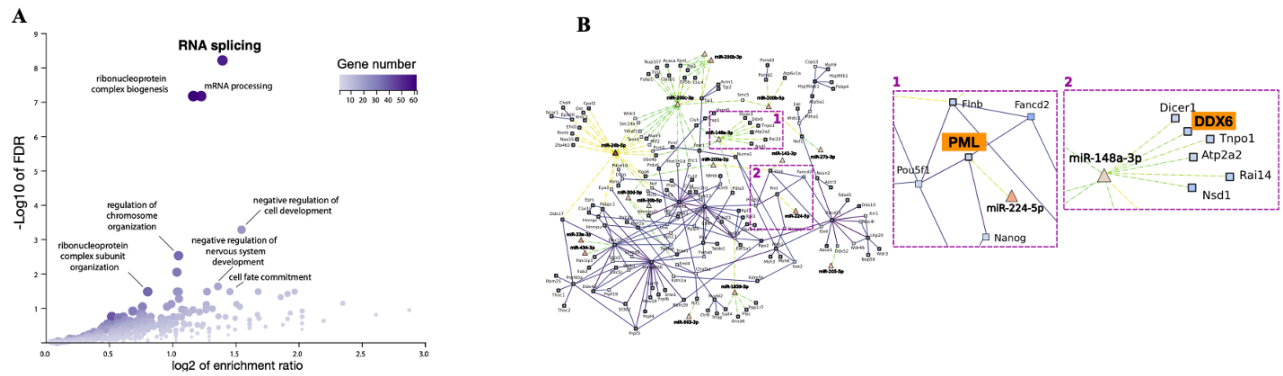

Figure 38. Gene ontology analysis of in-network proteins under putative miRNA control. A. RNA processing pathways comprise the most significantly altered pathways during diapause entry. RNA splicing is the top-altered pathway. **B.** Network map showing the in-network proteins chosen for IF validation.

To validate that these genes are downregulated at the protein level, I performed IF on wild-type and Dgcr8 KO cells under mTORi for 24h and 48h. I chose to do IF over western blot (WB) as this was the fastest way to validate with minimal cell number requirement as it is difficult to collect large cell numbers for 48h Dgcr8 KO cells under mTORi **(Figure 39 A and B)**. I chose SC-35 as a control stain for this experiment. SC-35 is a major component of another membrane-less RNA processing body called RNA speckles which does not show up in the miRNA-protein network. IF results showed that wild-type ESCs upon entry into dormancy were able to effectively down-regulate the expression of PML and DDX6. Whereas SC-35 was upregulated in paused wild-type ESCs **(Figure 39 A and B)**. In contrast, Dgcr8 KO cells under normal culture conditions expressed higher levels of PML and DDX6 and lower SC-35 expression when compared to wild-type ESCs. Upon entry into dormancy, Dgcr8 KO cells were able to down-regulate PML and DDX6 although the repression was not efficient. PML expression remained high in the surviving 1% of the population of Dgcr8 KO cells in 48h mTORi. The mean SC-35 expression remained the same in 24h paused Dgcr8 KO cells.

Here again, I highlight the fact about robustness with which the microRNA-protein network was created. It gives us a strong prediction of the molecular landscape that is in play during mouse dormancy establishment. From the above results, I was able to validate the network prediction of RNA processing proteins such as PML and DDX6 to be downregulated during the pausing of wild-type mESCs where their expression remains perturbed in Dgcr8 KO cells under both normal and mTORi conditions.

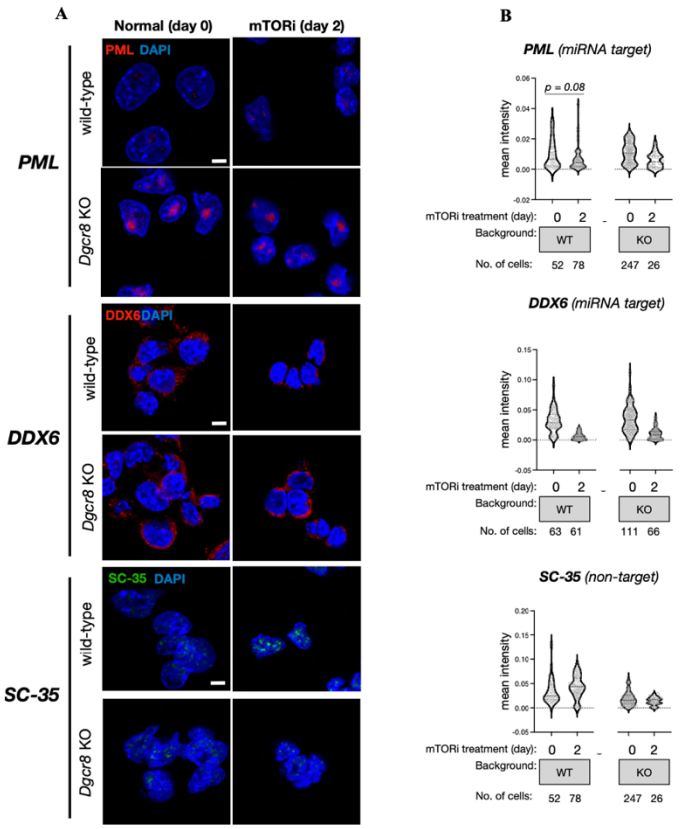

Figure 39. Inefficient repression of in-network RNA processing bodies PML and DDX6 in Dgcr8 KO mouse ESCs.

A. IF of PML and DDX6 (in-network) and SC-35 (non-target control, not present in the network) in wild-type and Dgcr8 KO ESCs under normal and day2 mTORi conditions. *Dgcr8* KO ESCs were able to downregulate PML and DDX6 but their suppression is inefficient when compared to wild-type ESCs. Scale bar = 10µm.

B. Single-cell quantifications of protein expression levels as determined by measuring mean (area-normalized) fluorescence intensity per cell.

1.9 *Dgcr8* KO cells show altered RNA splicing during dormancy entry

Here I take another example of RNA splicing which according to the miRNA-protein network is predicted to be amongst the top altered pathways in paused ESCs compared to normal. Alternate splicing (AS) is a process that many cells utilize in order to diversify their proteome to accommodate cellular response to changing cellular microenvironments. AS has been linked to mTOR/insulin pathway activity and its infidelity is associated with aging[148].

Since cellular membrane-less RNA processing bodies are perturbed in *Dgcr8* KO cells, I was curious to find out if this perturbation is reflected in the AS process. Indeed, *Dgcr8* KO cells failed to replicate the AS events observed in wild-type cells during dormancy entry **(Figure 40 A)**. Regulators of RNA biosynthesis were particularly affected in *Dgcr8* KO cells **(Figure 40 B)**.

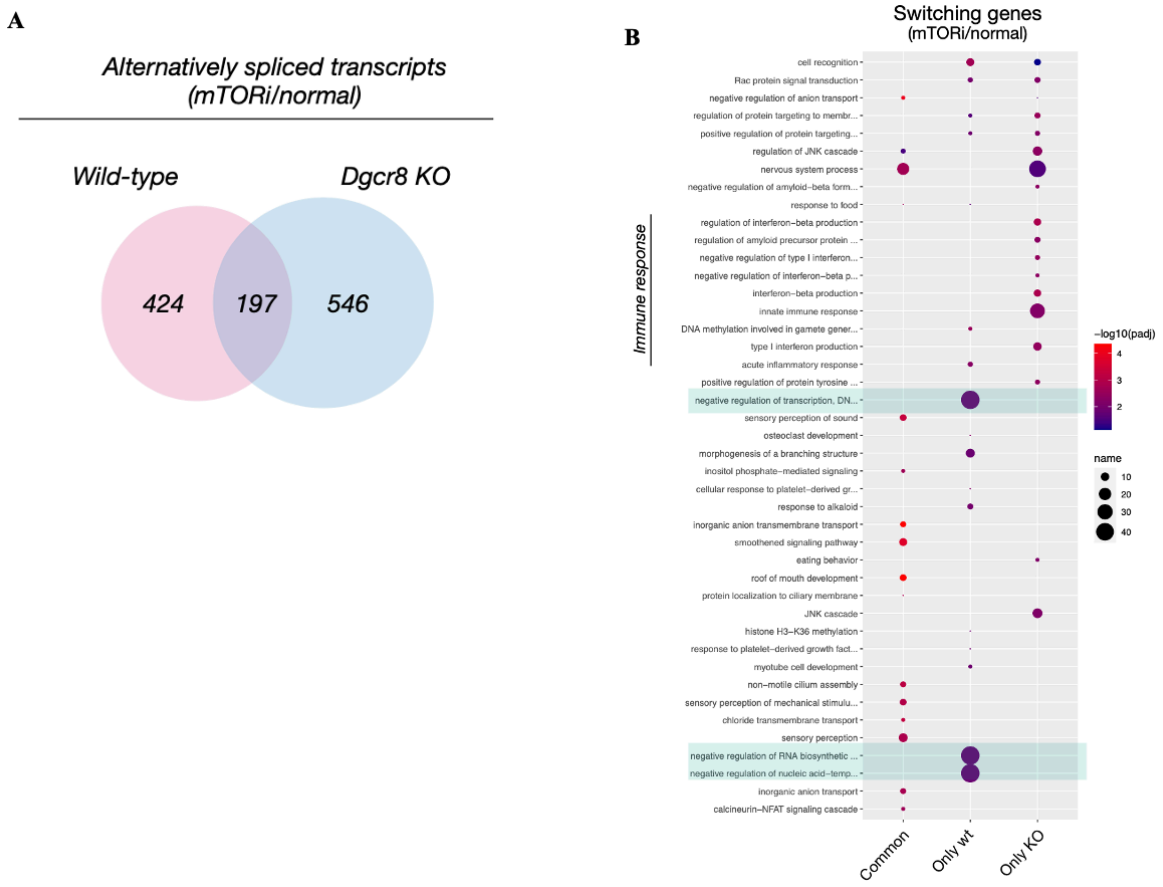

Figure 40. Aberrant RNA splicing in Dgcr8 KO ESCs upon dormancy entry.
A. Venn diagram of alternatively spliced transcript in wild-type and Dgcr8 KO cells under normal and mTORi conditions. Dgcr8 KO cells do not replicate the splicing events of wild-type cells as there is only a small overlap of 197 genes that are commonly spliced.
B. Gene ontology analysis of alternatively spliced genes. Common and genetic background-specific pathways are shown. AS isoforms of negative regulators of transcription and RNA metabolism are enriched only in wild-type cells, whereas *Dgcr8* KO cells show an inflammatory response at this level.

From the AS analysis performed by Francesca, I short-listed genes that showed differential Isoform usage in wild-type and *Dgcr8* KO cells. To confirm this, I performed real-time PCR for isoform detection. The PCR revealed the selected genes showing different AS levels in wild-type and KO cells (MBD2C, UBR2, WIPI2; **(Figure 41 A)** with MDM2 showing the most significant dysregulation for AS in *Dgcr8* KO cells. Since MDM2 showed the most significant dysregulation in isoform usage, I wanted to validate this gene further at the protein level. WB showed that the 32 KDa MBD2C – a short isoform of MBD protein is not expressed in *Dgcr8* KO cells. The overall levels of MBD2 protein are higher in *Dgcr8* KO cells compared to wild-type ESCs **(Figure 41 B and C)**.

The above results show AS events play a role during dormancy transition in mESCs which is controlled upstream by microRNAs and are perturbed in cells devoid of canonical miRNAs as seen in *Dgcr8* KO cells.

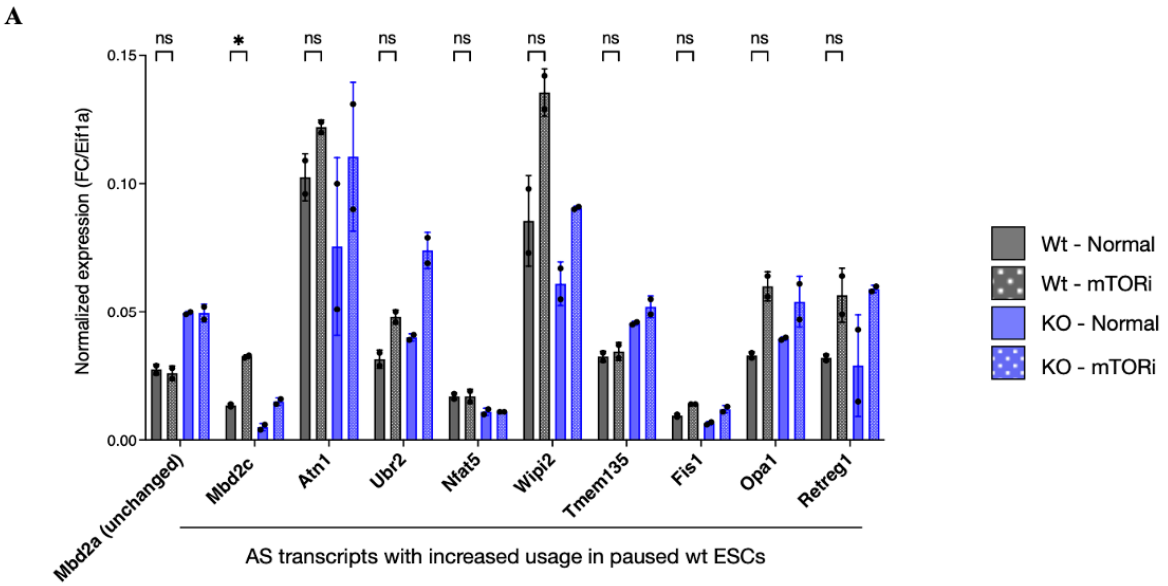

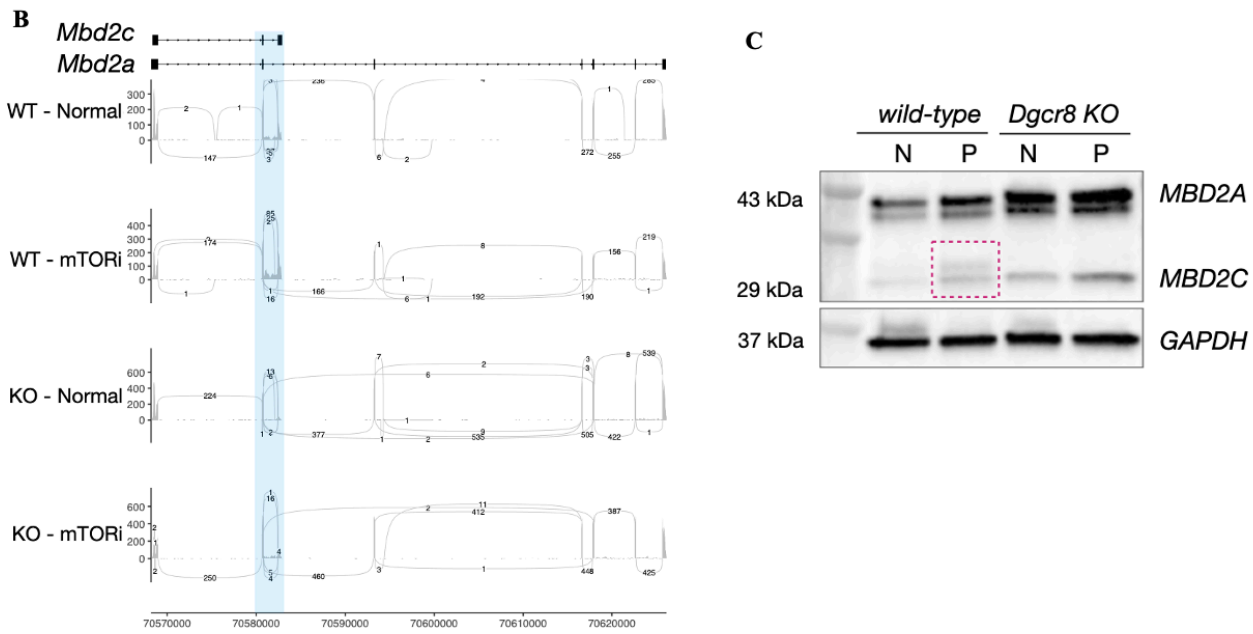

Figure 41. Aberrant RNA splicing in Dgcr8 KO ESCs upon dormancy entry.
A. Validation of the selected isoform was done by isoform-specific qPCR. Isoform showing increased usage in wild-type paused cells (compared to normal) and not in Dgcr8 cells were selected. Primers were designed to specifically amplify the selected isoforms (see methods).
B. Sashimi plots of the AS gene MBD2. Arcs display the number of reads across splice junctions.
C. Western blot for MBD2 shows higher expression of the protein in *Dgcr8* KO ESCs. The *Dgcr8* KO paused ESCs show increased utilization of the shorter isoform of MBD2C. An additional band around 32kDa that may correspond to posttranslational modification of MBD2C is visible in paused wild-type ESCs and not in paused *Dgcr8* KO ESCs.

1.10 The mTOR-TFE3 axis regulates miRNA biogenesis in dormancy

The results so far show the miRNA-mediated fine-tuning of gene expression during diapause entry. The generated microRNA-protein network predicts functional molecular mechanisms that are in play at the time of dormancy showing only selected microRNAs to get upregulated. As a next step, I wanted to know how these dormancy-associated miRNAs are getting upregulated. For this Lambert mined for transcription factor (TF) binding sites on the promoters of 14 concordant upregulated miRNAs. Transcription start sites of miRNAs were retrieved from the FANTOM5 database, and promoters were defined as the region 1,500 bp upstream and 500 bp downstream of the TSS. After the intersection with the clustered miRNAs, the presence of TFBS motifs was predicted within the set of the 14 promoters of the concordant up-regulated miRNAs **(Figure 42)**. Enrichment of a given motif was evaluated by comparing the fraction of promoters with a TFBS for these candidate promoters versus a background set composed of the promoters of all other detected miRNAs (N=91).

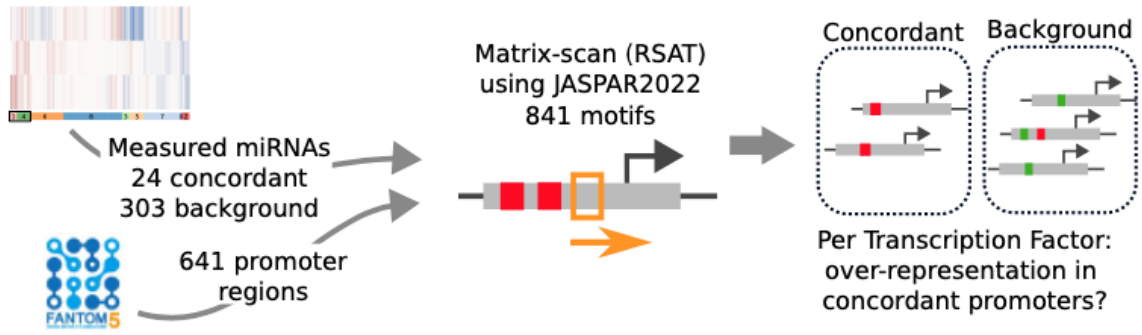

Figure 42. Schematics of TF mining at candidate miRNA promoters.
Transcription start sites of miRNAs were retrieved from the FANTOM5 database and used to scan the [-1,500, +500] regions with JASPAR motifs. High-confidence hits were then used to compare the fractions of promoters with a given motif, for promoters of concordant, positive logFoldChange miRNAs against promoters of other measured miRNAs. from concordant up-regulated miRNAs.

Motifs enriched for 15 TFs were found on the promoters of 14 upregulated miRNAs **(Figure 43)**. The identified TFs belong to important developmental regulators (e.g., HOXD10, ZSCAN4, PAX3) and TFs responsive to external stimuli, such as hormones (e.g., NR2F1, RXRA, PPARD) and nutrient sensing (TFE3). Since mTOR which is a nutrient-sensing pathway gets downregulated during embryonic diapause and is responsible for TFE3 phosphorylation, I decided to focus on TFE3 as a main upstream regulator. I did not consider other developmental TFs since they are either not expressed in ESCs (HOXD10 and PAX3) or expressed in the 2-cell stage (ZSCAN4).

Name	N candidate promoter	Odds Ratio	P-value	Rank
PPARD	8	3.91	0.016	1
POU2F2	7	3.89	0.0208	2
PAX3 (1)	14	5.22	0.024	3
NR2F1	9	3.33	0.0266	4
PAX3 (2)	12	3.42	0.0302	5
HOXD10	9	3.03	0.0385	6
ETV2::DRGX	14	4.38	0.0414	7
ZSCAN4	5	3.69	0.0487	8
LMX1A	12	2.99	0.0493	9
TFE3	**9**	**2.76**	**0.0541**	**10**
ARGFX	14	3.6	0.0701	11
RFX3	3	4.83	0.0712	12
GRHL1	13	2.72	0.0884	13
PRRX2	13	2.72	0.0884	14
HNF4A	5	2.89	0.0947	15
RXRA::VDR	14	3.12	0.0985	16

Figure 43. Enriched TF motifs predicted from JASPAR on the candidate miRNA promoters

TFE3 and the closely related factor TFEB are known to regulate ESC metabolism and lysosomal genes via their TF activity within the nucleus[149]. Intracellular TFE3/TFEB localization dynamically changes in an mTOR-dependent manner. When mTOR is active, TFE3/TFEB is phosphorylated and is sequestered in the cytoplasm, whereas nutrient depletion leads to loss of mTOR-dependent TFE3 phosphorylation and its translocation into the nucleus[150] **(Figure 44 A)**. Based on this literature evidence, I hypothesized that TFE3 nuclear migration and its occupancy on the miRNA promoters drive the transcription of the dormancy-

associated miRNAs. Thus, providing the missing link between mTOR activity and miRNA upregulation.

To validate the hypothesis, I first performed an IF for TFE3 in normal and paused wild-type mESCs. This is to check for its localization in these two conditions. Pausing via mTORi increased the levels of TFE3 both in the nucleus and in the cytoplasm **(Figure 44 B)**.

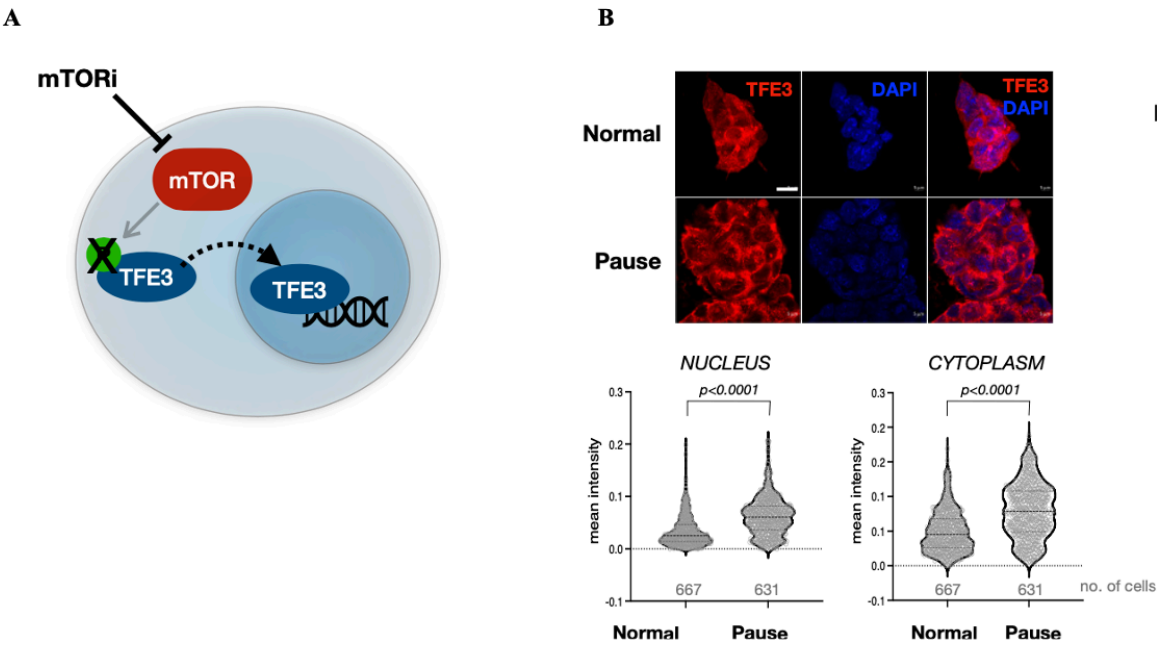

Figure 44. mTOR-TFE3 axis regulates miRNA biogenesis in dormancy.
A. Graphical representation of TFE3 regulation by mTOR. When mTOR is active, it phosphorylates TFE3 and sequesters it in the cytoplasm. When mTOR is not active, unphosphorylated TFE3 translocates into the nucleus and regulates its target genes.
B. IF of TFE3 in wild-type ESCs in normal and paused conditions. Lower panel shows single-cell quantification of mean fluorescent intensity (area normalized) in the nucleus and cytoplasm. Scale bar = 10µm. Statistical test is Kolmogorov-Smirnov test, two-sided.

Next, to validate TFE3 occupancy on the promoters of upregulated miRNAs, my colleague Chieh-Yu Cheng performed CUT&Tag. This method was chosen over ChIP owing to its better resolution, low background signal and low cell numbers. TFE3 is indeed bound to the promoters of dormancy miRNAs in paused cells at higher levels compared to normal ESCs and compared to control miRNAs **(Figure 45 A)**. miR-200a/b, which we functionally validated in previous experiments, were among the top TFE3 targets **(Figure 45 B)**.

In the first part of my thesis, I identified an mTOR-TFE3-miRNA axis, which regulates the rewiring of miRNA expression and downstream protein levels in the transition of mouse pluripotent cells from proliferation to dormancy.

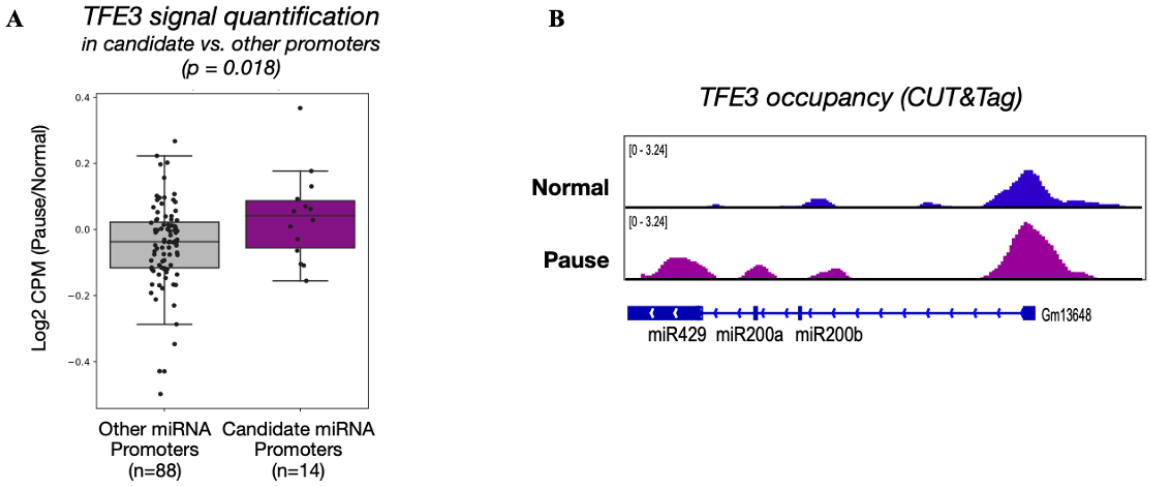

Figure 45. TFE3 binds to the promoters of candidate miRNAs and regulates their biogenesis during dormancy.

A. Comparison of the log2 ratio of TFE3 levels (maximum scaled CPM) at candidate (n=14) and control (n=88) miRNA promoters. Statistical test is Mann-Whitney U-test, one-sided.

B. Genome browser view of TFE3 occupancy over the Gm13648 gene which contains the miR-200a, miR-200b, and miR-429 miRNAs. TFE3 occupancy was mapped via CUT&Tag in wild-type normal and paused ESCs.

Part 2: Exploring the hypothesis of whether human PSCs and blastoids regulate their timing of development via the mTOR pathway.

In the first part of my thesis, I show how microRNAs are indispensable for mouse embryos to undergo diapause upon mTORi. The question still remains whether diapause can be replicated in humans and whether the process is conserved as shown in the mouse ESCs and embryos. Although this question has been raised in the past, a convincing case of functional and molecular reversibility of diapause with intact morphology has never been shown yet. To answer this question, I needed to know the pattern of mTOR activity in mouse and human.

2.1 mTOR pathway activity is similar in mouse and human embryo

It is known that the mTOR activity governs the proliferative and dormancy decisions of a stem cell. To know if mouse and human embryos share a similar pattern of mTOR activity, our collaborators from Kathy Niakan's lab performed immunofluorescence (IF) staining for phospho-S6 (pS6) a downstream mTOR target **(Figure 46 A and B)**. In both mouse and human embryos, we see that the polar trophectoderm (TE) shows a higher pS6 staining compared to mural TE and ICM. The mural TE in both species shows a salt and pepper pattern of staining of pS6. This is also true for another mTOR target phospho-AKT (pAKT) **(Figure 46 C)**. This expression pattern does not reflect on protein synthesis but on the mTOR activity itself **(Figure 46 D)**. This shows that mTOR is active in pluripotent cells although at lower levels when compared to TE.

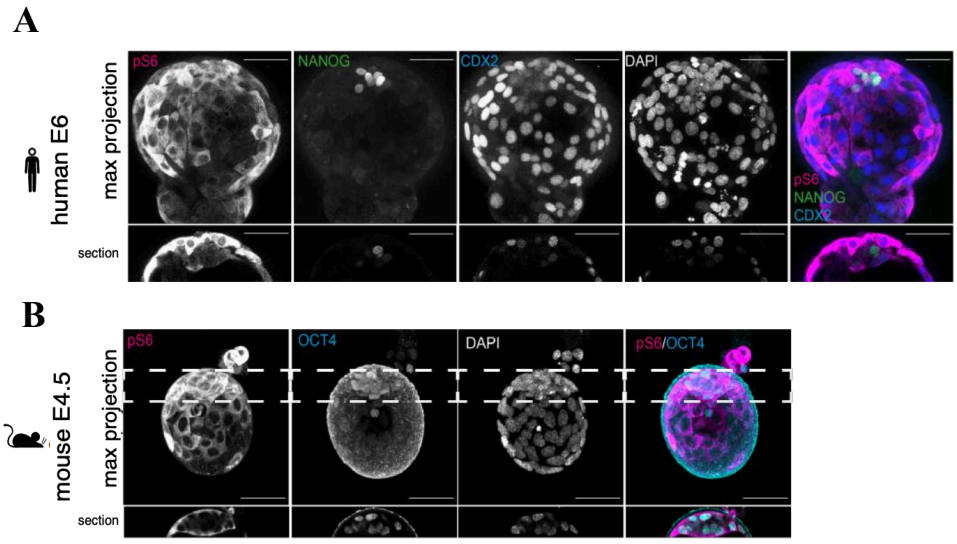

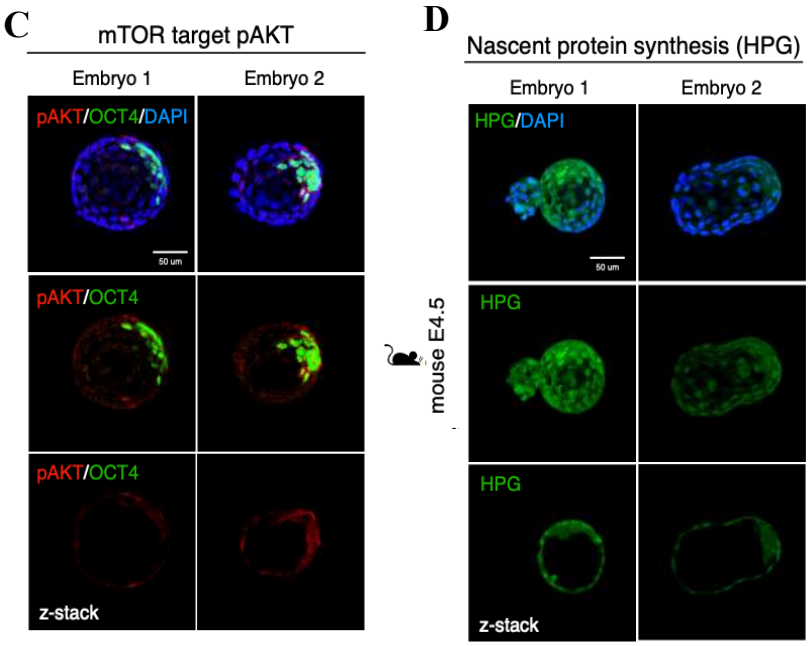

Figure 46: mTOR is sensed in a similar pattern in mouse and human blastocysts.
A. Immunofluorescence staining of E6 human blastocyst for mTOR downstream target pS6, epiblast marker NANOG and trophectoderm marker CDX2. Scale bar = 50µm.
B. Immunofluorescence staining of E4.5 mouse blastocyst for mTOR downstream target pS6, epiblast marker OCT4. Mouse and human blastocyst show similar patterns of pS6 staining Scale bar = 50µm. **C and D.** Immunofluorescence staining of another mTOR target pAKT and nascent protein synthesis in E4.5 mouse blastocyst. An amino acid analog HPG was used to track nascent protein synthesis. Both staining showed heterogeneity in pathway activity between ICM and TE and within TE. Scale bar = 50µm.

mTOR pathway is a nutrient-sensing pathway that regulates the growth and proliferation of cells based on the availability of nutrients. From the literature, it is known that insulin growth factor (IGF) is a direct upstream regulator of the mTOR pathway and has been implicated in diapause regulation in other species[151,152]. IGF1 is expressed from the maternal tissue, in an estrogen-dependent manner, for paracrine regulation of the embryo[153]. The embryo expresses IGF2 for autocrine regulation. pS6 and pAKT levels are altered in uterine fibroids in response to IGF1 but not IGF2[154]. Thus, showing the sensitivity of mTOR to IGF1.

To test the mTOR activity is similarly sensitive to IGF1 signaling in both species we subjected mouse and human embryos (either day 2 or day 5, based on embryo availability) to IGF1 treatment. Two concentrations of IGF1 were used – 17nM an estimated concentration in the human reproductive tract[155]and 1.7nM. IGF1 supplementation increased human blastocyst formation rate at 1.7 nM (58% in 1.7 nM IGF1 vs. 27% control media) **(Figure 47 A)**, consistent with previous findings[155].

Importantly, 1.7 nM IGF1 specifically benefitted the ICM in both human and mouse blastocysts by increasing the number of cells **(Figure 47 B and C)**. Higher IGF1 concentration did not

enhance this trend, which could be explained by the increase and plateau of pS6 at 1.7 nM IGF1 in the human ICM **(Figure 47 D)**.

The above data suggest that the mTOR pathway is active and tightly regulated in human blastocysts in a manner that is highly similar to the mouse, supporting the possibility that mTOR inhibition may induce a diapause-like dormant state in human embryos.

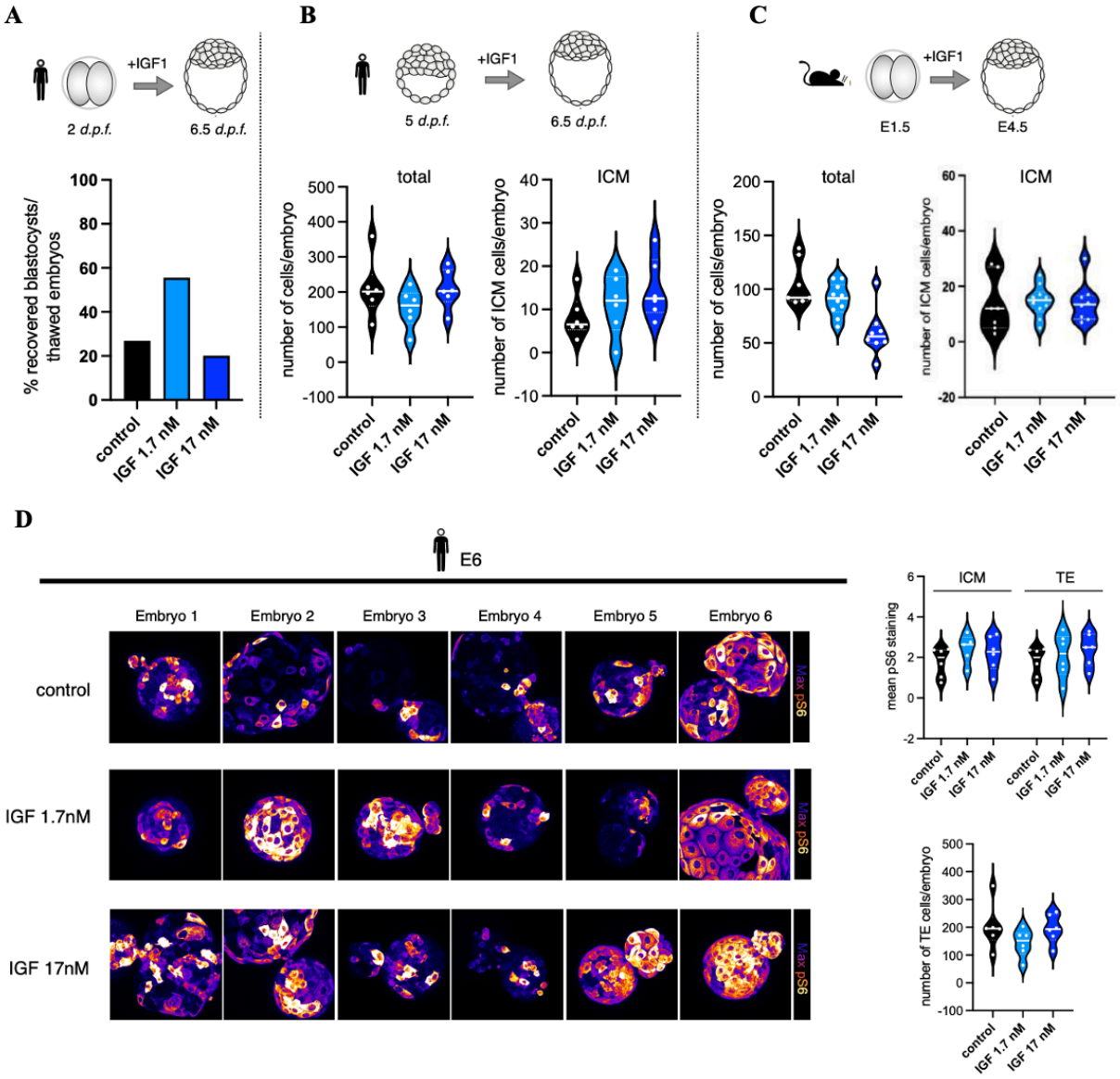

Figure 47. IGF supplementation on blastocyst formation rate and mTOR activity.
A. Human 2-cell embryos when cultured in 1.7nM IGF yielded a significantly higher percentage of blastocysts when compared to control embryos. n = 14 and 18 embryos were used for 1.7nM and 17nM treatments, respectively. As control, data from all thawed blastocysts in the assay year were collected, n = 137.
B. IGF treatment increases the number of cells in the ICM of human blastocysts. n = 6 embryos were used.
C. Mouse blastocyst, also showed an increase in ICM cell number when treated with IGF.
n = 6, 10, 8 for control, 1.7nM and 17nM respectively.
D. Human blastocysts show maximum pS6 intensity at 1.7nM IGF treatment and get saturated at a higher concentration of 17nM. Right panels show the quantification of pS6 intensities and number of TE cells in each condition.

2.2 Human PSCs show varying efficiency in undergoing diapause via mTOR inhibition.

Both human and mouse preimplantation development show the mTOR pathway to be active and show similar patterns of activity, I was curious to know whether human PSCs just like the mouse ESCs, have the capacity to undergo diapause via mTOR inhibition.
Human PSCs can be captured in various spectra of pluripotency which is reflective of early and post-implantation development **(see Figure 8 – in the introduction)**. Although it is known that diapause in most mammals occurs before implantation and naïve human PSCs may be more amenable to be put in a diapause-like state, I wanted to test in an unbiased manner, the capacity of different human PSCs cultured in naïve (PXGL), naïve-like (RSeT) and primed (mTeSR) to diapause via mTORi (see methods for cell-line and culture conditions and optimization). I used mouse ESCs grown in serum/LIF conditions under mTORi as a control as they are known to undergo diapause efficiently and homogeneously. I used INK-128 – an mTOR catalytic inhibitor to induce diapause in both mouse and human PSCs[114].

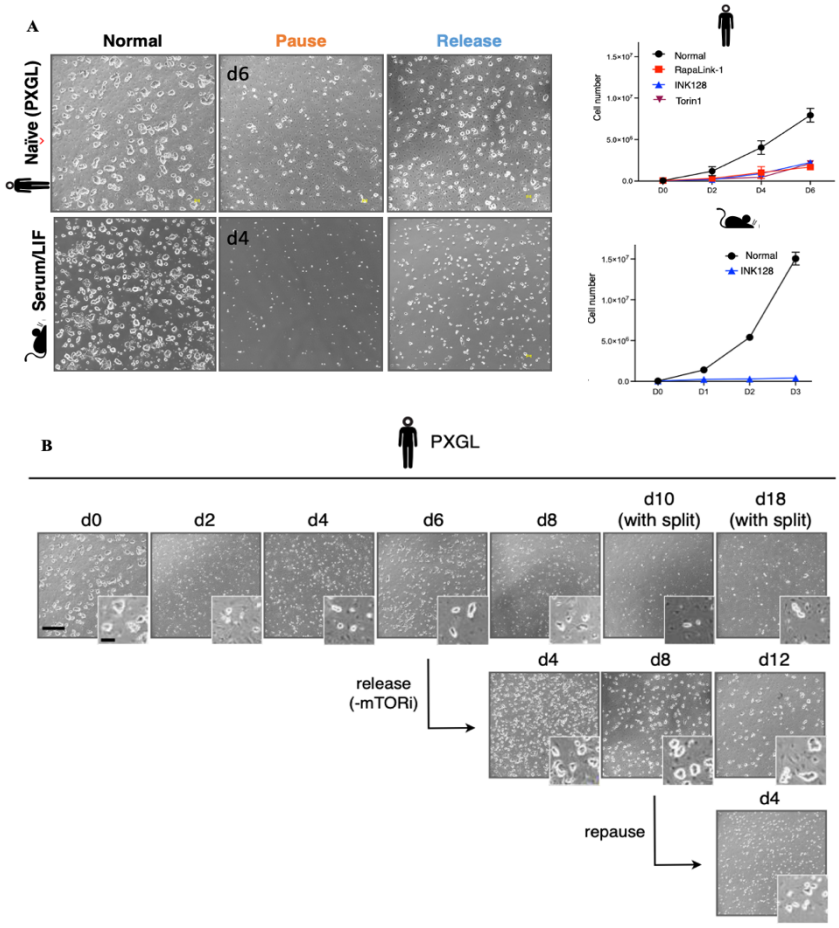

Figure 48. Human naïve (PXGL) cells reversibly pause like mouse ESCs.

A. Representative bright field images of human naïve ESCs before, during and after mTORi treatment as compared to the mouse. Scale bar = 500µm. Right panel shows the proliferation curves of human naïve ESCs treated with mTOR inhibitors Rapalink-1, INK128 and Torin1. Proliferation of mouse ESCs cultured in INK128 is shown in comparison.

B. Bright field images of pause, release and re-pause human ESCs in PXGL culture. Cells need to be split during prolonged pausing to overcome MEF depletion and differentiation. Scale bars: main - 500µm, inset - 100µm.

Human naïve cells cultured in PXGL (from now on PXGL cells) just like the mouse ESCs were able to reduce proliferation which was reversible and maintained a dome-shaped colony morphology with shiny borders **(Figure 48 A)**. PXGL cells could be maintained for a maximum testing period of 18 days under mTORi which could be released and iteratively re-paused without compromising on colony morphology **(Figure 48 B)**. PXGL cells paused with other mTOR inhibitors Rapalink-1 (new generation inhibitor with a mode of action similar to INK128) and Torin1 (non-rapalog inhibitor which is more selective for mTOR) exactly reproduced the same slow proliferation as seen with INK128 **(Figure 48 A)**. Reduction of proliferation by Torin-1 was in a dose-dependent manner **(Figure 49 A and B)**.

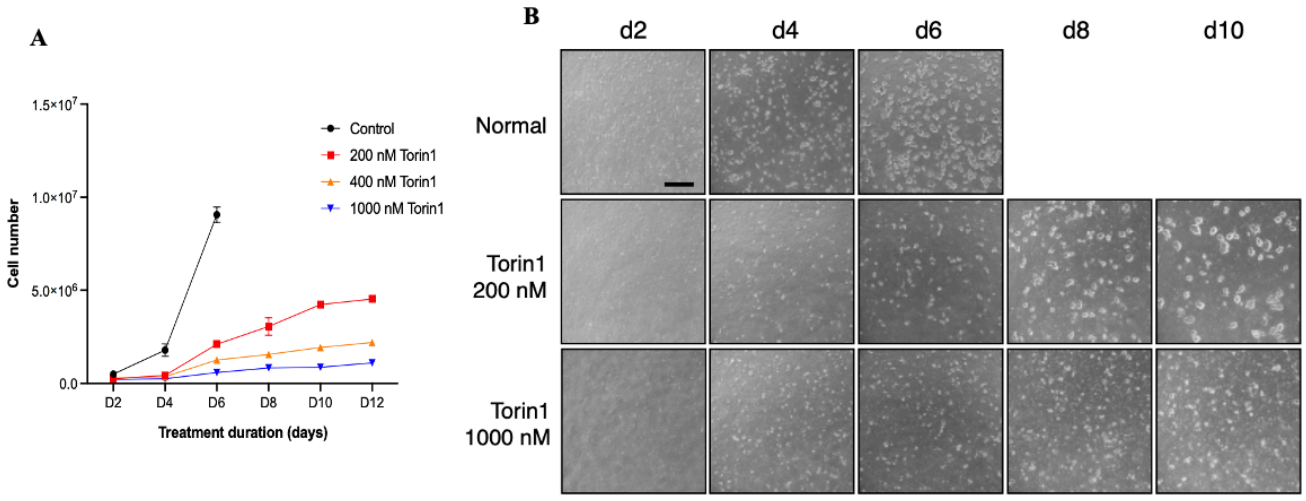

Figure 49. Dose-dependent pausing of human naïve ESCs by Torin1.

A. Proliferation curve of human ESCs when treated with catalytic inhibitor Torin1. Cells were treated with 200, 400, and 1000nM of Torin1 over a period of 12 days without split and cell numbers were counted. Control cells were terminated on day 6, as the culture became overconfluent after this period.

B. Brightfield images of Torin1 treated human ESCs over the treatment time course.

Scale bar = 500µm.

Human naïve-like iPSCs grown in RSeT (from now on RSeT cells) were also able to enter into a diapause-like state but with lower efficiency **(Figure 50 A)**. The population of cells that were able to undergo diapause using INK128 (see methods for pausing culture optimization) showed domed-shaped highly compact colony morphology with shiny borders with almost no proliferation. These cells reverted back to normal proliferation and morphology when released from mTORi **(Figure 50 A)**. This suggests that mTORi treatment does not have an irreversible

impact on cell growth and proliferation. Unlike the PXGL cells which responded homogenously to mTORi showing an initial increase in apoptosis which stabilized over time, RSeT cells persistently showed a high apoptotic rate under mTORi **(Figure 50 B)**.

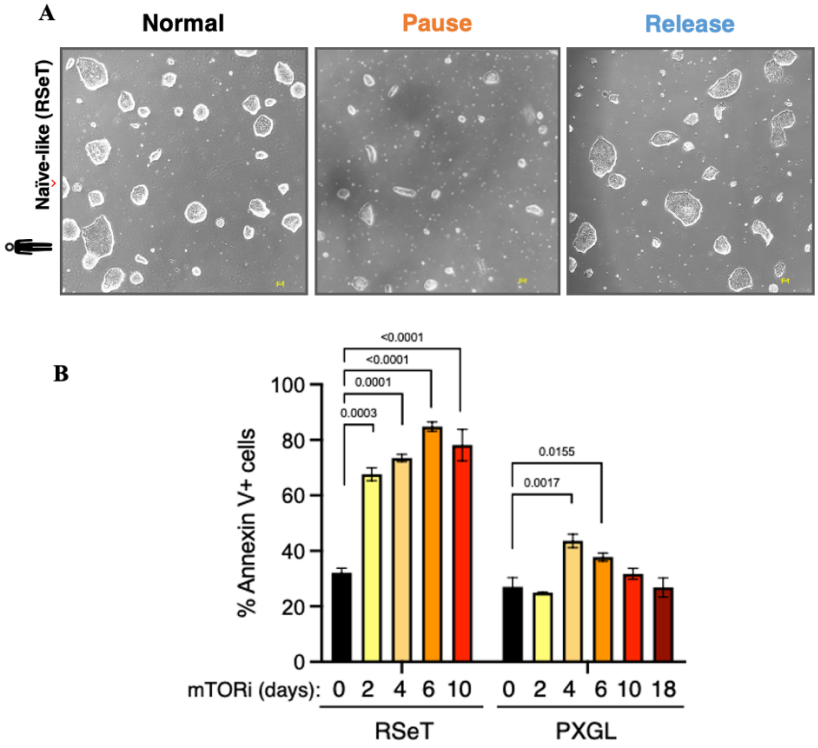

Figure 50. Human naïve-like cells (RSeT) reversibly pause upon mTOR inhibition with lesser efficiency compared to PXGL cells.

A. Representative bright field images of human naïve ESCs before, during and after mTORi treatment. Scale bar = 500µm.

B. Percentage of Annexin V positive cells during the course of mTORi treatment in RSeT and PXGL culture.

Since RSeT cells showed a high rate of apoptosis, I was curious to know whether the subset of cells undergoing dormancy was pluripotent. For this in collaboration with Maria (Epo GmbH, Berlin) we performed a teratoma assay to check the ability of these cells to give rise to 3 germ layers. Since paused RSeT cells did not proliferate, I used pause-release cells which were injected into immunodeficient mice. Normal proliferative RSeT cells were used for the control experiment. Tumour growth was measured over time **(figure 51 A)**. Pause-release cells formed teratomas within 35 days which is faster than normal cells which formed teratomas within 50-70 days **(Figure 51 B)**. The body weight of the mice was similar throughout the experiment. Like the normal cells, the pause-release cells were able to give rise to all three germ layers but with lower efficiency **(Figure 51 B)**. The results show that paused RSeT cells are pluripotent and maintain their differentiation capacity during mTORi-mediated dormancy.

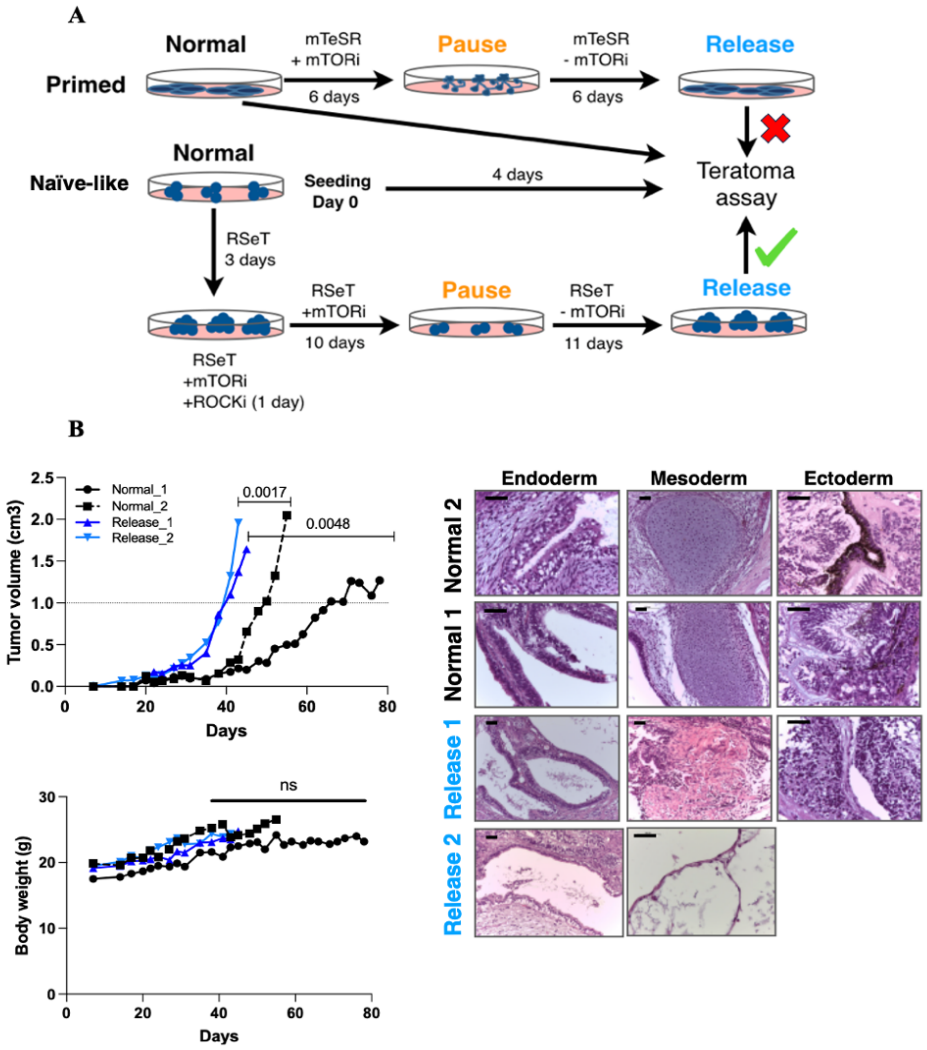

Figure 51. Naïve-like (RSeT) cells maintain their differentiation potential during mTORi-mediated pausing.

A. Schematic workflow of human PSCs developmental pausing. Note that human pluripotent stem cells require a longer treatment compared to mouse to establish and stabilize pausing.

B. Left panel: Quantifications of teratoma tumor volume in each injected animal. Mice were sacrificed when teratomas reached 2 cm^3 in volume. Naïve-like pause-release cells formed teratomas approximately two weeks earlier than normal PSCs. Statistical test performed is a non-parametric Friedman's test with Dunn's multiple testing correction. Graph showing body weight of mice during the course of teratoma assay.

Right panel: H&E staining of formed teratomas showing the generation of all three germ layers from pause-released naïve-like cells. Two mice were injected per cell line. None of the primed hPSCs generated teratomas under these conditions and were excluded from follow-up experiments. Scale bars, 50 µm.

Just like in the mouse ESCs, pausing of RSeT cells upregulated dormancy-associated microRNA miR-92 **(Figure 52)**. Showing a possible prominent and conserved role of miR-92 in regulating dormancy even in human PSCs.

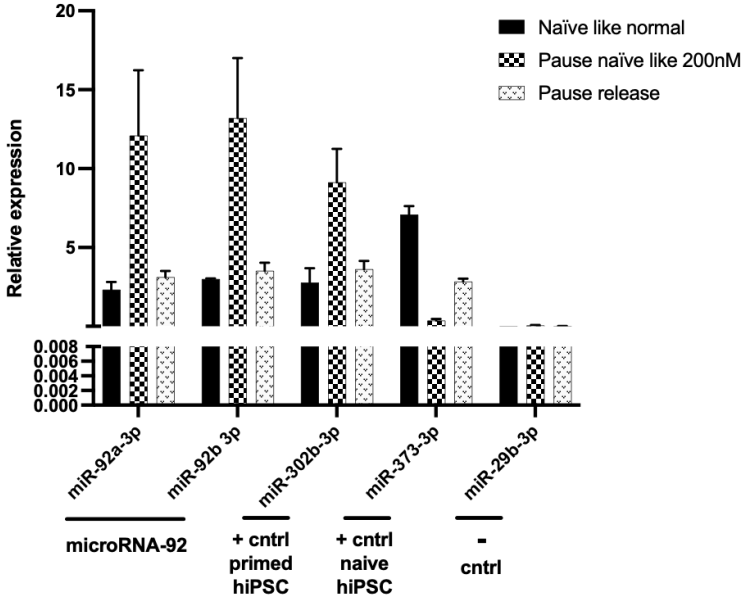

Figure 52. Pausing of RSeT cells upregulates miR-92 expression.
qPCR showing upregulation of miR-92 during pausing of RSeT cells. Upon release from pausing miR-92 levels revert back to normal levels. miR-302b-3p and miR-372-3p are miRNA markers for primed and naïve hPSCs respectively. miR-29b-3p is not expressed in hPSCs, hence used as a negative control. Relative expression is calculated against the housekeeping gene eIF1 alpha.

In contrast to naïve (PXGL) and naïve-like PSCs (RSeT), when I cultured primed hPSCs (from now on mTeSR cells) with the same concentration of 200nM INK128 they were unable to survive and died within 4 days of treatment. When I treated the same mTeSR cells with a lower concentration of 100nM INK128, the cells were able to survive albeit with altered morphology **(Figure 53)**. The mTORi-treated mTeSR cells assumed a network-like growth rather than growing as distinct individual dome-shaped colonies **(Figure 53 inset)**. This network-like growth had flattened cells with small interspersed cavities which persisted over time. Upon release from mTORi, mTeSR cells restored their original proliferative capacity and colony morphology.

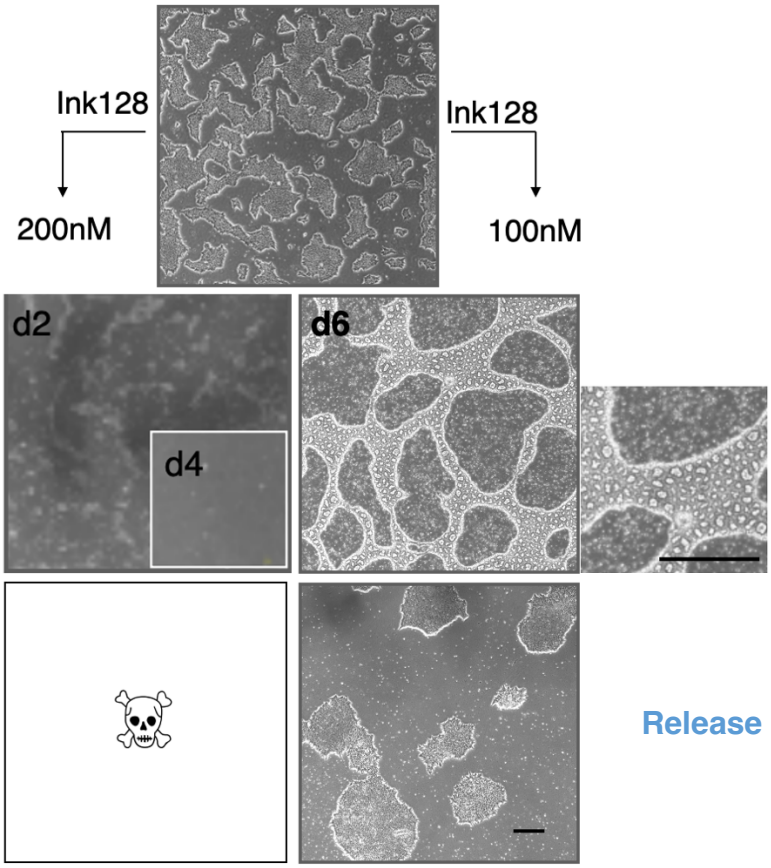

Figure 53. Human-primed mTeSR cells respond differently to mTOR inhibition.
Representative bright field images of human naïve ESCs before, during and after mTOR inhibition under indicated conditions. In 100nM mTORi condition, primed cells form flat network-like colonies having gaps between them. Scale bar = 500µm.

Just like the RSeT cells, mTeSR cells when treated with mTORi upregulated miR-92, showing its conserved role in transitioning the primed hPSCs into dormancy **(Figure 54 left)**.

With the altered cellular morphology observed in mTeSR cells upon mTORi, I wanted to know whether these cells retained their primed pluripotent markers. Real-time PCR data showed that although they undergo cell flattening, these cells retained the expression of primed pluripotent marks **(Figure 53 right)**.

Although the above results show primed hPSC's unique pause response to mTORi at lower concentrations, these cells failed the teratoma test. The primed pause-release cells were unable to give rise to tumors in immunocompromised mice. Thus, these cells were not considered further for the study.

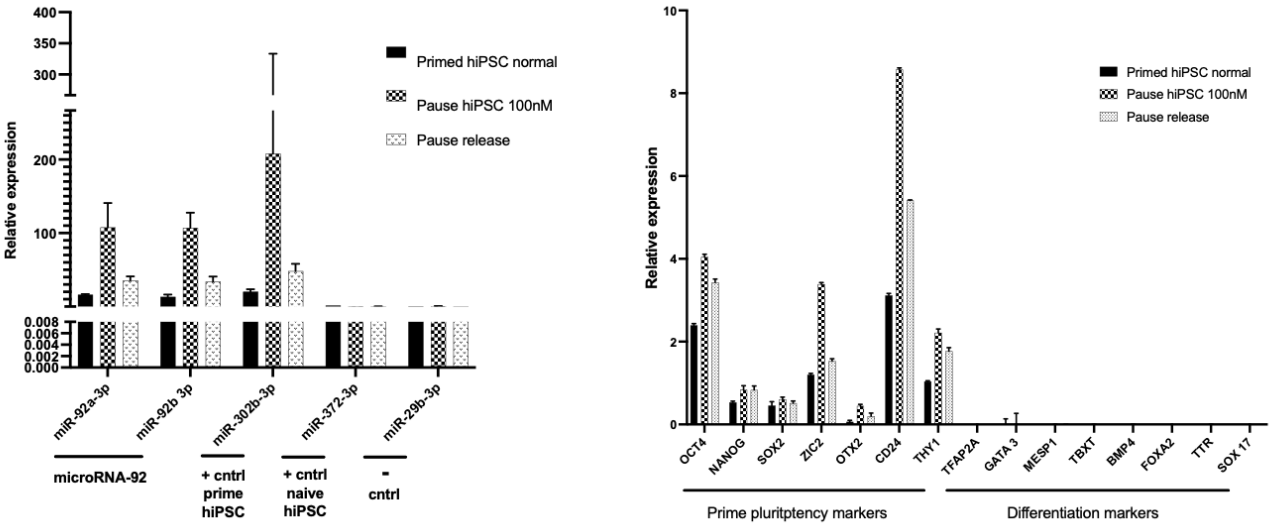

Figure 54. Pausing of human primed mTeSR cells.
Left: qPCR showing upregulation of miR-92 during pausing of mTeSR cells. Upon release from pausing miR-92 levels revert back to normal levels. miR-302b-3p and miR-372-3p are miRNA markers for primed and naïve hPSCs respectively. miR-29b-3p is not expressed in hPSCs, hence used as a negative control. Relative expression is calculated against the housekeeping gene eIF1 alpha.
Right: Expression of prime pluripotency marks during pausing of mTeSR cells. Relative expression is calculated against the housekeeping gene eIF1 alpha.

2.3 RSeT cells undergo deeper dormancy compared to PXGL cells

Since the efficiency of pausing was markedly different between naïve (PXGL cells) and naïve-like (RSeT cells), I wanted to investigate the position these cells occupy in the cell cycle. For this, I performed a 5-Ethynyl-2'-deoxyuridine (EdU) incorporation assay simultaneously on normal or paused PXGL and RSeT cells. The method employs the incorporation of thymidine analog EdU into a newly synthesized DNA strand to measure the proliferation in a given cell system. The detection of EdU is based on click chemical reaction which utilizes a fluorescent azide group that binds to the alkyne moiety in the EdU catalyzed by copper to give a fluorescent signal.
Similar to mouse ESCs, PXGL cells continued to progress through the cell cycle **(Figure 55 A)**. These cells had a slight increase in G0/G1 and G2/M stages and a corresponding decrease in S phase. The reduced EdU incorporation in these cells points to a slow rate of proliferation during mTORi pausing **(Figure 55B left)**. Treatment of PXGL cells with the mTOR catalytic inhibitors INK128 and RapaLink-1 resulted in similar cell cycle distributions **(Figure 55 A)**. The data shows the effect of mTORi on the growth of PXGL cells which is reflected in the extended cell cycle where G0/G1 and G2/M phases prolong proportionately more than the S phase compared to normal cells. In contrast to PXGL cells, RSeT cells showed complete cell cycle arrest in the G0/G1 phase, with only a fraction of cells in the S phase showing low EdU incorporation and no cells in the G2/M phase **(Figure 55 B)**.

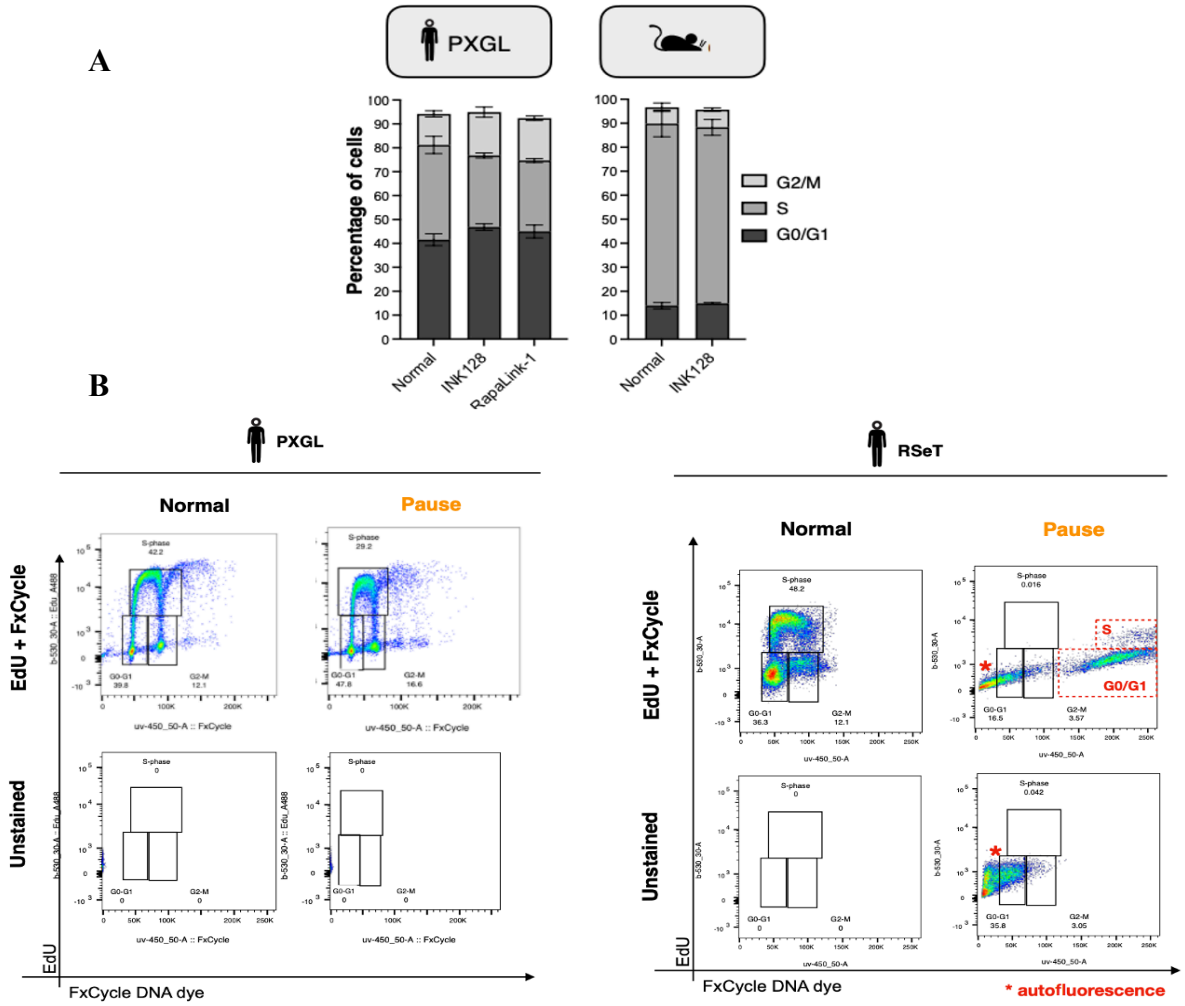

Figure 55. RSeT cells are more quiescent than PXGL cells.
A. Cell cycle distribution of mTORi-treated PXGL and mouse ESCs as determined by EdU incorporation. PXGL cells like the mouse ESCs have a slight increase G0/G1 and G2/M stages. Showing a slow rate of proliferation.
B. Flow cytometry data comparing cycle profiles of PXGL and RSeT cells. RSeT cells show greater quiescence to mTOR inhibition with the majority of cells in G0/G1 stage.

I also performed immunofluorescence (IF) for the mitotic marker H3phospoS10. IF showed complete loss of the marker in paused RSeT cells compared to PXGL cells which stained for fewer marks under mTORi. Upon release from mTORi, both the cell types reverted back to normal proliferation with an increase in cell number staining for the mitotic marker **(Figure 56)**.

The above results show that under mTORi, RSeT cells undergo deeper dormancy with no cell proliferation in contrast to PXGL cells which continue to proliferate and move through the cell cycle slowly. Importantly, pausing in both the cell types is functionally reversible with the recovery of the mitotic cells after release from mTORi.

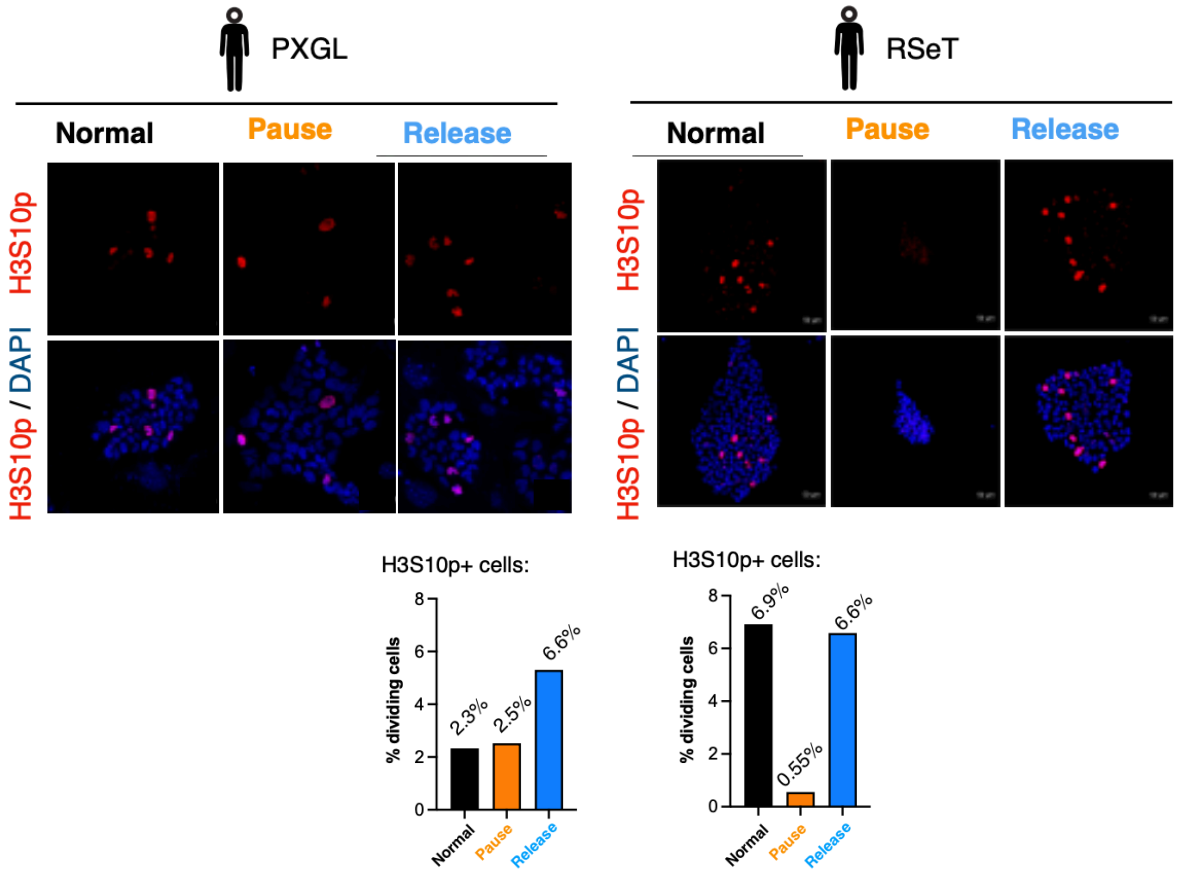

Figure 56. Reversal of proliferation in PXGL and RSeT cells after mTORi release.
Levels of cell division marker H3pS10 in normal, d6 pause and released human cells in PXGL and RSeT culture. The panel below shows single-cell quantifications. n = number of cells analyzed. Statistical test performed is one-way ANOVA with Tukey's multiple testing correction. Scale bar = 50µm.

2.4 Pluripotency and genome integrity is maintained in paused hPSCs

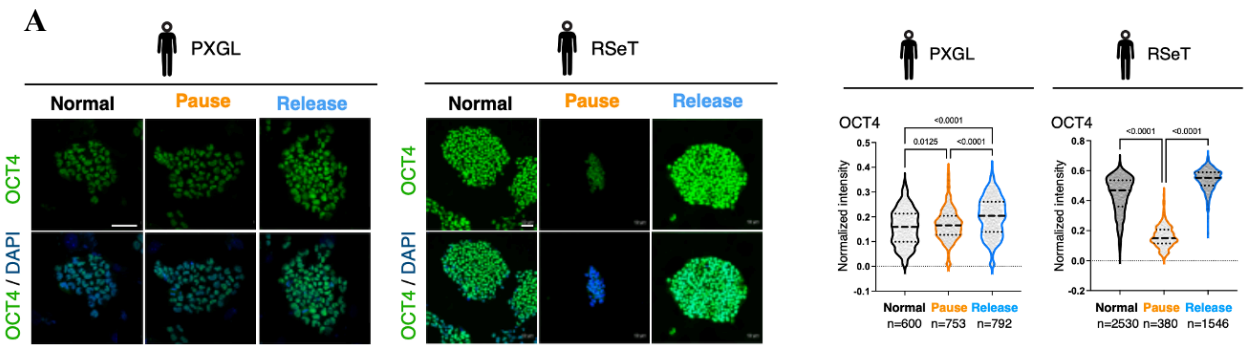

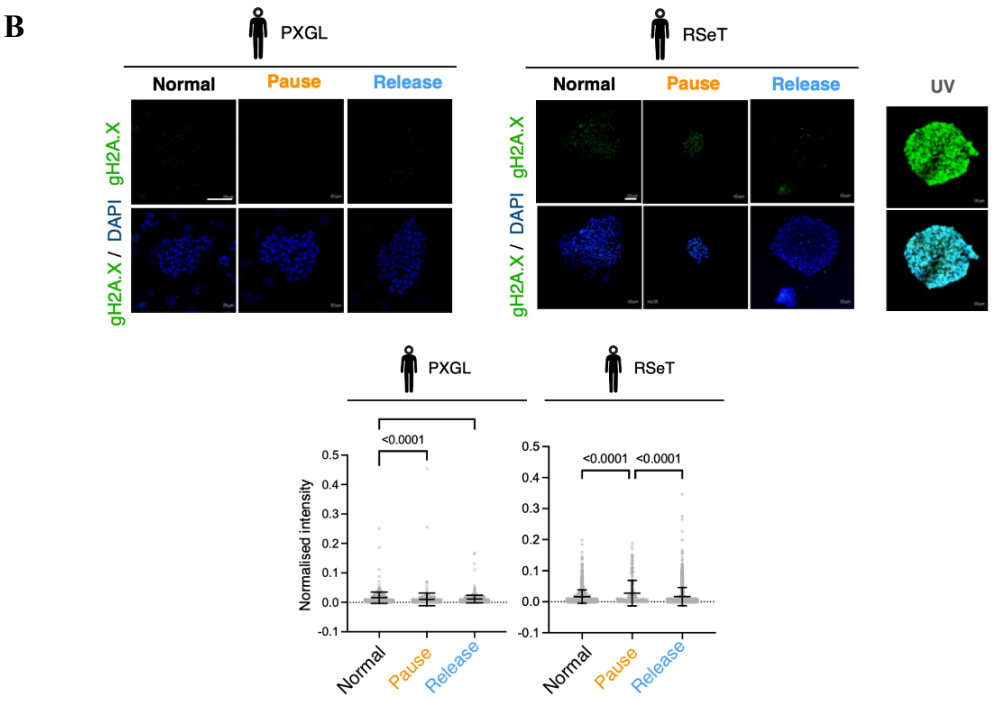

Figure 57. Dormancy preserves pluripotency and genome integrity in both PXGL and RSeT cells.

A. Levels of pluripotency marker OCT4 in normal, d6 pause and released human cells in PXGL and RSeT culture. The panel to the right shows single-cell quantifications. n = number of cells analyzed. Statistical test performed is one-way ANOVA with Tukey's multiple testing correction. Scale bar = 50µm.

B. Levels of DNA damage marker γH2A.X in the corresponding conditions. As positive control, cells were irradiated with UV at 4000µJ/sq cm for 10 seconds and fixed 6 hours later. Paused or released PXGL or RSeT cells do not show an increase in DNA damage. The panel below shows single-cell quantification of γH2A.X intensities normalized to the cellular area.

n = number of cells analyzed. Statistical test performed is one-way ANOVA with Tukey's multiple testing correction. Scale bar = 50µm.

From the teratoma assay, I tested the developmental potential of pause release cells in forming the three germ layers, I wanted to next investigate if there is any compromise of pluripotency and genome integrity at the time of pausing in both PXGL and RSeT cells. For this, I performed IF for OCT4 – a pluripotency marker and γH2A.X – a DNA damage marker that is first recruited at the site of damage **(Figure 57 A and B)** on normal, pause and pause release cells. I found that the expression of OCT4 did not change for paused PXGL cells when compared to control cells grown in normal culture conditions. **(Figure 57 A)**. Whereas the expression of OCT4 was greatly reduced in paused RSeT cells compared to normal. This might be due to the deeper dormancy experienced by RSeT cells, where the whole genome may be experiencing hypo-transcription and translation **(Figure 57 A)**. In both cell types after mTORi release expression of OCT4 was higher than the control normal cells which is indicative of hyper-transcription and translation after sustained genomic repression. Neither PXGL nor RSeT cells showed increased genomic recruitment of γH2A.X in pause or release conditions **(Figure 57 B)**. Thus, showing that the genome is not compromised under any of these conditions.

The above results show that cellular identity is preserved after mTORi-mediated pausing of hPSCs and these cells retain their developmental potential during the period of dormancy.

2.5 Pausing of hPSCs is mediated by mTOR

Earlier results show the involvement of the mTOR pathway in controlling the proliferative Vs dormancy decision of naïve hPSCs (PXGL) via pharmacological inhibition of mTOR. To further corroborate the involvement of mTOR, I aimed at genetically targeting Raptor and Rictor which are components of TORC1 and TORC2 respectively. Since I was unsuccessful in generating a stable shRNA knockdown for Raptor and Rictor, I decided to use siRNAs to target the above two proteins. PXGL cells were transfected with control siRNA and siRNA against Raptor and Rictor. After transfection the cells were allowed to grow for 3 days, after which the cells were plated for proliferation assay, immunofluorescence (IF) and western blot (WB) **(Figure 58)**.

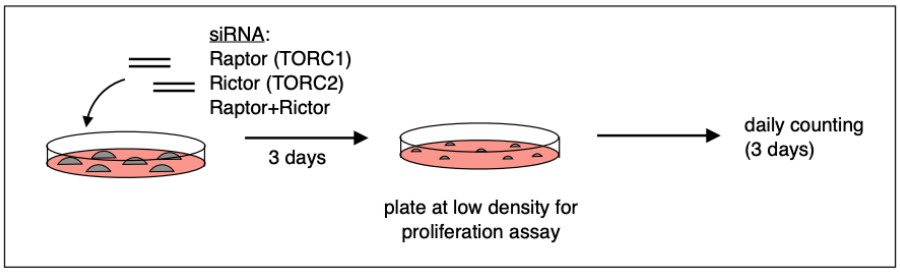

Figure 58. Schematic of siRNA-mediated knockdown of Raptor and Rictor.
Medium-density PXGL cell cultures were transfected with Raptor, Rictor siRNA, or both and grown for 3 days. After that cells were split and plated at low density for proliferation assay.

Knockdown of Raptor and Rictor were confirmed by WB **(Figure 59 A)**. IF for downstream mTOR targets after siRNA transfection showed decreased expression of phospo S6 (pS6) with Raptor siRNA, with its complete loss of expression in Raptor/Rictor combined knockdown. pAKT showed decreased expression with Rictor only and Rictor/Raptor combined knockdowns **(Figure 56 B and C)**. The above results provide experimental proof of the effectiveness of the siRNAs in bringing down the expression of mTOR target proteins and in turn, genetically reducing the overall mTOR activity.

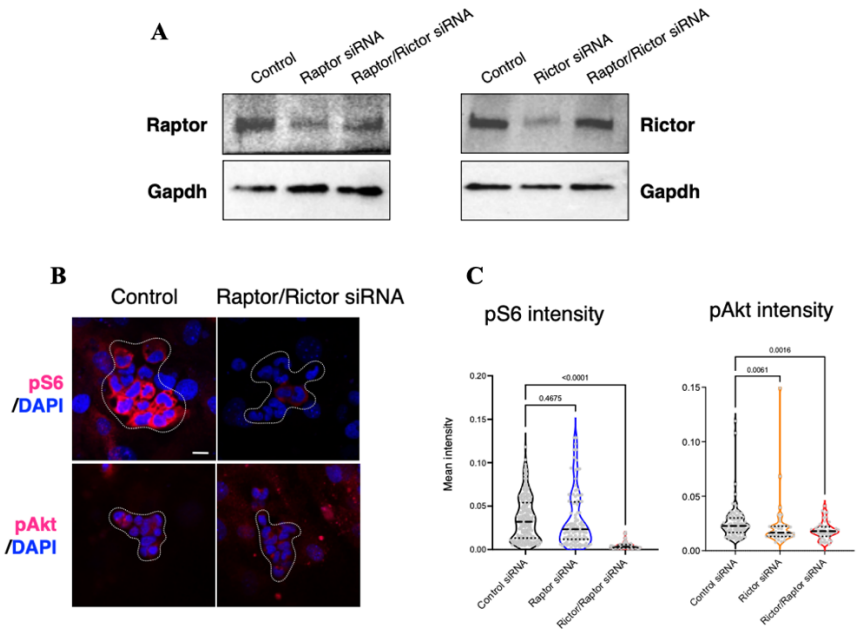

Figure 59. Genetic knockdown of mTOR. A. Western blot showing knockdown of Raptor and Rictor 48 hours after transfection. **B and C.** IF showing levels of TORC1/2 targets pS6 and pAKT 48 hours after transfection. Scale bars = 20µm.

siRNA-mediated transient knockdown of Raptor and Rictor reduced the proliferation of hESCs, which was further reduced by Raptor/Rictor combined knockdowns **(Figure 60 left)** while retaining the colony morphology during the process. The maximum reduction in proliferation was seen on day 2 **(Figure 60 right)**. After day 2 the Rictor-only knockdown cells reverted back to normal proliferation while the Raptor-only and Raptor/Rictor combined knockdown continued to proliferate slowly even at day 3. The above genetic perturbation shows the central role played by mTOR in bringing paused pluripotency in hPSCs.

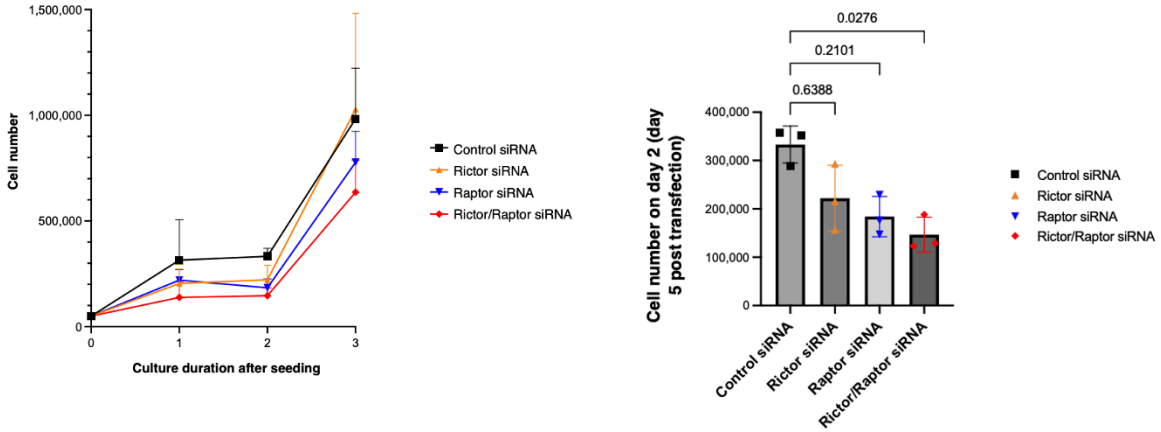

Figure 60. Genetic knockdown of mTOR slows proliferation in PXGL cells
Left: Proliferation curves of PXGL cells transiently transfected with Rictor, Raptor and control siRNAs.
Right: Cell numbers under different conditions on day 2 of the proliferation assay (day 5 post-transfection). siRNA effectivity reduced 5-6 days after transfection, particularly Rictor.

2.6 mTOR pathway activity in human vs mouse pausing

To investigate whether human and mouse cells interpret the mTOR inhibitor similarly during prolonged treatment, I next compared levels of mTOR downstream targets in PXGL and RSeT hPSCs and mouse ESCs. For this, I stained normal and paused cells for phospho-S6, phospho-4EBP1 and phospho-AKT and applied image-based single-cell quantifications. pS6 was completely lost in paused human PXGL and RSeT cells as well as mouse cells **(Figure 61)**. Similar to pS6, p4EBP1 was diminished in most cells **(Figure 61)**. pAKT showed a significant decrease in all cells, which was however stronger in mouse ESCs and particularly variable in RSeT hPSCs **(Figure 61)**. These results suggest that translation is more strongly and uniformly repressed under prolonged mTORi treatment in both species, which is accompanied by a significant, yet more variable AKT response.

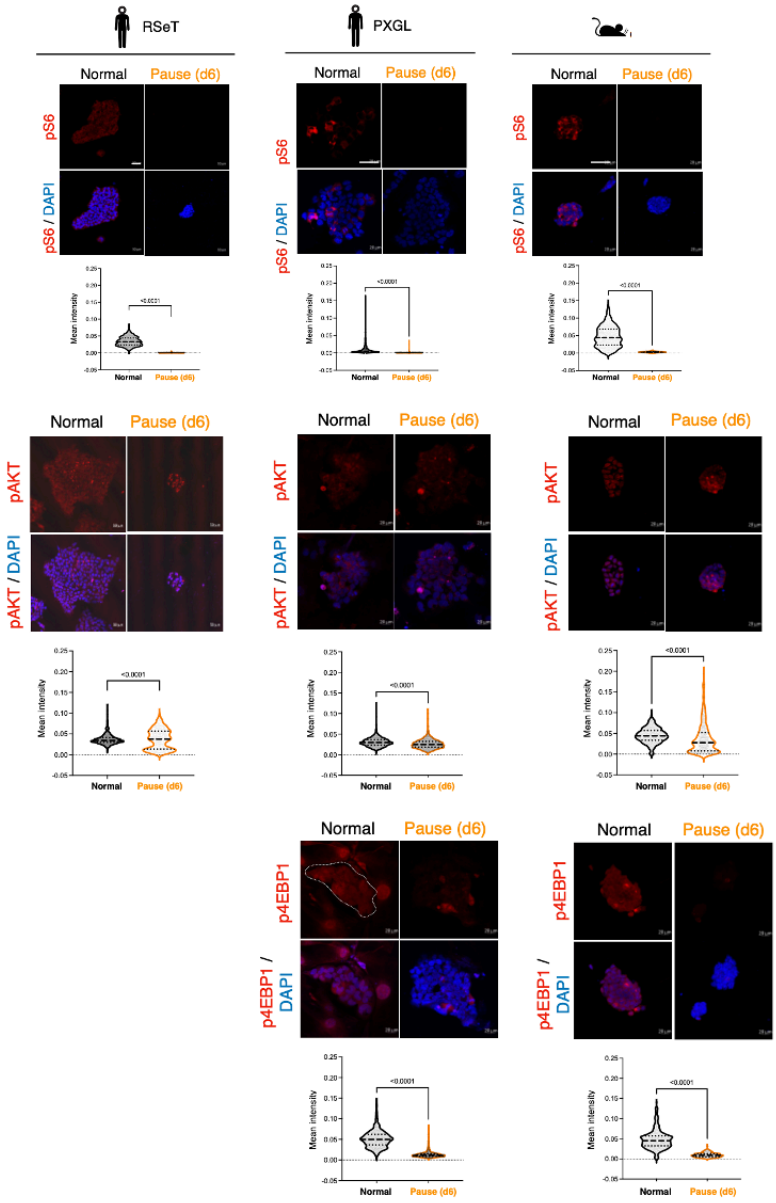

Figure 61: Levels of mTOR downstream targets in paused human and mouse ESCs.
Immunofluorescence data for mTOR downstream targets pS6, pAKT and p4EBP1. The bottom panels show single-cell quantifications of fluorescent intensities. Statistical test is two-tailed Kolmogorov-Smirnov t-test. Scale bars = 50µm.

2.7 Pausing is reversible at the molecular level in hPSCs

Until now I have shown that human PSCs have the capacity to undergo dormancy via mTOR inhibition which is functionally reversible where cells revert back to their normal proliferative state once mTOR inhibition is removed. I have also shown that during the period of dormancy, hPSCs retain their pluripotent colony morphology without compromising on their genome integrity. Since I have shown the phenotypic reversibility of hPSC pausing, I next wanted to investigate if this is reflected at the molecular level to identify pause-responsive genes and their ability to show reversibility upon dormancy exit.

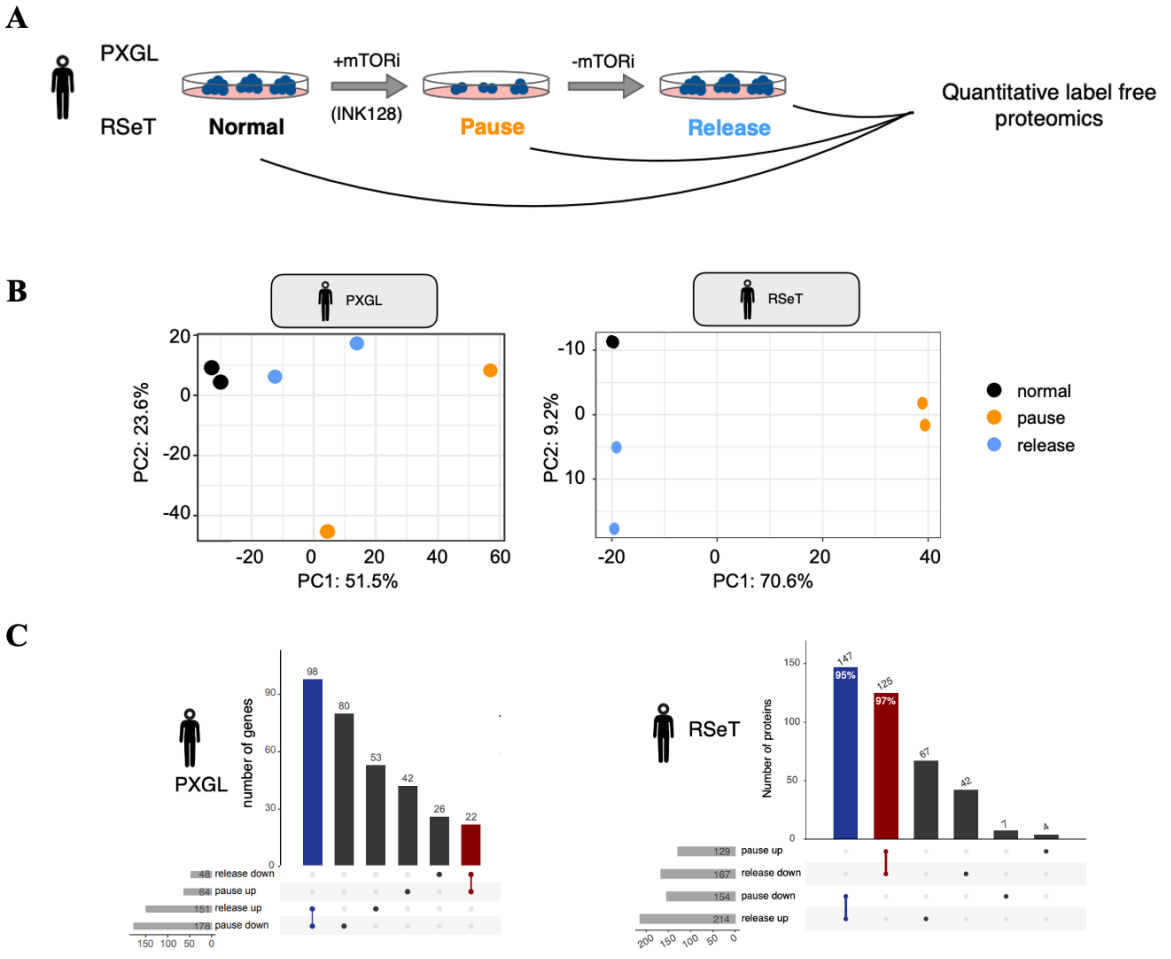

Figure 62. Reversibility of human PSC pausing at the molecular level
A. Schematics showing normal, paused and released human PSCs in PXGL and RSeT conditions were collected and subjected to quantitative label-free mass spectrometry.
B. Principal component analysis of top 500 variable proteins in indicated conditions in PXGL and RSeT culture.
C. Overlap of differentially expressed (DE) proteins in human PXGL and RSeT cells upon pause and release. In RSeT cells, 95% of DE proteins that are upregulated during pause are downregulated in release. 97% of DE proteins that are downregulated during pause are upregulated in release.

To compare the PXGL and RSeT conditions, with the help of the mass spectrometry facility at MPIMG performed quantitative label-free proteomics on normal, paused and release cells **(Figure 62 A)**. My colleague Vera performed principal component analysis (PCA). PCA showed a clear separation of normal and paused PSCs. The PCA also shows that the distinct paused state is clearly reversible in RSeT cells, while in the PXGL cells, the reversibility was more heterogeneous **(Figure 62 B)**. As expected, both paused PXGL and RSeT cells showed global downregulation of proteome when compared to normal proliferating cells. 321 and 392 proteins were significantly differentially expressed (DE, adjusted p-value <0.05 and log2FC>1) in PXGL and RSeT conditions, respectively **(Figure 62 C)**.

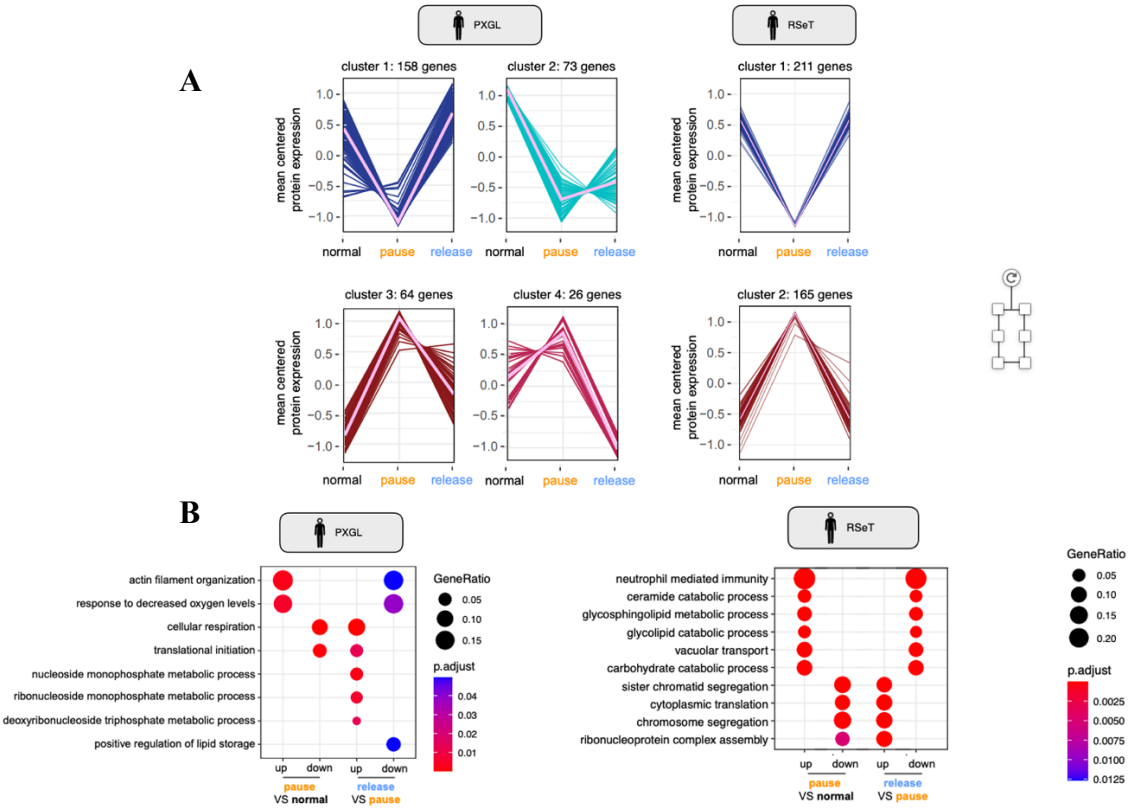

Figure 63. Reversibility of human PSC pausing at the molecular level

A. K-means clustering of downregulated or upregulated genes during pausing shows reversibility of expression pattern. Scaled log2(LFQ+1.1) values are shown. RSeT shows complete reversibility of expression patterns for 95% and 97% of genes in each cluster.

B. Gene ontology analysis of differentially expressed proteins in paused and released PXGL and RSeT cells.

To investigate the recovery of protein expression levels and patterns in released cells, DE proteins were subjected to k-means clustering **(Figure 63 A)**. We observed that both at the individual protein level and pathway level the pause response was largely reversible where cells reverted back to normal state after release from mTOR inhibition **(Figure 63 B)**. RSeT cells showed complete reversibility in gene expression pattern while in PXGL cells the restoration of gene expression was more heterogenous.

In general, pausing decreased anabolic activities such as translation, transcription, splicing, and RNA/protein export. Few cytoskeletal and metabolic pathways were upregulated. RSeT cells showed downregulation of cell division, which can be attributed to the earlier observed findings.

The above results again stress the point that hPSCs respond to pausing with varying efficiency and that pausing is reversible. The earlier results showing the phenotypic reversibility is also largely reflected at the molecular level in pause release cells of both naïve and naïve-like cells.

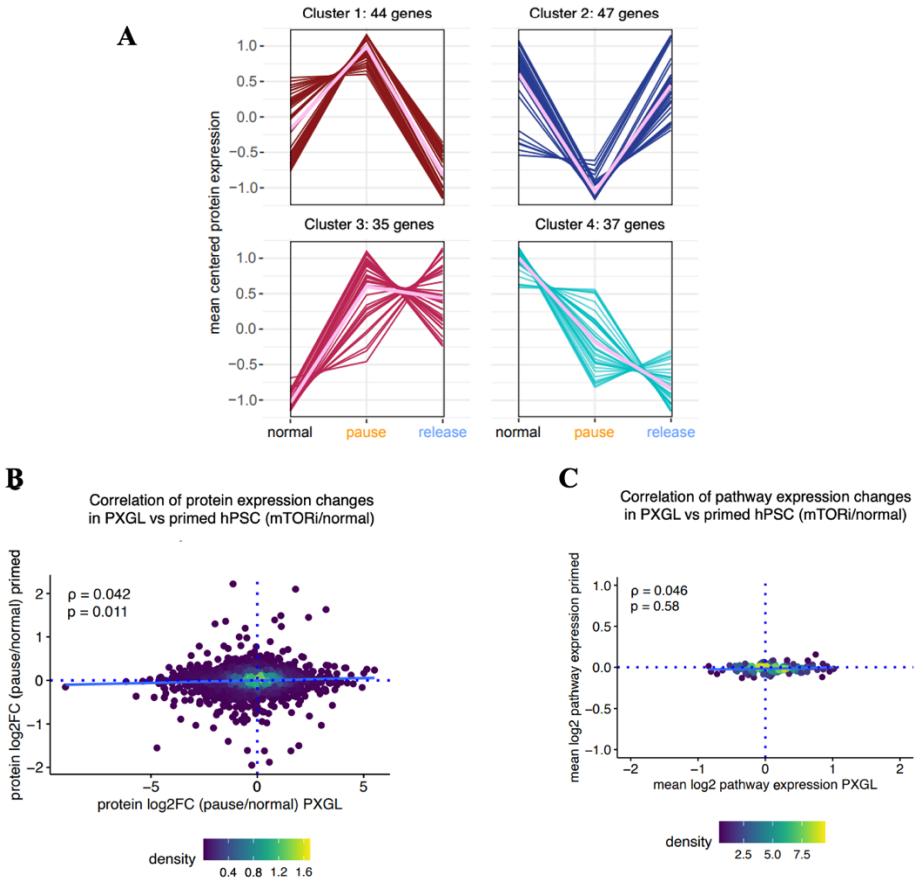

Figure 64. Characterization of the paused proteome of primed mTeSR hPSCs
A. K-means clustering of upregulated and downregulated proteins in primed hPSCs upon mTORi treatment.
B and C. Density plots showing the levels of protein **(B)** or pathway **(C)** expression in mTORi primed hPSC compared to PXGL cells. ρ, Spearman's Rho correlation coefficient.

As opposed to PXGL and RSeT cells, primed hPSCs treated with 100 nM INK128 showed fewer differentially expressed proteins in pause, of which only ~56% showed reversible expression **(Figure 64 A)**. Importantly, the response of primed hPSCs did not correlate with PXGL cells at the individual protein or pathway level **(Figure 64 B and C)**. Thus, the molecular characterization as well as the morphology of primed hPSCs under mTORi do not indicate a stable pause response as seen in PXGL and RSeT cells.

2.8 Developmental delay of human blastoids in extended pre-implantation culture

Until now I have tested the capacity of human cells to undergo dormancy in an *in vitro* setup where I have shown that human PSCs can be subjected to iterative pausing and release and that the process of pausing via mTORi is phenotypically and molecularly reversible.

Next, we took advantage of using the human blastoid model recently developed by our collaborators in IMBA, Vienna. Blastoids are embryonic stem cell-derived structures that are morphologically and transcriptionally highly similar to the human blastocyst (modeling days 5 to 7)[57]. The advantage the blastoid system brings is its high throughput nature which allows one to overcome the material and ethical limitations of human embryo research. Additionally, attachment or *in vitro* implantation of blastoids induces expansion and maturation of embryonic and extraembryonic cells, recapitulating these early post-implantation events and thereby allowing to test the reversibility of dormancy.

My colleague Heider Heidari Khoei tested the effect of mTOR inhibition on blastoid survival. For this blastoids were first cultured in a normal culture medium (see methods for culture conditions). Once blastoids were formed, they were grown in the presence of mTOR inhibitor Rapalink-1. RapaLink-1 is significantly more efficient in inducing mouse diapause compared to INK128 only. We observed that in the presence of Rapalink-1, the blastoids were able to maintain their morphology with an intact ICM and expanded blastocoel for a period of several days **(Figure 65 A)**. In contrast, the majority of blastoids growing in a normal culture medium collapsed by day 2. During the course of mTORi, the TE of the blastoids continued to grow in number whereas the ICM retained their original number **(Figure 65 B)**. This is also observed in *in vitro* and *in vivo* diapausing mouse embryos where we observe the TE increase in number **(Figure 65 C)**.

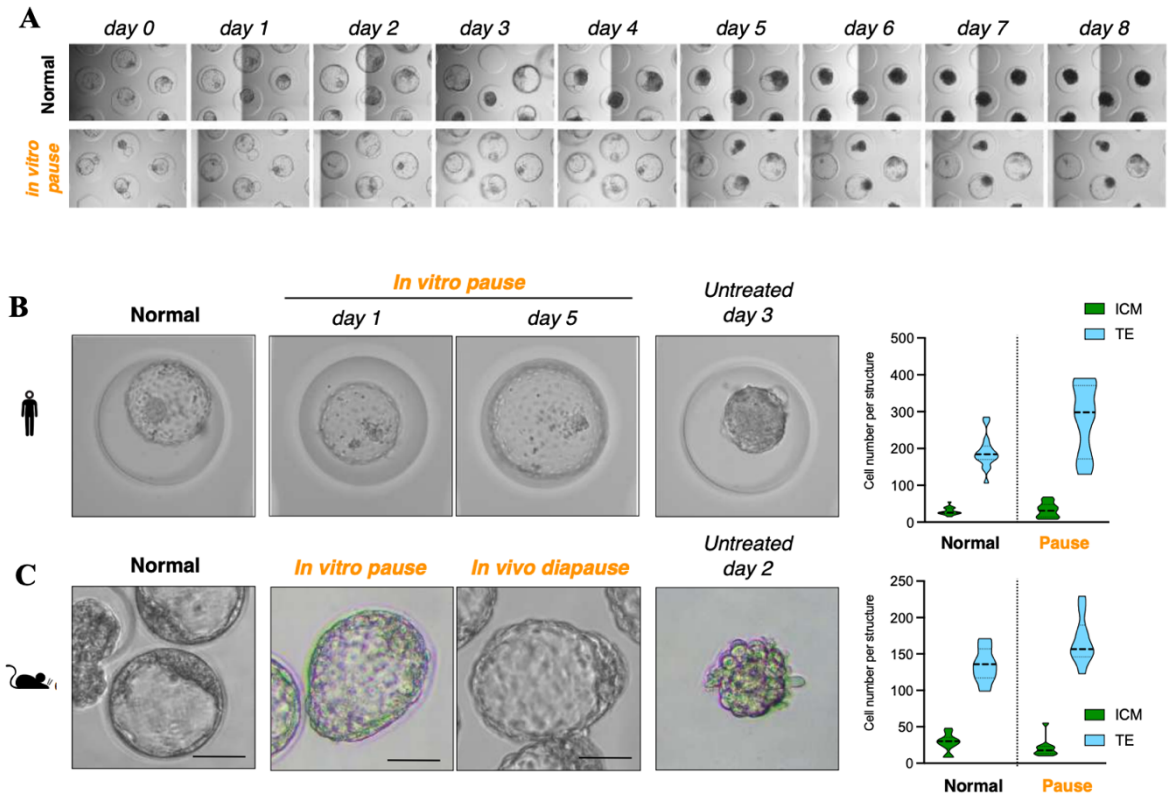

Figure 65. mTOR inhibition extends the development time of human blastoids.
A. Bright filed images showing blastoids in control and mTORi culture conditions. Days 1-8 indicate the time after blastoid formation (after 96 hours starting from ES culture).
B. Bright field images of normal and paused blastoids in comparison to untreated blastoid in extended culture. Right panel shows ICM and TE numbers based on immunofluorescence stainings.
C. Bright field images of normal and pause mouse blastocysts (*in vitro* and *in vivo* paused) in comparison to untreated blastocyst in extended culture. Right panel shows ICM and TE numbers based on immunofluorescence stainings.

Thus, mTORi induces similar, diapause-like morphological changes in both mouse embryos and human blastoids. Overall, ~50% of human blastoids could be maintained in culture for 5 days, with a subset persisting until day 8 across different concentrations of Rapalink-1 **(Figure 66 A)**.

Next, we wanted to investigate whether these paused blastoids were pluripotent and showed markers for extraembryonic lineages. Heider performed an IF to score for the above marks. Paused blastoids showed markers for pluripotency and extraembryonic cells just like normal untreated blastoids **(Figure 66 B)**.

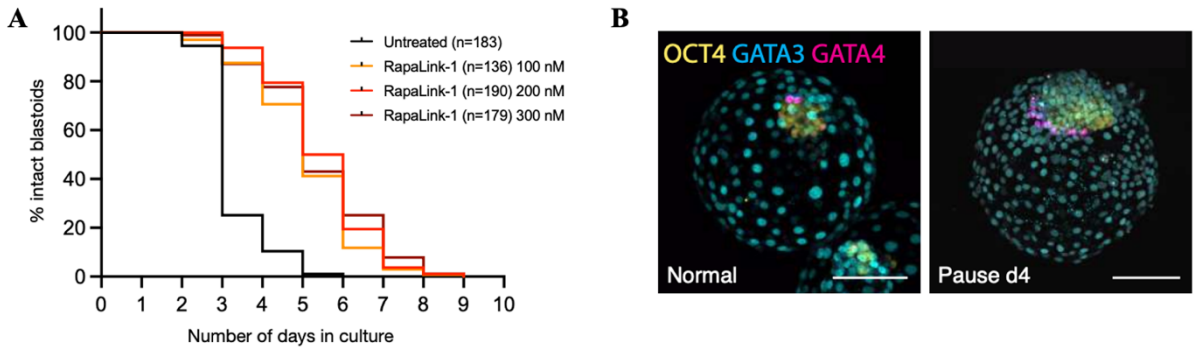

Figure 66. mTOR inhibition extends the development time of human blastoids.

A. Survival curves of blastoids in normal and mTORi cultures. The survival curves have been scored for blastoids in paused conditions using three different concentrations of Rapalink-1. Blastoids are not considered intact after the structural collapse of blastocoel.

B. IF stainings of blastoids for ICM marker Oct4, TE marker GATA3 and PrE marker GATA4. 16 control and 15 paused blastoids were stained. 3/15 paused and 2/16 control blastoids show linearly organized PrE layer.

This fulfills the major criterion of diapause namely the stabilization of germ layers of the embryo over an extended time period. Next, to prove that the pausing of blastoids is mediated by the mTOR pathway and not merely brought by inhibited protein synthesis, we treated the blastoids with cycloheximide (CHX). Treatment with CHX did not extend the survival of the blastoids **(Figure 67 A)**. Interestingly at high CHX concertation of 1000ng/ml, the TE of the blastoids was able to pause but at the expense of the ICM **(Figure 67 B and C)**. The CHX experiments show that mTOR brings about a structural re-wiring of the genome and is not limited only to regulating protein synthesis.

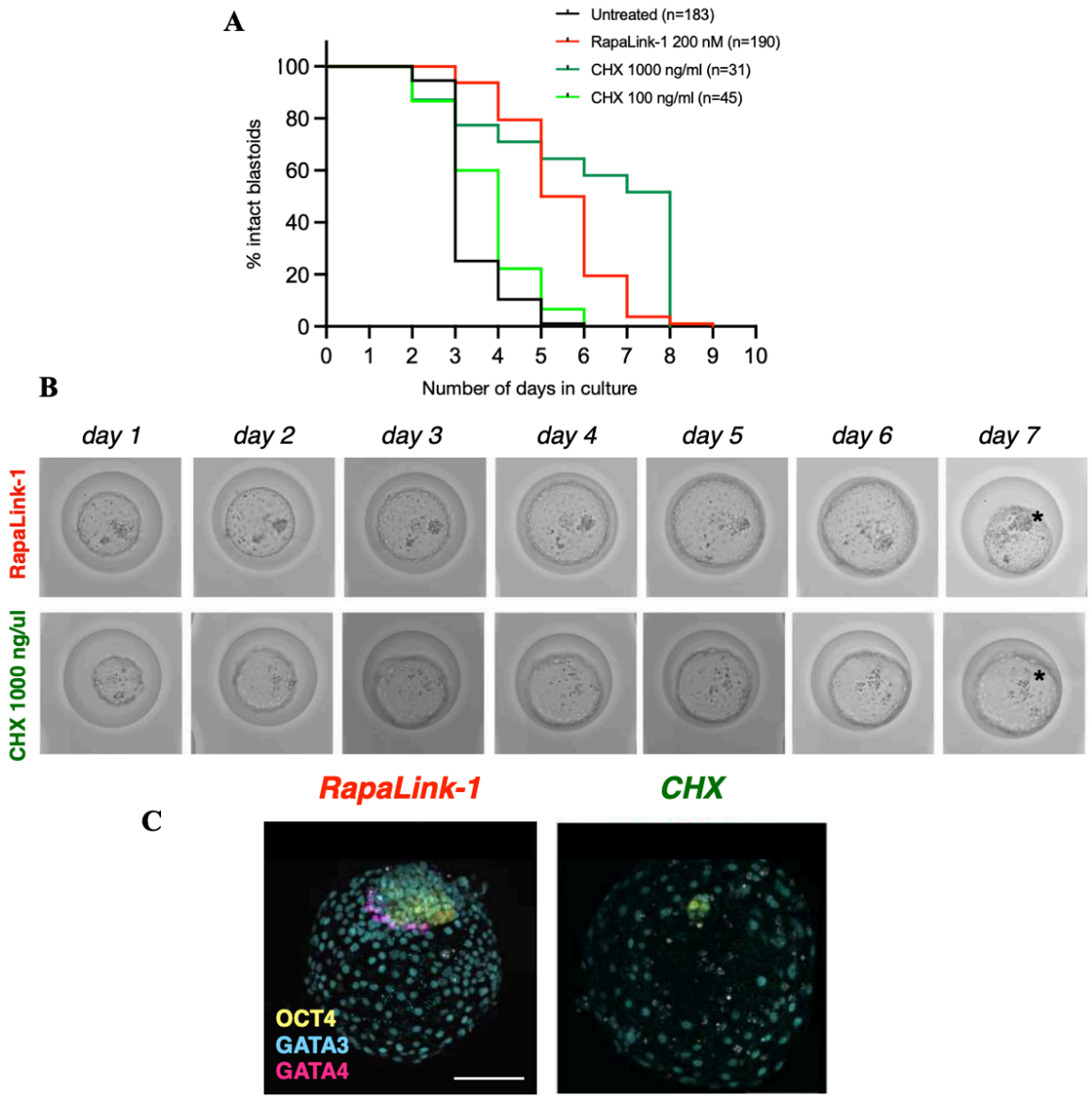

Figure 67. Inhibition of protein translation does not extend blastoid survival.
A. Blastoid survival curve in control, Rapalink-1 and CHX conditions. Blastoids are not considered intact after the structural collapse of blastocoel. n = number of blastoids.
B. Bright field images of blastoids in Rapalink-1 and CHX culture conditions. Blastoids in CHX culture were able to sustain their intact structure but at the expense of ICM (see astrix).
C. Immunofluorescence staining of blastoids in Rapalink-1 and CHX. The stainings confirm the loss of OCT4+ cells in blastoids grown in CHX culture.

Just like the mouse *in-vitro* paused blastocysts have the capacity to reactivate and implant upon receiving growth cues, I was curious to know, whether the extended
blastoid culture under mTOR inhibition is reversible. To test this Heider reactivated paused blastoids after 2-6 days of mTORi treatment and cultured them on matrigel coated dishes. The attachment of blastoids to the matrigel-coated dishes was 100 % in all the reactivated conditions. After 2-4 days of post-implantation culture, we were able to see TE layer differentiating which was confirmed by performing IF for CK7 and CGB **(Figure 68 A)**. We were also able to see the ICM and primitive endoderm (PrE) derivatives after 2-4 days of post-

implantation culture. We noted that there were more PrE cells compared to ICM after day 6 of blastoid activation **(Figure 68 B)**. This skewing towards PrE might be because of the specific reactivation conditions.

The above results show that the pausing is reversible and the capacity to reactivate and further differentiate is retained in human blastoids, thus fulfilling a further criterion of diapause.

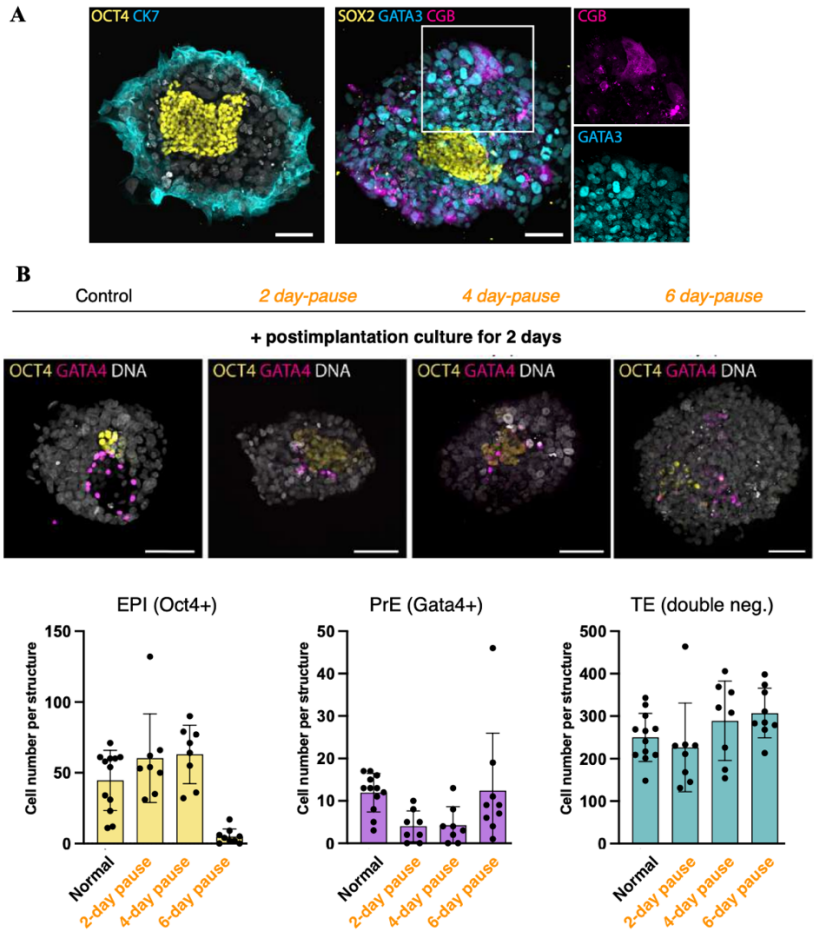

Figure 68. Reactivation of blastoids after extended culture.
A. Blastoids after 4 days of pausing were reactivated by plating them on matrigel-coated dishes. Derivates of TE (differentiation markers CK7, CGB), ICM (Sox2), TE (GATA3) were scored by immunofluorescence.
B. Blastoids were cultured in mTORi condition for 2-6 days. They were then reactivated by plating them on matrigel-coated dishes. After 2 days of reactivation, the blastoids were stained for ICM marker OCT4, PrE marker GATA4. Number of cells from each lineage were quantified. Scale bars = 100µm.

2.1.9 Species-specific tempo and metabolism of developmental pausing

The developmental time window for humans and mice is different and I was curious to know whether dormancy establishment in these two species happens at similar or distinct paces. To explore this idea, I collected mouse serum/LIF ESCs and human PXGL cells at various time points of pausing up to 10 days to get a time resolution of the pausing process in these 2 species

and performed proteomics **(Figure 69)**. My colleague Vera then performed the correlation analysis.

Figure 69. Comparison of developmental timing and metabolic pathways during human and mouse dormancy. PXGL cells and mouse ESCs (serum/LIF) were treated with mTORi and the cells were collected at the indicated time points for low-input mass spectrometry. To investigate reversibility, cells were released from pausing and collected 8 days later. Both the cell types were cultured in parallel using the same batch of inhibitor.

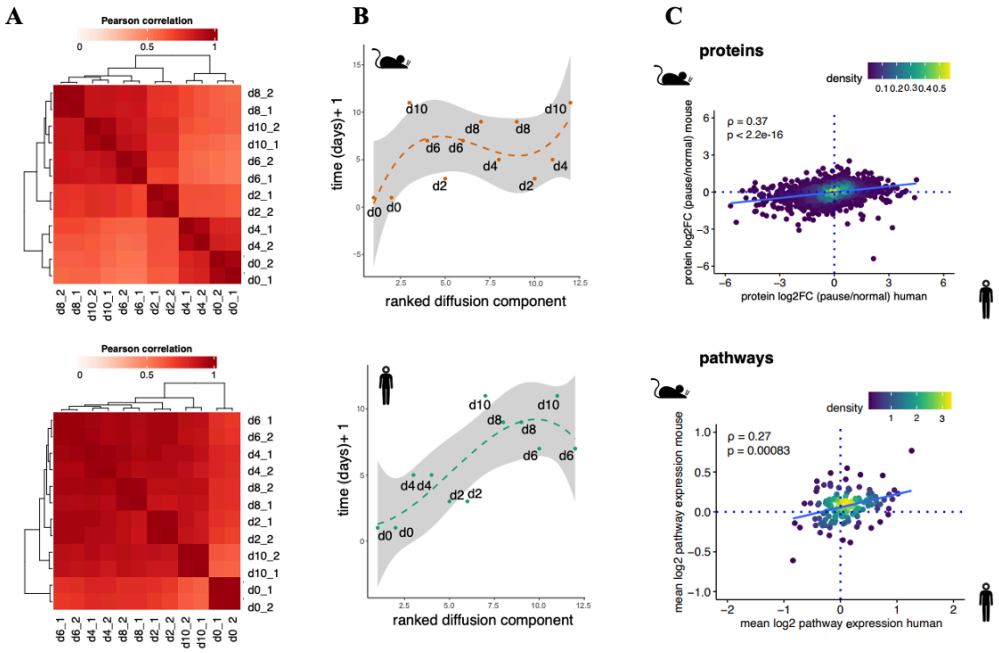

Figure 70. Comparison of developmental timing and metabolic pathways during human and mouse dormancy.

A. Correlation matrices of human (PXGL) and mouse ESCs. Two replicates were collected on the indicated days of proteomic analysis.

B. Pseudotime analyses of human or mouse ESCs undergoing pausing based on ranked diffusion components. The dashed line and grey shading show the median and confidence interval, respectively. Each dot shows a replicate collected on the indicated day of mTOR treatment.

C. Density plots showing the levels of protein (top) or pathway (bottom) expression in human and mouse cells in pausing relative to normal culture. Proteomic and pathway alterations in response to pausing show a statistically significant correlation in both species. ρ, Spearman's Rho correlation coefficient.

Correlation matrices of longitudinal samples showed different ‘breakpoints' in human and mouse cells, after which the paused proteomic signature was stabilized for human = d6, mouse = d2 **(Figure 70A)**. To corroborate the above data further, Vera used the time-course proteomics data to construct pseudotime trajectories using ranked diffusion components. This approach also pointed to d6 in humans and d2 in mice as the observable time points, after which the pseudotime no longer consistently progressed, and thus stabilized **(Figure 70 B)**. These results strongly suggest a species-specific tempo of PSCs to enter into a state of paused pluripotency. Once stabilized, human and mouse pause proteomes correlated at the protein and pathway levels **(Figure 70C)**.

Next with the aim of knowing the pathways that are important for dormancy maintenance, we chose time points after stabilization into dormancy day 8 in humans and day 4 for mice. The data showed that most anabolic pathways like ribosome, basal transcription, and protein export were downregulated in both species. Whereas pathways related to cell adhesion, and repair pathways were upregulated **(Figure 71 left)**. Apart from the common shared pathways, we also identified species-specific pathways utilized during dormancy. These mostly comprised of metabolic pathways, with lipid and amino acid metabolism specifically upregulated in the mouse; and sugar metabolism specifically upregulated in the human **(Figure 71 right)**. These differences may also be due to different culture conditions used in growing PXGL and mouse ESCs. For example, wnt inhibitors are used in PXGL culture which is absent in mouse ESC culturing (see methods for culture details). These observations point towards the use of common non-anabolic pathways by the 2 species as a response to mTORi-induced pausing at the same time requiring species-specific metabolic activity for establishment of pausing.

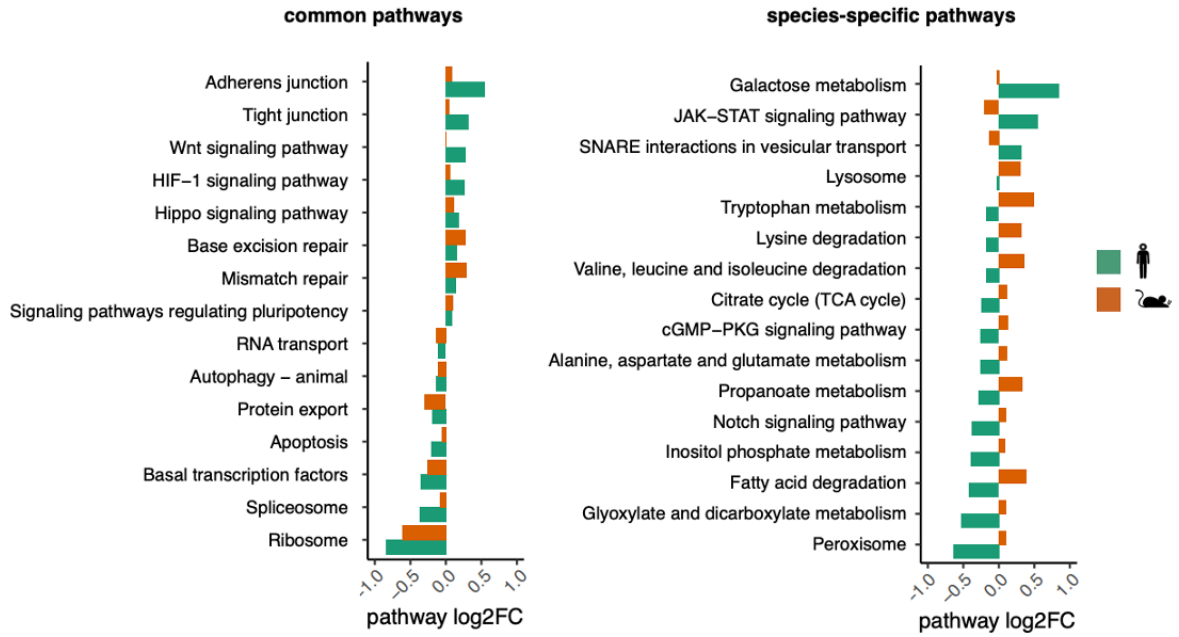

Figure 71. Comparison of developmental timing and metabolic pathways during human and mouse dormancy. Common and species-specific pathways in human and mouse paused ESCs. Basal transcription and translation pathways are downregulated; while DNA repair proteins are upregulated in both species. Metabolic profiles are strikingly species-specific.

Finally, we used the human blastoid model to corroborate the species-specific metabolic requirements from the above proteomics data. The above data shows lipid oxidation as one of the major pathways utilized by mouse ESCs for energy utilization during the diapause period. It has been shown in our lab and from the literature that fatty acids derived from lipid droplets are actively used during mouse diapause[113] and that enhancing fatty acid oxidation by L-carnitine supplementation significantly prolongs in vitro pausing duration of mouse blastocysts[124]. Consistent with species-specific energy sources, adding L-carnitine to the human blastoid culture during pausing did not alter the culture duration **(figure 72 A and B)**.

The above results allow us to understand specific metabolic requirements for species to undergoing diapause. The knowledge obtained here would help us to tweak culture conditions to have a more optimal culture for human blastoids to undergo prolonged dormancy which can eventually be extended to human blastocysts.

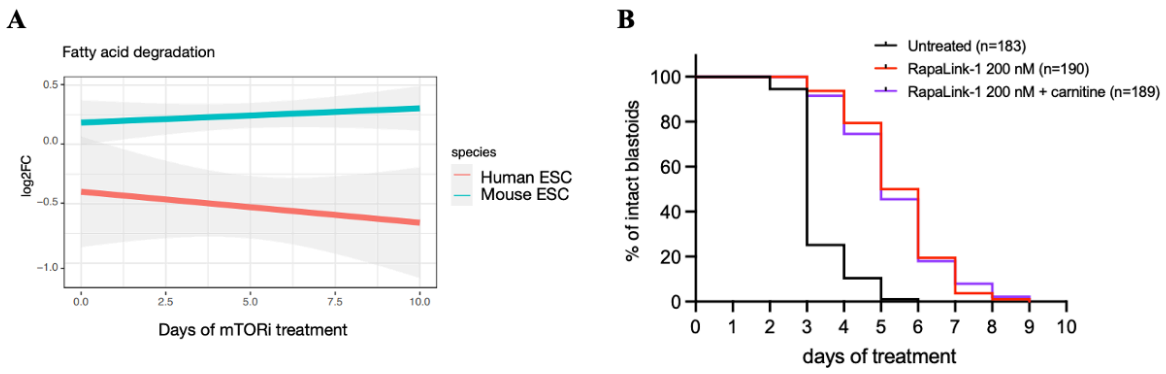

Figure 72. Carnitine supplementation does not further extend blastoid development in mTORi conditions.
A. Temporal expression of the fatty acid degradation pathway during mTORi treatment in mouse and human ESCs. Plot shows mean log2FC of proteins in the pathway (per KEGG annotation) on dx/d0, together with confidence interval. Human pausing does not depend on fatty acid oxidation for their survival.
B. Culture duration analyses of paused blastoids with or without carnitine supplementation. Enhancing fatty acid degradation does not prolong pausing of human blastoids, unlike mouse blastocysts. n = number of treated blastoids.

Discussion

mTOR inhibition induces reversible dormancy in human pluripotent stem cells and blastoids.

Embryonic dormancy or diapause is a reproductive strategy employed by many mammalian species when encountered by unfavorable conditions. mTOR which is a nutrient-sensing pathway plays an important role as a central regulator of dormancy across mammalian species. It acts as a rheostat in governing the proliferative and dormancy decisions of a cell. It has been shown earlier that inhibition of the mTOR pathway (mTORi) induces a diapause-like dormant state in mouse ESCs and in mouse embryos. Mouse embryos under mTORi can be reliably maintained in a quiescent state for a period of weeks without compromising the identity of the 3 germ layers namely the trophoblast (TE), inner cell mass. (ICM) and the primitive endoderm (PrE). Although dormancy is well characterized in mouse ESCs, the main question of human PSCs undergoing dormancy still remains unanswered. In the second part of my PhD thesis, I for the first time show the possibility of a dormancy-like state in human PSCs and blastoids and the route taken by these cells for dormancy establishment.

A similar pattern of mTOR expression is shared by human and mouse embryos

Since mTOR is the key regulator for cell growth, proliferation and quiescence it was necessary for me to explore whether human and mouse embryos have similar patterns of mTOR expression. Immunofluorescence of pS6 an immediate downstream mTOR target showed a high degree of similarity in expression pattern in the embryos from both species with polar TE showing high pS6 expression and weaker expression in mural TE and in the ICM **(Figure 46 A)**. This points to the possibility that human embryos could use the same primordial pathway to regulate their metabolic activity and time their development. Just like the mouse blastocyst embryos, human embryos react positively to IGF1 treatment as shown by pS6 staining and also an increase of epiblast number **(Figure 47 B and D)** showing mTOR is active and tightly regulated even in human embryos. IGF1 acts upstream of mTOR and depletion of nutrients and growth factors such as IGF1 inhibits mTOR activity which in turn induces diapause in mice. This opens the possibility of diapause also occurring in human embryos by mTOR inhibition.

Extension of blastoid culture upon mTOR inhibition

mTOR has a prominent role in human preimplantation development. Inhibiting the mTOR activity by the use of small molecule inhibitor Rapalink-1 prolonged blastoid culture for up to 8 days **(Figure 65A)**. Just like in the mouse blastocyst pausing[114] the pausing of human blastoid shows an increase in TE number, whereas the ICM cell number remained **constant (Figure 65 B and C)**. This differential TE dynamics during dormancy remains to be explored. It has to be noted that unlike mTORi pausing, only translational inhibition does not allow the blastoid to undergo dormancy, where only the TE survives at the expense of ICM. Thus, showing that the mTORi-mediated pausing does not only involve translational inhibition but a change in the structural rewiring of the genomic, transcriptional and metabolic landscape. From these results,

we can also infer that the survival of the TE is not dependent on the ICM **(Figure 67)**. It would be interesting to explore whether the differential DNA methylation landscape between ICM and TE cells is the reason why TE behaves differently during mTOR-mediated dormancy. It's known that mESCs show an increase in heterochromatic regions during dormancy[124]. If the formation of new heterochromatic regions is critical for dormancy establishment, then this could explain why the hypomethylated TE genome responds differently to mTORi-mediated dormancy. It can be presumed that the hypomethylated genome gives additional access to new regions for the PRC2 complex to bind. This can dilute the number of PRC2 to an extent that it is unable or there is a reduced binding of the complex to its intended regions. This might result in reduced deposition of H3K27me3 which might reflect on decreased heterochromatic regions in TE during dormancy[156].

Once established, the paused blastoids reactivate upon mTORi withdrawal. When cultured on matrigel-coated plates, the reactivated blastoids show TE, ICM and primitive endoderm cell derivatives with TE cells further differentiating to express CK7 and CGB **(Figure 68 A)**. These results show that pausing of blastoids is reversible and upon reactivation retains the capacity to differentiate, fulfilling the criteria of reversible diapause.

Human PXGL (naïve) and RSeT (naïve-like) cells but not mTeSR (primed) cells show reversible dormancy at the functional and molecular level

Previously it has been shown that mouse PSCs can undergo diapause upon mTORi and transcriptionally resemble a diapaused epiblast. To further investigate the possibility of human PSCs adopting a dormant, I subjected human naïve, naïve-like and primed PSCs to mTOR inhibition. Primed human PSCs showed altered, flat network morphology under low mTORi concentration and upon release reverted back to normal proliferation and morphology but failed to give rise to teratomas **(Figure 53)**. Naïve and naïve-like cells entered dormancy with varying efficiency. This might be due to differences in culture conditions, different stages in the cell cycle during the time of dormancy entry or lack of the presence of extraembryonic cells might be the contributing factors for this varied response. The high rate of apoptosis observed in naïve-like cells during dormancy might also be due to the fact that unlike the naïve-cells the naïve-like are cultured in feeder-free plates which may elude them from getting access to critical ECM materials. Analyzing the transcriptome profile at the single-cell level can help us to understand the underlying cause of heterogeneity. Compared to mouse PSCs, human PSCs are more challenging to culture under mTORi as they periodically require ROCK inhibitor for stabilization, particularly at the time of passaging.

Once established and stabilized, paused hPSCs reactivate upon mTORi withdrawal. The pause-release cells show greater proliferation as shown by the increase in mitotic cells **(Figure 56)** and faster teratoma formation **(Figure 51 B)**. This might be due to the selection of cells with high base-line mTOR activity.

Pause-induced changes in naïve and naïve-like PSCs reverted back to the original expression pattern both at the gene and pathway level upon mTORi removal. Naïve-cells showed more heterogenous reversibility when compared to naïve-like cells. In both cell types, many of the anabolic activities such as translation, transcription, protein export, etc were down-regulated upon pausing. This downregulation of anabolic activity during mTORi might be brought by the activity of the proteasome system. It is known from the literature that proteasomal activity helps in extending longevity in worms[157] also its activity is increased when mTOR is inactive which is essential for downregulating all anabolic processes[158]. It is also known that human ESCs have a high proteasomal activity for pluripotency and proteostasis maintenance (Schröter and Adjaye.,2014). It would be interesting to explore the role of proteosomes in dormancy establishment and whether their activity in naïve and naïve-like PSCs is essential for down-regulating anabolic processes. Since naïve-like cells come from an iPSC background, it is worth comparing the proteasomal activity between ESCs and iPSCs. This comparison could also shed light on the varying efficiencies with which these two types of human PSCs respond to dormancy via mTOR inhibition with naïve-like cells showing high apoptosis.

Species-specific route of developmental pausing

Temporal dynamics comparison between human and mouse cells by pseudotime proteomic analysis showed that mouse cells by day 2 stabilize their paused proteome while human cells take time to stabilize their paused proteome until day 6 **(Figure 70 B)**. This is probably because of the extended preimplantation time window in humans when compared to mouse preimplantation development. Both species correlate more at the pathway level than at the gene level **(Figure 70 C)**. At the pathway level, both species showed downregulated RNA and protein anabolic processes and upregulated in their DNA repair and cell adhesion. However, there are few species-specific pathway utilization. Lipid oxidation was upregulated during mouse dormancy and sugar metabolism was upregulated in human dormancy. This was corroborated with survival data for blastoids where supplementation with L-carnitine[124] did not have any additive effect on the length of dormancy during blastoid pausing **(Figure 72 B)**. This data can be used to tweak the paused blastoid culture conditions such that we obtain better survival of paused blastoids and hopefully extend the culturing days further from the present 8 days.

Implications of the study

Human embryos show variability in capacity to progress through early development where a majority fail to undergo proper development after pregnancies. Genetic or non-genetic factors may be the reason for such abnormalities. The second part of my thesis will help us to understand the process of early development in humans and help in improving embryo development and health. The study of dormancy in human stem cells will help increase our understanding of the functioning of the pluripotency network and how its long-term maintenance helps in maintaining embryo identity during extended survival. Embryo dormancy could provide the researchers with a valuable time window for genetic testing of embryos and synchronizing the embryo development with the mother's hormonal cycle. The

results of IGF1 favoring blastocyst formation rate can be applied for better embryo development in an IVF setting.
The results show a differential response of human PSCs to mTORi-mediated pausing where naïve-like cells show more apoptosis compared to naïve ESCs. It should be noted here that naïve ESCs are cultured on MEFs (feeder dependent) and naïve-like PSCs are cultured in a feeder-independent way. This points towards the direction of understanding the importance of the feeder layer in contributing towards dormancy by the supply of essential extracellular matrix (ECM) components. The contribution of ECM towards stabilization of pluripotency to a naïve or naïve-like state should be studied extensively as it may have an influence in modulating the metabolic environment and in turn the chromatin landscape mediated via adhesion signaling.

Limitations of the study

Although I used blastoids that imitate a human blastocyst, it is important to test the effect of dormancy via mTOR inhibition on human embryos to confirm that human development can also be altered by preserving its differentiation capacity. Human blastoids show a lot of variability in terms of ICM cell numbers from culture to culture, this variation could have an effect on the number of PrE cells being expressed. This skews the data during mTORi pausing when studying germ layer preservation. Another drawback of the study is that the developmental potential of the paused blastoids has not been tested extensively. ES and TS cells should be derived from the paused blastoids and cultured together to derive post-implantation structures. This would show that the paused hPSCs are developmentally competent by preserving their identity and differentiation capacity during the dormancy period.

Open questions to be answered

I have noticed that during hPSCs pausing, particularly RSeT cells, the nuclei of the paused cells appeared to have a distorted morphology with a high DAPI intensity **(Figure Top panel)**. While the nuclei of the normal and paused released RSeT cells have a normal rounded morphology. To investigate it further, my colleague Vera stained normal, paused and pause-release mouse blastocysts with Lamin B1**(Figure Bottom panel)**. Diapaused mouse embryos were collected from ovariectomized mice on day 3 of in vivo diapause. What I observed was a pronounced change in nuclear structure in both paused moue blastocyst and RSeT cells. Lamin B1 staining shows nuclear wrinkling happening during dormancy which returned back to its original shape and morphology upon reactivation. Similar morphological changes of the nuclei were also observed in in vitro-paused mouse blastocysts. This shows that dormancy brings changes to nuclear morphology in both species.

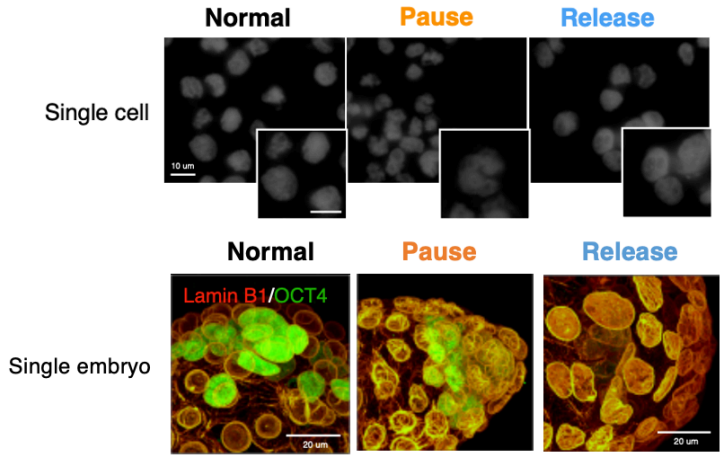

Figure: Nuclear morphology before, during and release from mTORi pausing in RSeT cells and mouse embryos. Top: nuclear morphology depicted with DAPI stain in RSeT cells. **Middle:** nuclear morphology depicted with Lamin B1 stain (Red) in mouse embryos.

Investigating the observed changes in nuclear morphology is important to understand how the nucleus and the chromatin are preserved during conditions of stress and whether the resulting changes in nuclear architecture reflect on preserving cellular identity by insulating the genetic material from stress-induced damage.

A) Understanding how nuclear deformation is formed in dormant hESCs

Our mass spectrometry data points in the direction of increased calcium signaling. From the literature, it is known that calcium signaling of the endoplasmic reticulum (ER) is predominant during cellular stress and has been linked to monitoring nuclear morphology[159]. It would be ideal to inhibit ER-calcium signaling in paused hESCs and see for changes in nuclear morphology. If any changes are observed it would be useful to do a phosphoproteome mass spectrometry to look for proteins having altered phosphorylation with a focus on the lamin family. Generating a phospho mutant of lamins involved will allow us to know that they are directly involved in nuclear wrinkling or folding during hESC dormancy.

If the above holds true, it would be ideal to know how ER-calcium is responsible for changing the phosphorylation status in lamins. Again, from our mass spectrometry data, we see an upregulation of cellular adhesion proteins **(Figure 71 left)**. Piezo channels are known to communicate calcium signals to the nucleus [160]. Western blot of piezo proteins in wild type and paused hESCs will help us know which piezo proteins (piezo-1/2) are highly expressed. Genetic knockout (KO)by CRISPR-cas9 or shRNA-mediated knockdown (KD) of piezo protein will help us know the link between ER-calcium in modulating the lamin phosphorylation which is responsible for nuclear envelop folding or wrinkling.

B) Significance of nuclear envelope folding or wrinkling

Is nuclear folding critical for hESC dormancy? To answer this question, using phospho mutant engineered lamin hESC lines where the nuclear envelope remains stiff should be brought to pausing by mTOR inhibition. Paused hESCs expressing wild-type lamins would be used as controls. The above two cell lines must be checked for genome integrity by scoring for γH2A.X. γH2A.X is a DNA repair protein to be recruited first at the site of DNA damage. This data would help us to understand the critical importance of nuclear envelope folding towards maintaining genome integrity. The above data should also be supplemented with cell viability assays such as scoring for annexin V via flow cytometry.

C) Chromatin rheology during hESC pausing

From the above data, we will get to know the link between calcium signaling and phosphorylation of lamins in bringing changes to the nuclear envelope during hESC pausing. Next, to address how chromatin rheology is influenced by changes in nuclear envelope morphology using paused phospho mutant lamin, paused wildtype hESC lines as controls, IF for H3K27me3 and H3K9me3 should be done. This would tell us which of the histone marks is up or down-regulated and is responsible for chromatin stiffness – ultimately leading to compromised genome integrity. Mining the phosphoproteome data for the respective methyltransferases and manipulating their expression levels in a wild-type hESC background under paused conditions will shed light on their role in chromatin rheology and its role in genome integrity during the process.

Conclusion: The above brief experimental outline will tell us the critical nature of nuclear envelope morphology in preserving cellular identity by insulating the genetic material from stress-induced damage toward dormancy establishment in hESCs.

Combinatorial action of dormancy-associated miRNA is essential for dormancy transition in mouse pluripotent stem cells via the mTOR-TFE3 axis

The successful establishment of dormancy is an active phenomenon that involves coordinated rewiring of the transcriptional, epigenetic and metabolic landscape. MicroRNAs are small non-coding RNAs involved in regulating cell growth, proliferation, metabolic and fate transitions. They exert their regulatory influence by binding to 3'UTRs of mRNAs bringing about translational repression or mRNA decay. Although their role in mouse preimplantation development has been shown to be dispensable, here I show their indispensable role in diapause entry in mouse ESCs and embryos. In the first part of my PhD thesis, I identified miRNAs as one of the most critical regulatory layers for stress response, to enable a pluripotent cell to undergo state transition and yet maintain their cellular identity during the onset of dormancy.

Recent studies have focused only on individual miRNA roles in lifetime extension in worms and mouse and dissecting its target interaction. This gives us a limited understanding of miRNA as a key regulator of dormancy. Here through my thesis, I aimed to give a macroscopic view of the microRNA regulatory network that functions during the onset of dormancy which details the interconnectivity between microRNAs and their targets.

MicroRNAs play a vital role as an adaptive stress responder during mouse preimplantation dormancy

MicroRNAs as regulatory player fine-tunes gene expression at a post-transcriptional level for the cells to adapt to various kinds of stress. Their function is dispensable in normal cellular homeostasis. This is shown in my thesis that microRNAs are essential during the onset of dormancy by rigorously testing *Dgcr8* KO mESCs **(Figure 15)**. I show that *Dgcr8* KO cells under normal conditions proliferate at the same pace as wild-type mESCs. Unlike wild-type mESCs which readily adapt to reduced mTOR activity by slowing down its proliferation, *Dgcr8* KO cells gradually collapse under mTOR inhibition. Showing that the critical role of microRNAs is indispensable for dormancy response in mESCs. This is also seen in mTORi paused DIPLO aggregated mouse embryos where the paused *Dgcr8* KO chimeric ICM failed to survive and only the wild-type trophoblast cells survived **(Figure 18 right)**. This shows the necessity of microRNA function during dormancy which acts downstream of mTOR. RNA sequencing of *Dgcr8* KO ESCs under pausing shows an aberrant transcriptional profile compared to paused wild-type mESCs. In the absence of mature canonical miRNAs, the *Dgcr8* KO ES cells show a high propensity to upregulate genes involved in differentiation **(Figure 24)** along with genes associated with pluripotency. This dysregulation of gene expression is a result of improper transcriptional rewiring. This shows the role played by microRNAs in

correctly tuning the gene expression of a cell to actively adapt their transcriptional machinery as they transition from proliferation to dormancy.

miRNA-target network functioning during mouse diapause

I have shown very strong evidence that microRNAs have a strong regulatory role in mouse ESCs and embryos transitioning into dormancy. MicroRNAs act combinatorially on many targets affecting multiple cellular processes simultaneously. In order to have a broader view in identifying dormancy-associated microRNAs and their functioning in a larger context of regulating their downstream targets, my colleagues and I identified via integrating single-embryo and ESC-specific small RNA sequencing the microRNAs that are concordantly upregulated in *in vitro* and *in vivo* paused polar blastocyst, and in diapaused mESCs **(Figure 28)**. The data was then used to construct an *in silico* post-transcriptional regulatory network that links all microRNAs to their target genes and their interacting proteins **(Figure 31)**. miRNA-target interactions were retrieved from miRDB and miRTarBase and protein-protein interactions (PPIs) from BioGrid, together with top-scoring interactions from StringDB. In addition, we integrated the proteome data of mTORi-treated or control ESC with the miRNA expression data. The network consisted of 335 PPIs and 196 miRNA-target connections. From the network 119 out of 431 proteins were significantly downregulated while17 out of 24 miRNAs were significantly upregulated both in embryos and ESCs. The network showed miR-200 family and miR-26b-5p which are the most significantly upregulated to have prominent hubs exhibiting a high number of regulatory interactions modulating its target genes and protein levels. Additionally, we also constructed an ESC-specific regulatory network having only ESC-specific miRNA profile and proteomics data and found an additional set of 44 miRNAs and 108 gene targets. The miRNA-target network showed cellular processes such as RNA splicing, cell cycle, mRNA translation and RNA processing bodies like PML and DDX6 among others to be affected during dormancy.

Having constructed the network, its functionality was tested in diapausing embryos by perturbing the most prominent miRNA hubs – miR-200 family and miR-26b-5p with miR inhibitors. Inhibiting the function of the above miRNAs significantly reduced the survival of the diapausing embryos and the remaining surviving embryos had fewer NANOG+ cells compared to control-injected embryos. The results suggest that perturbing the miRNA network disrupts the transcriptional layer which reduces the efficiency of embryos to diapause **(Figure 35)**.

I also tested overexpression of miR-92 from the network and its influence on diapause without mTOR inhibition. Ectopic over-expression of miR-92 was sufficient to prolong the survival of intact blastocysts up to 18 days in vitro, whereas empty vector or buffer controls did not prolong survival **(Figure 37)**.

Here I have tested the functionality of the miRNA-target network that works during the cellular transition into dormancy. The perturbation effect could further be amplified if more miRNAs from the core network are targeted. Further refinement to the network can be done by including

other cell types such as polar and mural TE and primitive endoderm which are also part of the embryo. Further experiments, such as AGO pull-down and site-specific mutations, will deliver insights into each of the nodes and edges in our network.

The above results cement the fact that microRNAs are necessary for embryos to undergo dormancy. This allows us to deepen our knowledge of the regulatory mechanism that exists when a cell decides to switch from proliferative to dormant phenotype or vice-versa in response to stress or regeneration cues at the same time maintaining its cellular identity. This understanding could also be applied to cancer stem cells that also undergo repeated cycles of activation and quiescence.

Dormancy-associated miRNAs regulate RNA processing

Through rigorous testing, I have shown the working of the miRNA-target networking during mouse embryonic dormancy. As mentioned above there are many cellular processes that are regulated by miRNAs. Instead of focusing on individual miRNA-target edges, I focused on the broader in-network perturbation of cellular processes. Among the in-network proteins downregulated, proteins part of the membraneless RNA processing bodies like PML and DDX6 were predicted to be significantly downregulated. Experimental testing for these two proteins in wild-type and *Dgcr8* KO ESCs showed that PML and DD6 were highly expressed in *Dgcr8* KO cells in normal culture conditions and unlike in wild-type ESCs, *Dgcr8* KO cells failed to efficiently downregulate PML and DDX6 during dormancy transition **(Figure 39)**. Showing that the in-network predicted proteins were indeed downregulated at the protein level and the expression of the above two proteins was perturbed in Dgcr8 KO ESCs in both normal and diapause conditions.

As PML and DDX6 proteins are involved in RNA processing such as splicing, I next investigated whether alternate splicing (AS) was affected in Dgcr8 KO cells. I along with my colleague Francesca validated aberrant AS activity happening in the *Dgcr8* KO condition at both RNA and protein level (refer AS analysis, PCR and WB)

Here by taking an example of RNA processing, I was able to show how miRNA rewires cellular processes in mouse ESCs for them to transition into dormancy. In line with this, there are other multiple ways by which miRNA regulates dormancy transition by regulating other cellular processes such as cell cycle and growth. For example, PCNA (cell proliferation regulator) and RIF1 (regulator of replication timing) are downregulated by miRNAs in the network.

TFE3 is the upstream regulator of dormancy-associated miRNAs

So far, I have identified the miRNA-target network that is functioning at the time of dormancy. I have experimentally also shown how miRNAs are able to re-wire cellular processes during mouse ESCs transition into dormancy. The question that still remains to be answered is how are these miRNAs getting upregulated. To investigate this, my colleagues did motif enrichment analysis for transcription factors (TFs) that can potentially bind to the promoters of these

upregulated microRNAs. TF motif enrichment analysis pointed us towards a list of 15 TFs that could potentially bind to the promoters of the concordant upregulated microRNAs. Eliminating the TFs that are not expressed in the ESCs and found TFE3 to be a potential TF that could regulate the expression of the dormancy-associated miRNAs. IF shows increased migration of TFE3 to the nucleus in wild-type ESCs cultured in mTORi **(Figure 44 B)**. CUT&Tag showed increased TFE3 occupancy on the promoters of dormancy-associated miRNAs during pausing compared to ESCs grown in normal culture conditions and compared to control miRNAs **(Figure 45)**. miR-200a/b, which we functionally validated in previous experiments, were enriched in TFE3 binding. In summary, we identify an mTOR-TFE3-miRNA axis, which regulates the rewiring of miRNA expression and downstream protein levels in the transition of mouse ESCs from proliferation into dormancy.

The above results show that microRNAs are indispensable to the embryos to transcend into dormancy. I show here that, just perturbing a select few microRNAs from the core network can destabilize the dormancy process with specific loss of pluripotent cells and subsequent structural collapse of the embryos. This perturbation effect could further be amplified if more miRNAs from the core network are targeted. Here I also try to highlight the fact about robustness with which the microRNA network was created and experimentally validate the functionality of the network to give us a strong knowledge of the microRNAs that are responsible for dormancy transition. Perturbing the network from any node could reduce the efficiency of *in vitro* dormancy. This knowledge not only broadens our understanding of miRNAs as regulatory layer but can also be used in clinical settings as a biomarker for diagnosing diseases. This would help us in detecting diapausing embryos in other species where hormonal measures are unreliable and impractical and also to use as biomarkers for detecting dormant cancer cells.

Implications of the study

The first part of my thesis highlights the indispensability of microRNAs in dormancy transition in mouse ESCs. The data suggests that miRNAs may act as first responders by bringing rapid changes in the protein landscape suited for dormancy induction by its regulatory action at the post-transcriptional level. The identification of dormancy-associated miRNAs and developing the in-silico miRNA-target network gives us a macroscopic view of the regulatory layer that functions during dormancy. The network highlights the nexus of transcription factor acting upstream of miRNAs regulating its expression and the protein families that get regulated downstream of miRNAs. The work will help in a deeper understanding of the mechanism of stress response that mediates cell state transition and also mechanisms that help maintain cellular identity during the period of dormancy. The knowledge can be applied to existing adult stem cell models to compare similarities and dissimilarities between embryonic and adult stem cell dormancy which can help in technological advances in adult tissue preservation and regeneration. The methodology of miRNA regulation can further be expanded to other cells such as TE and PrE to find the regulatory that functions in these cells during the period of dormancy at the single cell level. This could shed light on the differential response of these cells to mTORi-mediated pausing. The network can further be utilized in identifying the

cellular processes that first get affected during entry into dormancy by looking at proteins that are significantly downregulated and how this can cause a ripple effect in regulating other downstream pathways. This would give a step-wise clarity of how rewiring of the genome happens during dormancy. miRNAs as circulating biomarkers are being used for cancer detection and prognosis. Similarly, use of miRNAs as biomarkers can help in the non-invasive detection of diapausing embryos. The use circulating miRNAs can be used as a biological tool to investigate maternal and fetal crosstalk that happens during dormancy and also investigate the maternal control over the embryos during the period of reactivation.

Limitations of the study

The miRNA-target network mainly focuses on pluripotent cells but not for other cell types such as TE and PrE. Constructing a network for these cells would give us a complete picture of the functioning of a regulatory layer in these cells and how differently they respond to dormancy signals. While the functioning of the miRNA-target network has been functionally validated, rescue experiments should be done by expressing important miRNA hubs such as the miR-200 family and miR-26b-5p in Dgcr8 KO ESCs to observe to what extent the dormancy phenotype can be rescued in these cells. Although the study shows TFE3 occupancy on the promoters of dormancy-associated miRNAs, no direct evidence has been shown here for TFE3 being the main transcriptional driver for these miRNAs. Experiments blocking the migration of TFE3 into the nucleus during dormancy should be done or mutating the TFE3 binding sites on miR-200 family and miR-26-5p to show direct involvement of TFE3 as a transcriptional regulator.

Methods

Animal experimentation

All animal experiments were performed according to local animal welfare laws and approved by local authorities (covered by LaGeSo licenses ZH120, G0284/18, and G021/19). Mice were housed in ventilated cages and fed ad libitum.

Ethics statement

Human embryos were donated to the research project by informed consent under UK Human Fertilization and Embryo Authority (HFEA) License number R0162. Approval was also obtained from the Health Research Authority's Cambridge Central Research Ethics Committee, IRAS project ID 272218 (Cambridge Central reference number 19/EE/0297). The approval process entailed independent peer review along with approval from both the HFEA Executive Licensing Panel and the Executive Committees. Our research is compliant with the HFEA Code of Practice and has undergone independent HFEA inspections since the license was granted. Patient consent was obtained from Bourn Hall Clinic. Informed consent was obtained from all couples that donated surplus embryos following IVF treatment. Before giving consent, donors were provided with all of the necessary information about the research project, an opportunity to receive counseling, and details of the conditions that apply within the license and the HFEA Code of Practice. Specifically, patients signed a consent form authorizing the use of their embryos for research including stem cell derivation and for the results of these studies to be published in scientific journals. No financial inducements were offered for donation. Patient information sheets and the consent documents provided to patients are publicly available (https://www.crick.ac.uk/research/a-z-researchers/researchers-k-o/kathy-niakan/hfea-licence/). Embryos were donated cryopreserved and were transferred to the Francis Crick Institute where they were thawed and used in the research project.

Human ESC and blastoid experiments

As required by the German Stem Cell Act, all experiments involving hESCs and/or hESC derived blastoids were approved by Robert Koch Institute, Berlin, and the Commission for Science Ethics of the Austrian Academy of Sciences. The Wicell line H9 was used under the agreement 20-WO-341 for a research program entitled 'Modeling early human development: Establishing a stem cell based 3D in vitro model of human blastocyst (blastoids)'. This work did not exceed a developmental stage normally associated with 14 consecutive days in culture after fertilization even though this is not forbidden by the ISSCR Guidelines as far as embryo models are concerned. All experiments complied with all relevant guidelines and regulations, including the 2021 ISSCR guidelines that forbid the transfer of human blastoids into any uterus[161].

Cell lines and culture conditions

Mouse ESCs: Wild-type and *Dgcr8* KO[162] E14 ESCs (received from S. Kinkley Lab, MPIMG and Constance Ciaudo Lab, ETH respectively) were used. Cells were plated on 0.1% gelatin-

coated dishes and grown in DMEM high glucose with Glutamax media (Thermo Fisher Scientific, 31966047) supplemented with 15% FBS (Thermo Fisher Scientific, 2206648RP), 1x NEAA (Thermo, 11140-035), 1x b-mercaptoethanol (Thermo Fisher Scientific, 21985023), 1x Penicillin/streptomycin (Life Technologies, 15140148) and 1000 U/mL LIF and grown at 37°C in 20% O_2 and 5% CO_2 incubator. At each passage, cells were dissociated using TrypLE (Thermo Fisher Scientific, 12604-021) with media change every day. Cells tested negative for mycoplasma.

Mouse TSCs: TSCs (received from M. Zernicka-Goetz Lab) were grown on mitotically-inactivated mouse embryonic fibroblasts in media containing RPMI1640 + GlutaMAX (Thermo Fisher Scientific, 61870010), 20% FBS, b-mercaptoethanol (Thermo Fisher Scientific, 21985023), 1x Penicillin/streptomycin (Life Technologies, 15140148), 1x sodium pyruvate, 25 ng/µl FGF4 (R&D Systems, 235-F4-025) and 1 µg/ml Heparin (Sigma, H3149). Cells were depleted off feeders before collecting for analysis. Cells tested negative for mycoplasma.

Primed human PSC cell culture

Wild-type Zip13k2 female hiPSCs (Franz-Josef Müller Lab) were cultured without feeders on Matrigel-coated plates (Corning, 354277) in mTeSR media supplemented with 10µM ROCK inhibitor (ROCKi) (Tocris, 1254) on the day of seeding. ROCKi was withdrawn the day after thawing, the media was changed every day, and cells were passaged every four days. At each passage, cells were dissociated as clumps using EDTA and re-plated with 10µM ROCKi in a split ratio of 1:5. Cells were maintained at 37°C in 20% O_2 and 5% CO_2 incubator.

Naïve-like human PSC cell culture (RSeT)

To obtain naïve-like cells, primed hiPSCs were plated at medium density (1:3-1:4 of a 75% confluent 10 cm plate) on Matrigel-coated dishes (Corning, 354277) and grown in mTeSR media for 24 hours at 37°C in 20% O_2, 5% CO_2. After 24 hours, mTeSR media was replaced with RSeT™ Feeder-Free Medium (Stem Cell Technologies, 05975), and the cells were cultured at 37°C in 5% O_2, 5% CO_2 (hypoxic condition). The cells need to undergo at least 3 passages to completely reprogram to a naïve-like state. At each passage, cells were dissociated using TrypLE (Thermo Fisher, 12604-021) and 10^6 cells were seeded on a 10 cm culture dish with 5 µM ROCKi. ROCKi was withdrawn the day after thawing.

Naïve human PSC culture (PXGL)

H9 hESCs (provided by the laboratory of Austin Smith) were used. Naive PSCs were cultured on gelatin-coated plates including a feeder layer of gamma-irradiated mouse embryonic fibroblasts (MEFs) in PXGL medium. PXGL medium is prepared using N2B27 basal medium supplemented with PD0325901(1 µM, MedChemExpress, HY-10254), XAV-939 (2 µM, MedChemExpress, HY-15147), Gö 6983 (2 µM, MedChemExpress, HY-13689) and human leukemia inhibitory factor (hLIF, 10 ng ml^{-1}, in-house made). N2B27 basal medium contained DMEM/F12 (50%, GIBCO, 11320-074), neurobasal medium (50%, GIBCO, 21103-049), N-2 supplement (Thermo Fisher Science, 17502048), B-27 supplement (Thermo Fisher Science,

17504044), GultaMAX supplement (Thermo Fisher Science, 35050-038), non-essential amino acid, 2-mercaptoethanol (100 µM, Thermo Fisher Science, 31350010), and bovine serum albumin solution (0.45%, Sigma-Aldrich, A7979-50ML). Cells were routinely cultured in hypoxic chambers (5% CO_2, 5% O_2) and passaged as single cells every three to four days. All cell lines had routinely tested negative for mycoplasma.

Developmental pausing setup

Mouse ESC/TSC pausing: ESCs and TSCs were treated with the mTOR inhibitor INK-128 at 200 nM final concentration. Media was replenished as required. ESCs were paused for 6 days and TSCs for 12 days before collection of cells for small RNA profiling.

In vitro diapause: Blastocyst-stage embryos were cultured in KSOM+AA medium (Sigma, MR-101) and treated with 200 nM of RapaLink-1 to induce diapause *in vitro.*

In vivo diapause: In vivo diapause was induced as previously described[163] after natural mating of CD1 mice. Briefly, pregnant females were ovariectomized on E2.5 and afterwards injected with 3 mg medroxyprogesterone 17-acetate subcutaneously (Sigma, M-1629) on E3.5 and E5.5. Diapaused blastocysts were flushed from uteri in M2 media after 4 days of diapause at EDG7.5.

Optimization of pause hPSC culture

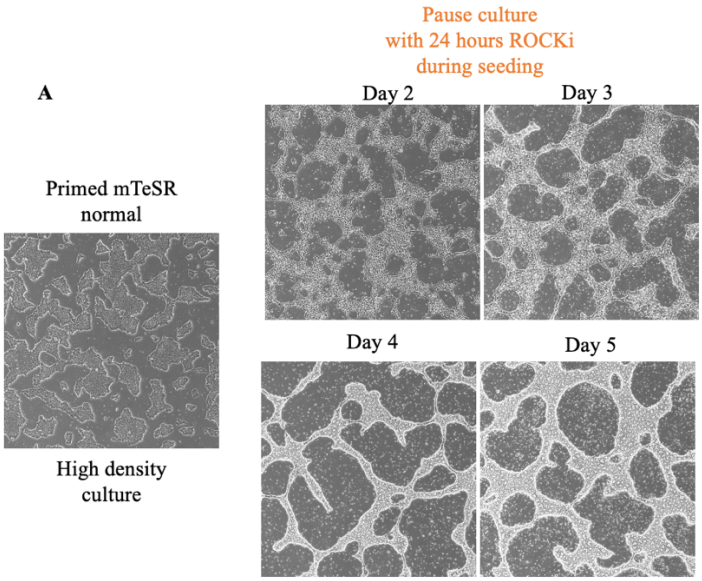

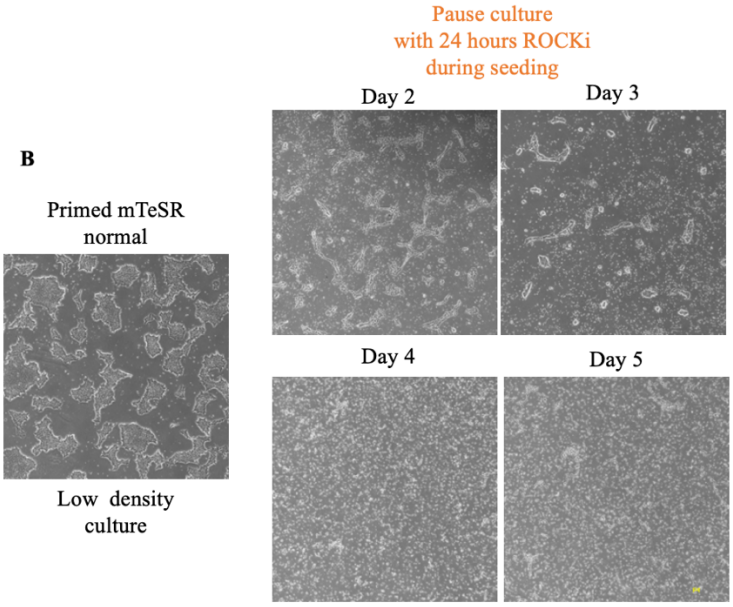

Figure I. Brightfield images of Zip13K2 hiPSC line (primed mTeSR cells) during the course of pausing. The pausing of the above cells involves a very delicate setup which involves the use of optimal cell densities for pause induction with 100nM INK128. **(A)** A high-density starting culture of mTeSR cells is optimal for inducing successful pausing. The success of pausing is determined by the ability to form a colony network from day 2 of pausing. This network formation is critical for the pause cells to survive during the period of pausing for up to 10 days (maximum testing period). **(B)** Starting with low-density or medium-density culture does not give an optimized response to mTORi-mediated pausing. The cells on day 2 fail to form a network which ultimately leads to the collapse of the cells during the pause duration.

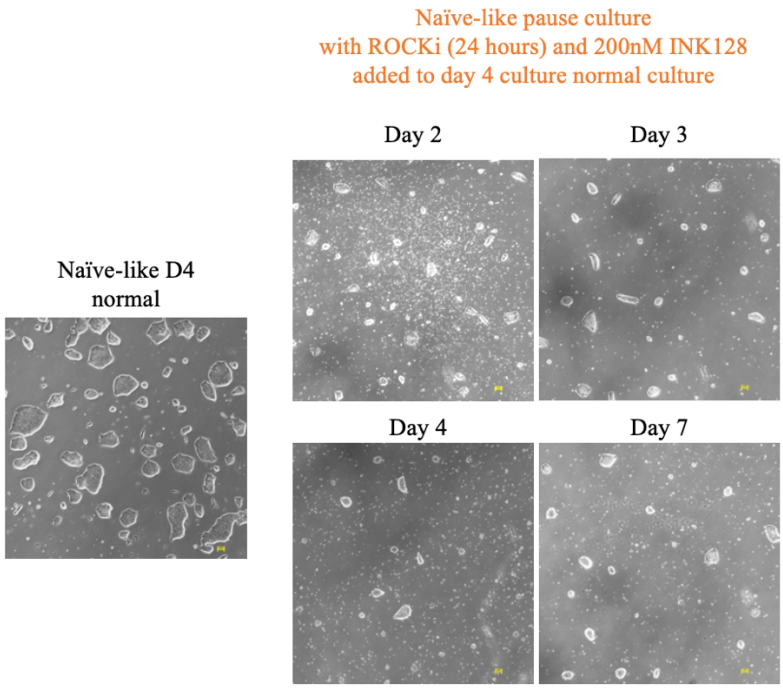

Figure II. The culture set up for naïve-like pausing. Starting from 800,000 cells, pausing is induced on day 4 of normal culture by adding 200nM INK128 along with ROCKi for 24 hours. Addition of INK128 before day 4 or after day 5 results in high cell death. The addition of ROCKi before the cell colony reaches 100μm in diameter (day 4 normal culture), results in colonies to differentiate which leads to cell death in pause conditions. Pausing of day 4 normal culture with INK128 without the addition of ROCKi does not lead to pause establishment and results in cell death within 24 hours of pause culture.

Human PSC pausing: For pausing of primed hiPSCs, cells were treated with the catalytic mTOR inhibitor INK128 (MedChemExpress/Biozol, MCE-HY-13328) at 100 nM final concentration (cells do not tolerate 200nM final concentration) and 10 μM ROCKi in mTeSR media for 1 day. The following day, ROCKi was withdrawn and cells were cultured in media containing INK128 for six days with daily media change.
For pausing of hiPSCs in RSeT culture, 10^6 cells were plated and grown in RSeT feeder-free medium. The media was changed every other day. On the fourth day of culture (approximate colony diameter of 100 μm), media containing 200 nM INK128 and 5 μM ROCKi was added for one day, then replaced with media containing only 200 nM of mTORi. Cells were cultured in INK-128 (i.e. paused) for 10 days unless otherwise stated in the legend. Media was changed every day.
For pausing of hESCs in PXGL culture, 400,000 cells were counted and plated onto confluent MEFs in PXGL media with 10μM ROCKi, Matrigel and 200 nM INK128 for one day. The next day the media was replenished with PXGL and 200 nM INK128. To validate INK128-mediated pausing, RapaLink-1 (Biozol, APE-A87764) was used at 200 nM and Torin1 (Abcam, ab218606) was used at 200-1000 nM.

Morula aggregations
Wild-type diploid morulae collected from CD1 (Hsd:ICR) females were used for aggregations. Wild-type-EGFP or *Dgcr8* KO-EGFP E14 mouse ESCs were combined with morulas as described[164]. Cells express an EGFP gene expressed from a CAGGS promoter and randomly integrated into the genome as a marker of ESC origin.

Teratoma formation
Mice were maintained under pathogen-free conditions in an air-conditioned animal facility, in a 12h light-dark rhythm and fed with sterilized standard pellets from Sniff (Soest, Germany) and acidified drinking water ad libitum. To test for teratoma formation in vivo, hiPSCs in RSeT culture were diluted 1:1 with matrigel and transplanted subcutaneously into the left flank of 6-8 week old female *NOG* mice (NOD.Cg-*Prkdc*^{scid} *Il2rg*^{tm1Sug}/JicTac, CIEA NOG mouse®, Taconic, Denmark). 1.9 x 10^6 cells were resuspended in 50 □l PBS and mixed with 50 □l Matrigel before transplantation. Mice were sacrificed after reaching a tumor volume >1.5 cm³ or after 150 days after transplantation. The tumor volume was measured using an external caliper. In order to determine the tumor volume, the greatest longitudinal diameter (length) and the greatest transverse diameter (width) were recorded. Tumor volume based on caliper measurements were calculated by the modified ellipsoidal formula. Resulting teratomas were sampled, weighed and fixed in formalin. Formalin fixed tumor samples were embedded in

paraffin. For histological examination, slices of different layers (different planes of tissue sections) were prepared and HE staining was conducted according to routine protocols. Briefly, after deparaffinization and rehydration, 5 μm longitudinal sections were stained with hematoxylin solution for 5 min followed by 5 dips in 1% acid ethanol (1% HCl in 70% ethanol) and then rinsed in distilled water. Then the sections were stained with eosin solution for 3 min and followed by dehydration with graded alcohol and clearing in xylene. The mounted slides were then examined and photographed using Zeiss Axioscope 40 microscope and screened for structures of all three germ layers (ectoderm, endoderm, mesoderm).

Human embryo culture

Vitrified embryos frozen in straws were thawed by quickly transferring the contents of the straw from liquid nitrogen directly into thaw solution (Irvine Scientific Vitrification Thaw Kit) and thawed per manufacturer's instructions. Embryos frozen in cryopets were thawed for 3 seconds in a 37 °C water bath before transferring into thaw solution (Irvine Scientific Vitrification Thaw Kit). Embryos frozen in glass ampoules were thawed completely in a 37 °C water bath after the top of the vial was removed under liquid nitrogen. The contents were emptied onto a petri dish and the embryo transferred through a gradient of sucrose solutions (Quinn's Advantage Thaw Kit, Origio) per manufacturer's instructions. Embryos were routinely cultured in Global Media supplemented with 5 mg/mL LifeGlobal Human Protein Supplement (both LifeGlobal) pre-equilibrated overnight in an incubator at 37 °C and 5% CO_2. These conditions were supplemented with IGF1 (291-G1/CF, R&D) at a final concentration of 1.7 or 17 nM.

Human blastoid formation and inhibitor treatments

Naive hPSCs were cultured under humidified conditions at 37°C in an incubator with 5% O_2 and 5% CO_2. Naive H9 hPSCs were cultured on mitotically inactivated mouse embryonic fibroblasts (MEFs) in PXGL medium. The medium was changed every day. The cells were passaged 4 d before blastoid formation. Blastoids were formed as previously published with minor modification. Naive hPSCs were harvested using Accutase. The cells were resuspended in PXGL medium supplemented with 10 μM Y-27632 (MedChemExpress), seeded onto gelatin-coated plates and incubated at 37 °C for about 70 min to exclude the MEFs. The unattached cells were collected, pelleted through centrifugation, and resuspended in N2B27 medium containing 10 μM Y-27632 (aggregation medium), after which cells were seeded onto an array of 400-μm microwells inserted into a well of a 96-well plate. Agarose microwell arrays were casted using a custom PDMS stamp into 96-well plates[16,17]. Approximately 45 cells were seeded for each microwells in the arrays. After 24 hours, the aggregation medium was replaced with N2B27 medium supplemented with 1 μM PD0325901, 1 μM A83-01, 1 μM 1-oleoyl lysophosphatidic acid sodium salt (Tocris, 3854), 10 ng ml^{-1} hLIF and 10 μM Y-27632. The medium was refreshed every 24 h. After 4 days, blastoids were treated with following inhibitors; 100, 200 and 300 nM RapaLink-1, 200 nM INK128, 2,5 and 25 μM 10058-F4, 100 and 1000 ng ml−1 cycloheximide and 200 nM Rapamycin. The phase-contrast images were acquired using Thermo Fisher scientific EVOS cell imaging system. The number of blastoids in the microwells were counted manually for each well every day. For the survival curves, only visible blastoids in the microwells were counted.

Blastoid reactivation after pausing

Paused blastoids were reactivated by culturing them in an extended culture condition previously published for human blastoids. Blastoids were selected using a mouth pipette, washed with CMRL1066 medium and transferred into wells of a 96-well plate coated with Matrigel containing pre-equilibrated media. For the first day, the culture medium was CMRL1066 supplemented with 10% (v/v) FBS, 1 mM L-glutamine (Gibco), 1× N2 supplement, 1× B27 supplement, 1 mM sodium pyruvate (Sigma) and 10 μM Y27632. After 24 h, half of the medium was replaced with a new medium including 5% Matrigel. After 48h, 50% of medium was replaced with a new medium supplemented with 20% (v/v) FBS and 5% Matrigel. After 72h, half of the medium was replaced with a new medium supplemented with 30% (v/v) KSR and 5% Matrigel. Cultures were fixed for staining after 2 or 4 days of culture with 4% PFA.

Bulk RNA-seq

800,000 wild-type or *Dgcr8* KO mouse ESCs in normal or mTORi culture (day 2) were used. Total RNA was extracted using the RNeasy extraction kit (Qiagen, 74104). 1 μg of total RNA was used for standard library preparation using NEBNext PolyA mRNA magnetic isolation module (NEB, E7490). In brief, polyA mRNA isolation was done followed by first-strand and second-strand cDNA synthesis. Double-stranded cDNA was purified using AMPure beads (Beckman Coulter, A63881). Adaptor ligation was performed in a 5-fold diluted ice-cold adaptor dilution buffer. PCR enrichment of adaptor-ligated DNA was done using the following conditions: Initial denaturation - 98C for 30 seconds; Denaturation - 98C for 10 seconds ; Annealing - 65C for 75 seconds (8 cycles) ; final extension - 65C for 5 minutes. Purification of the PCR reaction was done using AmPure beads. Library quality was assessed by running samples on Tape Station (Agilent, 4150).

Small RNA-seq on ESCs and TSCs

Sample preparation: Small RNA was extracted using miRNeasy kit (Qiagen, 217004). In brief, the cell pellet was homogenized in Qiazol and incubated on a benchtop for 5 min. Chloroform was added to the homogenate and was shaken vigorously for 15 sec and incubated at room temperature for 3 min. The homogenate was centrifuged at 12000 g for 15 mins at 4C. To the aqueous layer, 70% ethanol was added and shaken vigorously. The sample was then pipetted into the RNeasy Mini spin column and centrifuged at room temperature. The flow-through contains the miRNA and other small RNA. To the flow-through, 100% ethanol was added and shaken vigorously. The sample was pipetted into an RNeasy MinElute spin column (Qiagen Cat No: 74204). The column was washed with buffers RWT, RPE, and 80% ethanol. Small RNAs were extracted in 14ul of RNase-free water.

Library preparation and sequencing: 10 ng RNA was used as input. Small RNA libraries were prepared using the SMARTer smRNA-seq Kit for Illumina (Takara, 635031) with 12 amplification cycles followed by bead size selection (ratio 0.95x-0.7x), followed by an additional clean-up step with the bead-to-sample ratio of 0.95x. Library QC was done using Qubit and BioAnalyzer and the final libraries were quantified using KAPA Library Quantification Kit (Roche, 07960140001). Libraries were diluted to 2 nM final concentration

for pooling. Pooled libraries were sequenced on a HiSeq4000 flowcell with single-end 75 bp reads to get ~15M reads per sample.

Ultra low-input small RNA-seq on dissected embryos

Sample preparation: Normal blastocysts at E4.5, in vivo paused blastocysts at EDG7.5, and mTORi-treated blastocysts were used for microdissection. Laser-assisted separation of ICM and mural trophoblast was performed using a Hamilton Thorne XYRCOS laser system with power set to 100% and a pulse length of 300 µs (see Supplementary Video 1). For dissection, blastocysts were fixed between two holding pipettes. While the holding pipettes were carefully pulled apart, cellular connections were cut by successive laser pulses, allowing the separation of the blastocyst into pieces containing ICM or mural trophectoderm. Immediately after separation the tissue fragments were transferred into 7 µl PBS and frozen down on dry ice.

Library preparation and sequencing: Small RNA libraries were prepared using the "TrueQuant small RNA-Seq" kit from GenXPro (Germany) according to the manual. The method is based on a single-tube protocol for ligation of UMI-containing adapters to RNA molecules followed by Reverse Transcription and PCR[56]. No size selection of the small RNAs was performed. Small RNAs were amplified with 12-20 cycles to reach the required amounts for sequencing. Sequencing was performed on an Illumina NextSeq500 instrument with 1x75 bps.

Small RNA-seq data analysis

Mapping and quantification:

The miRDeep2 (v2.0.1.2)[165] algorithm was applied for quantification of miRNAs across samples, using the reference annotations of mature and hairpin miRNAs from miRBase[58] (version 22). The steps of the algorithm include preprocessing and quality control of reads, alignment of reads (mapper.pl script, options -j -l 17, other options set to default) with ambiguous reads assignment and multi-loci reads processing (default: maximum of 5 multi-site mapping), and quantification of miRNAs against miRBase mouse mature and hairpin sequences, after filtering for other non-coding RNAs. Across samples, an average of 44.5% of reads were aligned. The quality of quantification was confirmed by evaluating Pearson correlation of read counts between replicates for each set of conditions across experiments, observing an average correlation of 0.944.

Differential expression analysis:

Differential expression analysis was applied for each experiment using DESeq2[166], comparing each set of condition samples against the control samples for both samples representing embryonic fate and samples representing extraembryonic fate separately. Low read count miRNAs were discarded by keeping only those miRNAs showing a normalized read count above 5 in at least 3 samples. Read-counts quantification was transformed into regularized log counts for downstream analyses such as PCA visualization of samples. Differentially expressed genes were identified with thresholds $|\text{logFoldChange}| \geq \log2(1.5)$ (representing an increase or a decrease of at least half the value in the control samples) and adjusted p-value<0.1 (Benjamin-Hochberg correction).

Differential expression status agreement and clustering:

From the results of DESeq2 differential expression analyses across experiments, logFoldChange values of miRNAs from each analysis were aggregated into a single table. The

concordance of differential expression status for each miRNA was evaluated for each group of experiments by comparing the logFoldChange sign and magnitude. To systematically identify groups of miRNAs with concordant patterns across ESCs and embryo experiments, we applied hierarchical clustering to the miRNA fold change profiles (with Ward's linkage for clusters distance and Euclidean distance between pairs of miRNAs). We calculated the average silhouette coefficient, which measures the homogeneity within clusters versus the distance between clusters) for an increasing number of clusters (2 to 30), and selected the final number by maximizing this silhouette score, balanced by the number of clusters. The final indexing of clusters per experiment reflects the number of miRNAs within the cluster, from 0 the smallest cluster to N the largest cluster. Clustering was performed for the following groups of experiments separately: ESCs versus Blastocyst-polar, TSCs versus Blastocyst-mural, and Blastocyst-polar versus Blastocyst-mural. For each group, average logFoldChange values were calculated for each cluster, and clusters grouping miRNAs with concordant logFoldChange (either positive or negative across all comparisons) were extracted for downstream regulatory network analyses.

Nanostring

Quantification: Total RNA was isolated using the Rneasy extraction kit (Qiagen, 74104). 150 ng of total RNA in a volume of 3 µl was used as the starting material. miRNA sample preparation and miRNA CodeSet hybridization were done following the manufacturer's protocol (MAN-C0009-07). The Sprint cartridge was then run on nCounter® Sprint Profiler. Quantification data was generated using nSolver from Nanostring. Of the four housekeeping genes, B2m was barely expressed across all samples, so normalization was done only using the following 3 housekeeping genes : Actb, GAPDH, and Rpl19. A total of four samples were quantified: ESC-WT (2 replicates, samples 01 and 02) and mTORi paused ESC (2 replicates, samples 05 and 06).

Differential expression: RCC values were extracted so as to be used for differential expression using DESeq2 with RUV correction[167] . This correction method allows for exploring and removing components of unwanted variations detected in the data. The first component of unwanted variation was removed. From the available housekeeping genes, B2m was confirmed to be too little expressed to be used for housekeeping genes normalization. Actb appeared as differentially expressed in ESCs on day 6 of pausing, but was still included as housekeeping for normalization. DESeq2 is then applied to the transformed values of the measured mouse miRNAs. Differentially expressed miRNAs were identified using the following thresholds: absolute log2FC greater or equal to log2(1.5), and adjusted P-value lower or equal to 0.1.

Global proteomics

Sample preparation: Proteomics sample preparation was done according to a published protocol with minor modifications[168]. In brief, 5 million cells in biological duplicates were lysed under denaturing conditions in 500 µl of a buffer containing 3M guanidinium chloride (GdmCl), 10 mM tris(2-carboxyethyl)phosphine, 40 mM chloroacetamide, and 100 mM Tris-HCl pH 8.5. Lysates were denatured at 95°C for 10 min shaking at 1000 rpm in a thermal shaker and sonicated in a water bath for 10 min. 100 µl lysate was diluted with a dilution buffer

containing 10% acetonitrile and 25 mM Tris-HCl, pH 8.0, to reach a 1 M GdmCl concentration. Then, proteins were digested with LysC (Roche, Basel, Switzerland; enzyme to protein ratio 1:50, MS-grade) shaking at 700 rpm at 37°C for 2 h. The digestion mixture was diluted again with the same dilution buffer to reach 0.5 M GdmCl, followed by a tryptic digestion (Roche, enzyme to protein ratio 1:50, MS-grade) and incubation at 37°C overnight in a thermal shaker at 700 rpm. Peptide desalting was performed according to the manufacturer's instructions (Pierce C18 Tips, Thermo Fisher Scientific). Desalted peptides were reconstituted in 0.1% formic acid in water and further separated into four fractions by strong cation exchange chromatography (SCX, 3M Purification, Meriden, CT). Eluates were first dried in a SpeedVac, then dissolved in 5% acetonitrile and 2% formic acid in water, briefly vortexed, and sonicated in a water bath for 30 seconds prior to injection to nano-LC-MS/MS.

Run parameters: LC-MS/MS was carried out by nanoflow reverse phase liquid chromatography (Dionex Ultimate 3000, Thermo Fisher Scientific) coupled online to a Q-Exactive HF Orbitrap mass spectrometer (Thermo Fisher Scientific), as reported previously[169]. Briefly, the LC separation was performed using a PicoFrit analytical column (75 µm ID × 50 cm long, 15 µm Tip ID; New Objectives, Woburn, MA) in-house packed with 3-µm C18 resin (Reprosil-AQ Pur, Dr. Maisch, Ammerbuch, Germany).

Peptide analysis: Raw MS data were processed with MaxQuant software (v1.6.10.43) and searched against the mouse proteome database UniProtKB with 55,153 entries, released in August 2019. The MaxQuant processed output files can be found in Table S6 , showing peptide and protein identification, accession numbers, % sequence coverage of the protein, q-values, and label-free quantification (LFQ) intensities.

Low-input proteomics: 5000 cells per sample were lysed in a denaturing buffer, reduced and alkylated, and sequentially digested by Lys-C and trypsin. Peptides originating from about 1000 cells were loaded onto Evotips Pure (Evosep, Odense, Denmark) according to manufacturer protocol. Peptide separation was carried out by nanoflow reverse phase liquid chromatography (Evosep One, Evosep), using the Endurance column (15 cm x 150 µm ID, with Reprosil-Pur C18 1.9 µm beads #EV1106, Evosep) with the 30 samples a day method (30SPD). The LC system was online coupled to a timsTOF SCP mass spectrometer (Bruker Daltonics, Bremen, Germany) applying the data-independent acquisition (DIA) with parallel accumulation serial fragmentation (PASEF) method[7]. MS data were processed with Dia-NN (v1.8) and searched against in silico predicted mouse or human spectra[8].

Differential expression analysis and enrichment analyses:

The protein levels across the three replicates of each condition were extracted from the reported label-Free Quantification values from the mass spectrometry experiment. Protein intensities were scaled by the median value per sample. No proteins were removed for the differential expression analysis. The analysis was performed using Limma[170] and Limma-Voom[171]. We applied a threshold of $|\log FoldChange| \geq \log2(1.5)$ and a threshold of adjusted P-value>0.1 for the identification of differentially expressed proteins. GO-term and pathway enrichment analyses were performed with the online tool WebGestalt[172], using the non-redundant sets of GO terms, and the KEGG pathways. Default parameters were kept, notably for filtering categories (minimum number of genes: 5 per category, maximum number: 2000) and for

correction for multiple testing (Benjamini-Hochberg correction, FDR<0.05 for filtering significant categories).

Differential expression analysisfor human and mouse PSCs: The Differential Enrichment analysis of Proteomics data (DEP) package v1.16.0 was used in R for proteomics data preparation and the statistical analysis[173]. For human iPSCs, the label free quantification (LFQ) values were filtered. Only proteins quantified in both replicates of at least one condition were kept. Number of proteins kept after filtering: 4470 in PXGL, 4615 in RSeT, 5872 in primed conditions. For mouse ESCs, only proteins quantified in at least 2 out of 3 replicates of at least one condition were kept. A total of 4,783 proteins were kept after filtering. Both human and mouse proteomics data was background-corrected and normalized by variance stabilizing transformation. Missing values were imputed using random draws from a Gaussian distribution centered around a minimal value. Proteins with a p.adj < 0.05 and $|\log_2 FC| > 1$ were considered differentially expressed.
Scatter plots: The global change in proteome profile was displayed by the mean LFQ values in normal vs paused iPSCs and were generated using ggplot2.
GO term analysis: To identify enriched Biological Processes, Gene Ontology analysis in the clusterProfiler R package was applied on the differentially expressed proteins (DEPs) with a p.adj < 0.05 and |log2FC| of >1[12]. The Benjamini-Hochberg correction was used to correct for multiple comparisons and a pvalueCutoff of 0.05 and qvalueCutoff of 0.1 were used. Enriched biological processes were displayed with a cnetplot and dotplot. Selected biological processes were displayed with ggplot2.

Global proteomics: human-mouse comparison
Pairwise protein expression analysis: A total of 2861 proteins were expressed in both human (PXGL) and mouse data. The $\log_2 FC$ of paused vs proliferating of all overlapping proteins was plotted with ggscatter and the Spearman's Rho correlation coefficient was calculated.
Pairwise pathway expression analysis: KEGG[174] pathways containing at least 10 genes symbols were included in the pairwise pathway expression analysis. A total of 146 pathways were shared between mouse and human data. The pathway expression value was defined as the mean $\log_2 FC$ of proteins between paused and proliferating mouse ESCs and human naïve iPSCs, or between different culture consitions for human PSCs. Pathway and gene $\log_2 FC$ for human and mouse are provided in Table S4. The mean $\log_2 FC$ for each pathway for human and mouse data was plotted with ggscatter and the Spearman's Rho correlation coefficient was calculated.

Pseudotime analysis
Data was filtered with only those proteins remaining that were expressed in both samples of at least one condition. Data was normalised and missing values were imputed using random draws from a Gaussian distribution centred around a minimal value with the DEP package. Proteins expressed in both the human and mouse ES cells were used to compute a diffusion map pseudotime with the destiny package (v3.10) in R (version 4.2.1). The species-specific data was used to generate a pseudotime based on the ranked diffusion component, using destiny package.

miRNA-target network

Predictions of miRNA-targets were gathered from the miRDB database (V6.0), annotated into three categories of confidence (low, medium, high) following the official documentation on the confidence score (associated thresholds: ≥50, ≥60, ≥80). Only medium and high-confidence miRNA-target interactions were retained for downstream analysis. In addition, experimentally validated interactions from miRTarBase V8.0 were included, retaining only functional interactions. This led to a total of 705,242 edges (664,660 from miRDB, 30,795 from miRTarBase, 9,787 from both) between 1,998 miRNAs and 17,802 proteins. Annotation of the edges and their nodes was done using the log2FoldChange values obtained from miRNAs and proteomics differential expression analyses comparing mTORi paused ESC against controls. We established a score for the edges defined as the difference of log2FoldChange values between the miRNA and the target measured protein. Such score emphasizes the expected negative regulation of miRNAs onto their target translation so that a highly up-regulated miRNA linked to a highly down-regulated protein will lead to a highly positive edge score. This resulted in a subset of 80,099 edges with annotated scores, for 558 miRNAs and 5,019 targets. From these edges, three subnetworks were built after filtering for connections between miRNAs and proteins with non-zero logFoldChange values. First, subsets of miRNAs of interest were defined based on their differential expression values either from the mTOR-inhibited paused ESC analysis, or from their joint patterns evaluated across pausing experiments of ESC and Blastocyst-polar cells. The first network consists of regulatory relationships between the 24 concordantly upregulated miRNAs between ESC and embryos and their targets. , yielding 5,234 miRNA-target edges with 2,104 unique proteins. As the 1% of top-scoring edges yielded only 3 miRNAs, we relaxed the threshold down to the top 10%, yielding a subnetwork of N=196 edges between 17 unique miRNAs and 172 proteins. The second network consisted of the same 24 miRNAs, relaxing the score threshold down to the top 30% of miRNA-target regulatory interactions. This allowed us to explore additional regulatory relationships that do not exhibit strong regulatory patterns (i.e. strong target downregulation upon miRNA upregulation), and so discover miRNA-target subnetworks with milder phenotypic changes, but nonetheless putatively still important in the context of pausing. We finally constructed a third network from the ESC experimental data only, considering the full set of miRNAs with a positive logFoldChange from the differential expression analysis of mTOR-inhibited ESCs. As this resulted in a large network, we selected and inspected for downstream analysis only the top 1% of highest-scoring miRNA-target connections, yielding a subnetwork of N=355 edges with 55 unique miRNAs and 266 proteins.

Multipartite miRNA-protein and protein-protein networks

To address how perturbation of miRNAs propagates downstream and which other proteins or subnetworks are impacted by the deregulated miRNAs, we extended the miRNA-target network to a multipartite network of miRNA-targets and protein-protein interactions assembled from multiple sources of gene connections. The use of multiple sources aimed at both covering more relationships than any single resource, as well as identifying connections with multiple supporting sources. Protein-protein interactions (PPIs) were gathered from the StringDB database (V12.0), filtered so as to keep the top 10% of all interactions after sorting on the combined score, and dropping those reported from text-mining only. These were

complemented with interactions reported in the BioGrid database (V4.4.224). This represented a total of 84,363 deduplicated, high-confidence interactions, involving 12,896 unique proteins. The nodes in this protein-protein network were annotated with the logFoldChange values obtained from the differential proteomic analysis upon mTOR-inhibited paused ESCs. As for the miRNA-target edges, protein-protein interactions were scored using the logFoldChange values of the nodes they connect, where we defined the edge score between two proteins as the sum of the logFC of two connected proteins, highlighting the expected co-expression of interacting proteins. This yielded a total of 34,846 protein-protein edges including 4,730 unique proteins with measured logFCs. From these, the top 1% highest-scoring edges were retained and included in each of the different miRNA-target subnetworks, resulting in a multipartite network of the most important regulatory interactions, supposedly representing the core of the dormancy network. Of note, to enhance the clarity of visualization of the resulting networks, we removed protein nodes where the protein had only one connection (miRNA or protein) while not significantly down-regulated.

miRNA loss-of-function in blastocysts via miRNA inhibitor injections

Inhibitors (antimiRs) against miR26b-5p and miR200a/b/c-3p were purchased from Qiagen (339130 , 339160 respectively). AntimiRs in injection media (1mM Tris-HCL pH 7.5 and 0.5mM EDTA in embryo grade water) were injected into each cell of 2-cell-stage embryos (BL/6xCast hybrid) using Leica DMIRB inverted microscope, Narishige MMO micromanipulators/microinjectors, Eppendorf Celltram 4r microinjector and Eppendorf FemtoJet microinjector. Embryos were then transferred to fresh KSOM+AA media (Sigma, MR-101) and cultured until the early blastocyst stage. Blastocysts were split into two groups and treated either with DMSO or 200 nM RapaLink-1. As a negative control, a non-targeting inhibitor (Qiagen, 339136) with no sequence hits of >70% homology to any organism in the NCBI and miRBase databases was used. The survival rate and duration of embryos in mTORi-induced pausing were scored.

miR-92 overexpression

Pre-miR sequences of miR-92a and miR-92b were PCR amplified and cloned into pLKO.1-puro lentiviral vector between AgeI and EcoRI restriction sites. Virus production and transduction were done using standard protocols. In brief, 4ug of lentiviral plasmids were packaged with equal parts of viral packaging vectors (pVSV-G, pMDL, pRSV) by transfecting them in HEK 293T cells. Virus production was carried out for 72 hours. The final precipitated virus was then suspended in 200ul ice-cold PBS. 30ul of viral suspension was then used to infect 100,000 mESCs in single-cell suspension for 1 hour at 37C. After this, the infected mES cells were seeded onto a 6-well culture plate. The media was changed the next day. Puromycin selection was done 48h after infection and overexpression of respective microRNAs was assessed by miRNA qPCR using Taqman probes against miR-92a-5p and 3p; miR-92b-5p and 3p ; miR-290a-3p (positive control). The relative microRNA expression was calculated against the eIF1alpha housekeeping gene.

Immunofluorescence (IF)

Mouse ESCs: Cells were cultured on glass coverslips and were fixed in 4% PFA for 10 min at room temperature, washed once in PBS, and then permeabilized with 0.2% Triton-X100 in PBS for 5 min on ice. After washing once in PBS-T (PBS with 0.2% Tween-20), cells were blocked with blocking buffer (PBS-T, 2% BSA, and 5% goat serum (Jackson Immunoresearch/Dianova, 017-000-121) for 1 hour at room temperature. Cells were then stained with primary antibodies: PML, SC-35, DDX-6, NPM-1 overnight at 4C. The cells were washed thrice with wash buffer (PBS-T, 2% BSA) for 10 min. Anti-mouse 488 or anti-rabbit 568 secondary antibody conjugated with Alexa Fluor was added to cells at a dilution of 1:700 in blocking buffer and incubated for 1 hour at room temperature, followed by 3 washes with wash buffer for 10 min. The coverslips were then mounted with Vectashield with DAPI (Vector labs, H-2000) and sealed with nail polish. Imaging was done using a Zeiss LSM880 Airy microscope using Airy scan mode and image processing was done using Zen black and Zen Blue software (version 2.3). Image quantification was done using CellProfiler (version 4.2.1) where nuclei or cells that were denoted as primary objects were identified and the normalized intensities of the respective protein stained were measured against nuclear or cell area (https://cellprofiler.org/). Data were plotted using GraphPad Prism (version 9).

Mouse Embryos: Embryos were fixed for 10 minutes in 4% PFA, then permeabilized for 15 minutes in 0.2% Triton X-100 (Sigma, T8787) in PBS. Permeabilized embryos were incubated in blocking buffer (0.2% Triton X-100 in PBS + 2% BSA Fraction V 7.5% (Thermo Fisher Scientific, 15260-037) + 5% goat serum (Jackson Immunoresearch/Dianova, 017-000-121) for 1h. Then embryos were incubated overnight at 4C with the CDX-2 and NANOG primary antibodies. Primary antibodies were diluted in blocking buffer, Prior to incubation with the secondary antibodies, embryos were washed three times in washing buffer (0.2% Triton X-100 in PBS + 2% BSA). Then, the embryos were incubated with the secondary antibodies for 1h at room temperature. The donkey anti-mouse Alexa Fluor 680 and donkey anti-rabbit Alexa Fluor 568 antibodies were diluted 1:200 in blocking buffer. After incubation with the secondary antibody, embryos were washed three times in washing buffer. Then, embryos were mounted on a microscope slide with a Secure-Seal™ Spacer (8 wells, 9 mm diameter, 0.12 mm deep, Thermo Fisher Scientific, S24737), covered with a cover glass, and sealed with nail polish.
Imaging was done using a Zeiss LSM880 Airy microscope using Airy scan mode and image processing was done using Zen black and Zen Blue software (version 2.3). Image quantification was done using CellProfiler[66] (version 4.2.1) where nuclei or cells that were denoted as primary objects and the normalized intensities of the respective protein stained were measured against nuclear or cell area (https://cellprofiler.org/). Data were plotted using GraphPad Prism (version 9).

Human PSCs: Cells were cultured on glass coverslips and were fixed in 4% PFA for 10 min at room temperature, washed once in PBS, then permeabilized with 0.2% Triton-X100 in PBS for 5 min on ice. After washing once in PBS-T (PBS with 0.2% Tween-20), cells were blocked with blocking buffer (PBS-T, 2% BSA and 5% goat serum (Jakson Immunoresearch/Dianova, 017-000-121) for 1 hour at room temperature. Cells were then stained with primary antibodies pS6 (CST Cat no: 4858) 1:200, pAKT (CST, 4060T) 1:200, KI67 (BD Pharmingen, 556003)

1:400, H3 phosphoS10 (Abcam, ab5176), 1:1000, OCT4 (Santa Cruz, sc5279) 1:50, NANOG (Abcam, ab109250) 1:200, γH2A.X (Biolegend, 613405) 1:400 overnight at 4°C. The cells were washed thrice with wash buffer (PBS-T, 2% BSA) for 10 min. Anti-rabbit (Thermo, A10042) or anti-mouse (Thermo, 21202) secondary antibody conjugated with Alexa Fluor was added to cells at a dilution of 1:700 in blocking buffer and incubated for 1 hour at room temperature, followed by 3 washes with wash buffer for 10 min. The coverslips were then mounted with Vectashield with DAPI (Vector labs, H-2000) and sealed with nail polish. Imaging was done using a Zeiss LSM880 Airy microscope using Airy scan mode and image processing was done using Zen black and Zen blue software (version 2.3). Image quantification was done using CellProfiler (version 4.2.1) where nuclei or cells which were denoted as primary objects were identified and the normalized intensities of the respective protein stained were measured against nuclear or cell area(https://cellprofiler.org/). Data were plotted using GraphPad Prism (version 9).

Human Embryos: Human embryos were fixed in 4% paraformaldehyde in PBS for 1h at 4°C, and mouse embryos 10 min at room temperature. Embryos were washed once in PBS, then permeabilized with 1× PBS with 0.5% Triton X-100 and then blocked in blocking solution (10% FBS in 1× PBS with 0.1% Triton X-100) for 1-2h at room temperature on a rotating shaker. Embryos were then incubated with primary antibodies diluted in blocking solution overnight at 4 °C on rotating shaker. The following day, embryos were washed once in 1× PBS with 0.1% Triton X-100 at room temperature on a rotating shaker, and then incubated with secondary antibodies diluted in blocking solution for 1 h at room temperature on a rotating shaker in the dark. Embryos were washed in 1× PBS with 0.1% Triton X-100 and counterstained with DAPI. The following antibodies and dilutions were used: anti-pS6 (Cell Signaling, 4858) 1:250, anti-OCT4 (Santa Cruz, 5279) 1:500, anti-Nanog (R&D AF1997) 1:200, anti-CDX2 (BioGenex, MU392-UC) 1:100, anti-pAKT (CST 4060T) 1:100, anti-4EBP1 (CST 2855) 1:100, anti-Lamin B1 (Abcam ab16048) 1:100, and anti-GATA3 (R&D AF2605) 1:200. All secondary antibodies were Alexa Fluor (Life Technologies), raised in donkey and used 1:200 to 1:1000. For imaging, embryos were placed on a µ-Slide 18 Well Flat dish (Ibidi, 81826) in PBS and imaged on a Leica Sp8 confocal with a Leica HCX PL APO 63x / 1.3 GLYC CORR CS objective. The z-stack step is 3.5-5 µm.

Human Blastoids: Blastoids were collected using mouth pipette and transferred to U-bottomed 96-well plates (Merck, BR701330). Once the structures had settled, the medium was washed twice with PBS and fixed with 4% PFA for 30 min at room temperature, followed by three 10 min washes with PBS. PBS containing 10% normal donkey serum and 0.3% Triton X-100 was used for blocking and permeabilization for 3h at room temperature. The primary antibody was incubated at 4 °C in blocking/permeabilization solution with gentle shaking and washed at least three times with PBS containing 0.1% Triton X-100 for 10 min. The secondary antibody was diluted in PBS containing 0.1% Triton X-100 and incubated at room temperature in the dark for 1 h. Then, the blastoids were washed three times with PBS containing 0.1% Triton X-100 for 10 min and prepared for imaging. For imaging, the blastoids were placed in a glass-bottomed plates. Confocal IF images of blastoids were acquired with an Olympus IX83

microscope with Yokogawa W1 spinning disk (Software: CellSense 2.3; camera: Hamamatsu Orca Flash 4.0). The confocal images were analyzed, and display images were exported using FIJI 1.53k or Bitplane IMARIS 9.7.0 software. For cell counting, Bitplane IMARIS software was used. Cell count parameters were set for size and fluorescence strength of voxels and then overall cell count data was obtained for each image using the IMARIS spot function.

Transcription Factor Binding Site (TFBS) mining at candidate miRNA promoters

To identify potential transcription factors regulating the set of concordant up-regulated miRNAs, we performed a motif search over the promoter sequences of these miRNAs. Promoters were taken from the work of de Rie et al. 2017[175], totaling 1,468 promoter regions (lifted over to mm10 genome assembly), each associated to one miRNA. Overlapping regions were merged, resulting in 641 sequences. Larger regions were then identified by extending from the 3' end by 1,500 nucleotides upstream and 500 nucleotides downstream. Motifs of transcription factors were obtained from the JASPAR database[176], taking the set of 841 vertebrates non-redundant position frequency matrices. The Matrix-Scan tool from RSAT[177] was applied to scan the sequences, requiring a maximum p-value per site of 0.1. Background frequencies were calculated from the input set of sequences (markov=1, bg_pseudo=0.01). This scan resulted in a total of 5,389,949 motif hits across the 641 promoter sequences. Hits were further filtered on their sequence-matching score, so as to keep for each transcription factor hits above the median hit-score, resulting in a total subset of 453,101 motif hits. Finally, for each transcription factor, a Fisher test was applied to assess whether that TF exhibited enriched binding sites (relative to other TFs) within the promoter sequences of the up-regulated miRNAs (N=14), compared to a background set of promoter sequences corresponding to all other expressed miRNAs (N=91) A total of 215 TFBS motifs presented an odds-ratio greater than 1, indicating a relatively greater proportion of candidate promoters with a motif hit over other promoters. Filtering for odds-ratio greater than 2 and raw P-value lower than 0.1 yielded the set of 16 transcription factors whose binding sites are enriched among the concordant up-regulated miRNAs and that therefore represent potential regulators of dormancy.

CUT&Tag

Sample preparation: Frozen nuclei were used and CUT&Tag was performed as described previously[178] with minor modifications. Cells were dissociated using accutase and washed in PBS. Nuclei were extracted by resuspending the cells in ice-cold NE1 buffer (20 mM HEPES-KOH, pH7.5, 10 mM KCl, 0.5 mM Spermidine, 0.1% Triton X-100, 20% glycerol, 1 mM PMSF, 5 mM NaF, 1 mM Na3VO4) and incubating on ice for 10 min. Nuclei were fixed by incubating with 0.1% formaldehyde at room temperature for 2 min. 1.25 M glycine was added to stop cross-linking. Fixed nuclei were centrifuged for 4 minutes at 1300g at 4°C and were frozen in Wash buffer (20 mM HEPES-KOH, pH 7.5, 150 mM NaCl, 0.5 mM Spermidine, 1 mM PMSF, 5 mM NaF, 1 mM Na3VO4) with 10% DMSO at -80°C until further processing. For each CUT&Tag reaction, 3.5 µl of Concanavalin A beads (Bangs Laboratories) were equilibrated by washing 2 times in 100 µl Binding buffer (20 mM HEPES-KOH, pH 7.5, 10 mM KCl, 1 mM CaCl2, 1 mM MnCl2) and concentrated again in 3.5 µl Binding buffer. 10,000 cryopreserved nuclei were thawed and bound to the Concanavalin A beads by incubating for 10 min with rotation at room temperature. The beads were separated on a magnet and

resuspended in 25 µl of cold Antibody buffer (Wash buffer with 0.1% BSA) containing respective primary antibody or IgG (TFE3, Sigma HPA023881, 1:50; IgG, Abcam ab46540, 1:100). Primary antibody incubation was done by incubating the beads at 4 °C with gentle nutation overnight. The beads were separated from the primary antibody on a magnet, resuspended in 25 µl of Wash buffer containing matching secondary antibody (guinea pig α-rabbit antibody, ABIN101961, Antibodies online, 1:100) and were incubated for 30 min at room temperature with gentle nutation. Afterwards, the beads were separated from the secondary antibody and washed once in 200µl of Wash buffer while being kept on the magnet. Homemade 3xFLAG-pA-Tn5, preloaded with Mosaic-end adapters, was diluted 1:250 in wash buffer and 25 µl of it was used to resuspend the beads. The beads were incubated for 1h at room temperature with gentle nutation and were washed once in 200 µl wash buffer. Tagmentation was performed by incubating the beads in 50 µl Tagmentation buffer (10mM MgCl2 in wash buffer) for 1h at 37°C. Tagmentation was stopped by adding 2.25 µl of 500 mM EDTA and 2.75 µl of 10% SDS to the beads followed by adding 0.5 µl of Proteinase K (20 mg/ml). After vortexing for 5 sec, the beads were incubated at 55 °C for 1h to solubilize the DNA fragments and then at 70 °C for 30 min to inactivate the Proteinase K. The beads were removed on the magnet and the DNA was purified using Chimmun DNA Clean & Concentrator (D5205, Zymo Research) following the manufacturer's manual. The final CUT&Tag DNA was eluted in 25 µl of elution buffer. To amplify the NGS libraries, 25 µl of NEBNext HiFi 2x PCR Master Mix (New England BioLabs) was mixed with 21 µl of the CUT&Tag DNA, 2µl of 10 µM i5- and 2µl of 10 µM i7- unique barcoded primers and the following program was run on a thermocycler: 72 °C for 5 min, 98 °C for 30 sec, 98 °C for 10 sec, 63 °C for 10 sec (14 cycles of step 3-4) and 72 °C for 1 min. Ampure XP beads (Beckman Coulter) were used for post-PCR cleanup. 55 µl (1.1x volume) of the Ampure XP beads were added to the PCR mix and incubated for 10 minutes at room temperature. The beads were separated and washed two times using 80% ethanol on a magnet. Finally, the CUT&Tag libraries were eluted in 25 µl of Tris-HCl, pH 8.0. The quality of the CUT&Tag libraries was assessed by Agilent High Sensitivity D5000 ScreenTape System and QubitTM dsDNA HS Assay (Invitrogen). Sequencing libraries were pooled in equimolar ratios. The libraries were sequenced on Illumina next next-generation sequencer in paired-end mode at 5-8 million fragments per library.

Analysis: Raw reads were subjected to adapter and quality trimming with cutadapt (version 2.4; parameters: --quality-cutoff 20 --overlap 5 --minimum-length 25 --adapter AGA TCGGAAGAGC -A AGA TCGGAAGAGC) as were their respective input samples. Reads were aligned to the mouse genome (mm10) using BWA with the 'mem' command (version 0.7.17, default parameters). A sorted BAM file was obtained and indexed using samtools with the 'sort' and 'index' commands (version 1.10). Duplicate reads were identified and removed using GATK (version 4.1.4.1) 'MarkDuplicates' and default parameters. After careful inspection and validation of high correlation, replicates of treatment and input samples were merged respectively using samtools 'merge'.

The smoothed Counts Per Million (CPM) signal was aggregated over extended promoter regions (upstream : 1,500 nt, downstream : 500 nt) by taking the maximum value over the regions and scaling those by the 95th quantile value across promoters for each condition. To further quantify the increased or decreased signal in paused over control samples, the log2 ratio of these maximum values was calculated, yielding for each promoter a positive value for

relative increase signal, or a negative value for relative decrease. Finally, a one-sided Mann-Withney U test was performed to evaluate whether promoters of candidate miRNAs presented a greater increase in signal in paused samples, as compared to promoters of other measured miRNAs with available signal (N=88 from the previous 91 promoters).

Nascent RNA expression analysis

25,000 wild-type or D*gcr8* KO cells in normal or mTORi conditions were plated onto 0.1% gelatin-coated glass coverslips. EU staining was performed using Click-iT RNA imaging kit (Invitrogen, C10329) following the manufacturer's protocol. The coverslips were then mounted with Vectashield (Vector labs, H-1000) and sealed with nail polish. Imaging was done using a Zeiss LSM880 Airy microscope using Airy scan mode and image processing was done using Zen black and Zen Blue software (version 2.3). Image quantification was done using CellProfiler (version 4.2.1) where nuclei that were denoted as primary objects were identified and the normalized intensities of the EU staining were measured against the nuclear area (https://cellprofiler.org/). Data were plotted using GraphPad Prism (version 9).

Differential gene expression analysis

Transcript abundance estimations per sample were obtained with kallisto[179] and imported to R with the Bioconductor package tximport[180]. tximport summarizes transcript level abundance estimates for gene-level analysis. Differential gene expression was performed with the Bioconductor package DESeq2. Differentially expressed genes between WT paused vs normal and *Dgcr8* KO paused vs normal was defined as those with an adjusted p-value of 0.05 or smaller and |log2FC|>1.

Differential isoform usage analysis

Abundance estimates per sample were obtained with kallisto. The R Bioconductor package IsoformSwitchAnalyzeR[181] was used for differential isoform usage (DIU) analysis. Identification of differentially used isoforms across all genes with IsoformSwitchAnalyzeR is done through DEXseq[74], which is a statistical method originally developed for differential exon usage based on the likelihood ratio test that has since been shown to adequately control for false discovery rate (FDR) in the setting of DIU.

Sashimi plots

Reads were aligned to the mouse genome (build GRCm38/mm10) using STAR[182] with default settings. Sashimi plots were done using ggsashimi[183]. Only differentially used transcripts were used for plotting.

Western Blot (WB)

Cells were lysed with RIPA buffer supplemented with protease inhibitor cocktail for 30 min at 4C. The cells were spun at 14000 rcf for 20 min at 4C and the supernatant was collected for BCA protein quantification. 50 µg of protein was loaded onto a gradient gel (Biorad, 4561083) and the run was performed at 75V for 2.5h. Proteins were transferred to PVDF membrane (Invitrogen, IB24002) and blocking was done with 5% non-fat milk for 1h at room temperature. MBD2 or GAPDH primary antibodies were diluted in non-fat milk (1:1000) and incubated at

4C overnight. The blots were washed thrice in PBST for 10 minutes. The blots were then incubated with secondary antibody diluted 1:2000 and incubated for 1h at room temperature. The blots were washed thrice in PBST for 10 minutes each. Protein detection was done using SuperSignal West Dura on Biorad ChemiDoc MP Imaging System.

siRNA-mediated knockdown of Raptor and Rictor

65,000 cells were plated on a 6-well dish. On the second day after plating, when the cells are approximately 40-50% confluent, cells were transfected with siRNAs (Dharmacon, siGenome) using the FuGene reagent (Promega, E2311). The following siRNA concentrations were used: Rictor: 100 nM (M-016984-02-0005), Raptor: 500nM (M-004107-01-0005), control: 100nM/500nM (D-001206-14-05). After transfection, the cells were grown for three days, after which cells were plated for proliferation assays, western blot and immunofluorescence.

Apoptosis assay

Cells adherent to the plate as well as floating cells were collected for the apoptosis assay. Cells were dissociated using TrypLE, washed in cold PBS, and resuspended in Annexin binding buffer (10 mM HEPES, 140 mM NaCl and 2.5 mM $CaCl_2$, pH 7.4). Cell density was adjusted to 400,000 cells in 500 µl Annexin binding buffer. Staining for Annexin V was done according to manufacturer's instructions (Thermo Fisher, R37174) along with dead cell stain using SYTOX AADvanced (Thermo, S10274) for 15 min at room temperature. A FACS AriaFusion flow cell cytometer was used to analyze cell staining. Data were analyzed using FlowJo (version 10) and plotted using GraphPad Prism (version 9).

Cell cycle assay

To study cell cycle distribution, the Click-iT EdU Alexa Fluor 488 Flow Cytometry Assay kit (Thermo Fisher, C10425) was used. Normal and paused iPSCs were incubated at 37°C for 2 hours with 10 µM EdU in 5% O_2, 5% CO_2. Cells were then harvested, washed once with 3 ml of 1% BSA in PBS, centrifuged at 300 g for 5 min and the supernatant was removed. The pellet was dislodged and fixed in 100µl Click-iT fixative for 15 minutes at room temperature. After fixation, cells were washed with 3 ml of 1% BSA in PBS. The pellet was then resuspended in 100 µl1x Click-iT saponin-based permeabilization and wash reagent and incubated for 15 minutes at room temperature. To this, 500 µl Click-iT reaction cocktail was added and incubated for 30 minutes in the dark at room temperature. After incubation, cells were washed with 3 ml of 1X Click-iT saponin based permeabilization and wash reagent, suspended in 200 ul of the same reagent. FxCycle violet (Life Technologies, F10347) was added to a final concentration of 1 µg/ml to measure DNA content and incubated for 1 hour at room temperature in the dark. FACS AriaFusion cell cytometer was used to acquire data using BD FACSDIVA Software v8.0.1. Data were analyzed using FlowJo (version 10) and plotted using GraphPad Prism (version 9).

List of publications

1. **Dhanur P. Iyer***, Heidar Heidari Khoei*, Vera A. van der Weijden, Afshan McCarthy, Teresa Rayon, Claire S. Simon, Ilona Dunkel, Sissy E. Wamaitha, Maria Stecklum, Anja Sterner-Kock, Kay Elder, Phil Snell, Leila Christie, Edda G. Schulz, Kathy K. Niakan, Nicolas Rivron, Aydan Bulut-Karslioglu. **Reversibly developmental pausing of human pluripotent cells and blastoids via mTOR inhibition** ***(in revision, Cell)***
2. **Dhanur P. Iyer*,** Lambert Moyon*, Francisca R. Ringeling, Chieh-Yu Cheng, Lars Wittler, Annalisa Marsico, Aydan Bulut-Karslioglu. **Combinatorial microRNA activity mediates the cellular transition into embryonic dormancy.** ***(under review, Genome Research)***
3. **Dhanur P. Iyer**, Heidar Heidari Khoei, Nicolas Rivron, Aydan Bulut-Karslioglu. **Pressing pause on mouse and human development.** ***(Commissioned protocol manuscript in preparation)***
4. Vera A. van der Weijden, Maximilian Stoetzel, **Dhanur P. Iyer** , Beatrix Fauler, Mohammed Shahraz, David Meierhofer, Steffen Rulands, Theodore Alexandrov, Thorsten Mielke, Aydan Bulut-Karslioglu. **Metabolic enhancement of developmental pausing.** ***(accepted, Nature Cell Biology 2023)***

Bibliography

1. Zhu, M. & Zernicka-Goetz, M. Principles of Self-Organization of the Mammalian Embryo. *Cell* **183**, 1467–1478 (2020).
2. Tarkowski, A. K. Experiments on the Development of Isolated Blastomeres of Mouse Eggs. *Nature* **184**, 1286–1287 (1959).
3. Borsos, M. & Torres-Padilla, M.-E. Building up the nucleus: nuclear organization in the establishment of totipotency and pluripotency during mammalian development. *Genes Dev.* **30**, 611–621 (2016).
4. Mihajlović, A. I. & Bruce, A. W. The first cell-fate decision of mouse preimplantation embryo development: integrating cell position and polarity. *Open Biol.* **7**, 170210 (2017).
5. Pauken, C. M. & Capco, D. G. The Expression and Stage-Specific Localization of Protein Kinase C Isotypes during Mouse Preimplantation Development. *Dev. Biol.* **223**, 411–421 (2000).
6. Vinot, S. *et al.* Asymmetric distribution of PAR proteins in the mouse embryo begins at the 8-cell stage during compaction. *Dev. Biol.* **282**, 307–319 (2005).
7. Plusa, B. *et al.* Downregulation of Par3 and aPKC function directs cells towards the ICM in the preimplantation mouse embryo. *J. Cell Sci.* **118**, 505–515 (2005).
8. Humięcka, M., Szpila, M., Kłoś, P., Maleszewski, M. & Szczepańska, K. Mouse blastomeres acquire ability to divide asymmetrically before compaction. *PLOS ONE* **12**, e0175032 (2017).
9. Wu, S., Liu, Y., Zheng, Y., Dong, J. & Pan, D. The TEAD/TEF Family Protein Scalloped Mediates Transcriptional Output of the Hippo Growth-Regulatory Pathway. *Dev. Cell* **14**, 388–398 (2008).

10. Zhang, L. *et al.* The TEAD/TEF Family of Transcription Factor Scalloped Mediates Hippo Signaling in Organ Size Control. *Dev. Cell* **14**, 377–387 (2008).
11. Zhao, B. *et al.* TEAD mediates YAP-dependent gene induction and growth control. *Genes Dev.* **22**, 1962–1971 (2008).
12. Goulev, Y. *et al.* SCALLOPED Interacts with YORKIE, the Nuclear Effector of the Hippo Tumor-Suppressor Pathway in Drosophila. *Curr. Biol.* **18**, 435–441 (2008).
13. Nishioka, N. *et al.* The Hippo Signaling Pathway Components Lats and Yap Pattern Tead4 Activity to Distinguish Mouse Trophectoderm from Inner Cell Mass. *Dev. Cell* **16**, 398–410 (2009).
14. Dietrich, J.-E. & Hiiragi, T. Stochastic patterning in the mouse pre-implantation embryo. *Development* **134**, 4219–4231 (2007).
15. Niwa, H. *et al.* Interaction between Oct3/4 and Cdx2 Determines Trophectoderm Differentiation. *Cell* **123**, 917–929 (2005).
16. Strumpf, D. *et al.* Cdx2 is required for correct cell fate specification and differentiation of trophectoderm in the mouse blastocyst. *Development* **132**, 2093–2102 (2005).
17. VerMilyea, M. D., O'Neill, L. P. & Turner, B. M. Transcription-Independent Heritability of Induced Histone Modifications in the Mouse Preimplantation Embryo. *PLoS ONE* **4**, e6086 (2009).
18. Torres-Padilla, M.-E., Parfitt, D.-E., Kouzarides, T. & Zernicka-Goetz, M. Histone arginine methylation regulates pluripotency in the early mouse embryo. *Nature* **445**, 214–218 (2007).
19. Parfitt, D.-E. & Zernicka-Goetz, M. Epigenetic Modification Affecting Expression of Cell Polarity and Cell Fate Genes to Regulate Lineage Specification in the Early Mouse Embryo. *Mol. Biol. Cell* **21**, 2649–2660 (2010).

20. Ohnishi, Y. *et al.* Cell-to-cell expression variability followed by signal reinforcement progressively segregates early mouse lineages. *Nat. Cell Biol.* **16**, 27–37 (2014).

21. Arman, E., Haffner-Krausz, R., Chen, Y., Heath, J. K. & Lonai, P. Targeted disruption of fibroblast growth factor (FGF) receptor 2 suggests a role for FGF signaling in pregastrulation mammalian development. *Proc. Natl. Acad. Sci.* **95**, 5082–5087 (1998).

22. Rappolee, D. A., Basilico, C., Patel, Y. & Werb, Z. Expression and function of FGF-4 in peri-implantation development in mouse embryos. *Development* **120**, 2259–2269 (1994).

23. Feldman, B., Poueymirou, W., Papaioannou, V. E., DeChiara, T. M. & Goldfarb, M. Requirement of FGF-4 for Postimplantation Mouse Development. *Science* **267**, 246–249 (1995).

24. Cheng, A. M. *et al.* Mammalian Grb2 Regulates Multiple Steps in Embryonic Development and Malignant Transformation. *Cell* **95**, 793–803 (1998).

25. Kang, M., Piliszek, A., Artus, J. & Hadjantonakis, A.-K. FGF4 is required for lineage restriction and salt-and-pepper distribution of primitive endoderm factors but not their initial expression in the mouse. *Development* **140**, 267–279 (2013).

26. Tang, F. *et al.* Tracing the Derivation of Embryonic Stem Cells from the Inner Cell Mass by Single-Cell RNA-Seq Analysis. *Cell Stem Cell* **6**, 468–478 (2010).

27. Morris, S. A. *et al.* Origin and formation of the first two distinct cell types of the inner cell mass in the mouse embryo. *Proc. Natl. Acad. Sci.* **107**, 6364–6369 (2010).

28. Yamanaka, Y., Lanner, F. & Rossant, J. FGF signal-dependent segregation of primitive endoderm and epiblast in the mouse blastocyst. *Development* **137**, 715–724 (2010).

29. Guo, G. *et al.* Resolution of Cell Fate Decisions Revealed by Single-Cell Gene Expression Analysis from Zygote to Blastocyst. *Dev. Cell* **18**, 675–685 (2010).

30. Yang, D.-H. *et al.* Disabled-2 Is Essential for Endodermal Cell Positioning and Structure Formation during Mouse Embryogenesis. *Dev. Biol.* **251**, 27–44 (2002).

31. Gerbe, F., Cox, B., Rossant, J. & Chazaud, C. Dynamic expression of Lrp2 pathway members reveals progressive epithelial differentiation of primitive endoderm in mouse blastocyst. *Dev. Biol.* **313**, 594–602 (2008).

32. Kemp, C., Willems, E., Abdo, S., Lambiv, L. & Leyns, L. Expression of all Wnt genes and their secreted antagonists during mouse blastocyst and postimplantation development. *Dev. Dyn.* **233**, 1064–1075 (2005).

33. Meilhac, S. M. *et al.* Active cell movements coupled to positional induction are involved in lineage segregation in the mouse blastocyst. *Dev. Biol.* **331**, 210–221 (2009).

34. Schulz, K. N. & Harrison, M. M. Mechanisms regulating zygotic genome activation. *Nat. Rev. Genet.* **20**, 221–234 (2019).

35. Braude, P., Bolton, V. & Moore, S. Human gene expression first occurs between the four- and eight-cell stages of preimplantation development. *Nature* **332**, 459–461 (1988).

36. Casser, E. *et al.* Totipotency segregates between the sister blastomeres of two-cell stage mouse embryos. *Sci. Rep.* **7**, 8299 (2017).

37. Gardner, D. K., Phil, D., Lane, M. & Schoolcraft, W. B. Noninvasive assessment of human embryo nutrient consumption as a measure of developmental potential. **76**, (2001).

38. Piotrowska, K., Wianny, F., Pedersen, R. A. & Zernicka-Goetz, M. Blastomeres arising from the first cleavage division have distinguishable fates in normal mouse development. *Development* **128**, 3739–3748 (2001).

39. Piotrowska-Nitsche, K., Perea-Gomez, A., Haraguchi, S. & Zernicka-Goetz, M. Four-cell stage mouse blastomeres have different developmental properties. *Development* **132**, 479–490 (2005).

40. Nikas, G., Ao, A., Winston, R. M. L. & Handyside, A. H. Compaction and Surface Polarity in the Human Embryo in Vitro. *Biol. Reprod.* **55**, 32–37 (1996).

41. Fogarty, N. M. E. *et al.* Genome editing reveals a role for OCT4 in human embryogenesis. *Nature* **550**, 67–73 (2017).

42. Niakan, K. K. & Eggan, K. Analysis of human embryos from zygote to blastocyst reveals distinct gene expression patterns relative to the mouse. *Dev. Biol.* **375**, 54–64 (2013).

43. Petropoulos, S. *et al.* Single-Cell RNA-Seq Reveals Lineage and X Chromosome Dynamics in Human Preimplantation Embryos. *Cell* **165**, 1012–1026 (2016).

44. Kuijk, E. W. *et al.* The roles of FGF and MAP kinase signaling in the segregation of the epiblast and hypoblast cell lineages in bovine and human embryos. *Development* **139**, 871–882 (2012).

45. Roode, M. *et al.* Human hypoblast formation is not dependent on FGF signalling. *Dev. Biol.* **361**, 358–363 (2012).

46. Mobley, R. J. *et al.* MAP3K4 Controls the Chromatin Modifier HDAC6 during Trophoblast Stem Cell Epithelial-to-Mesenchymal Transition. *Cell Rep.* **18**, 2387–2400 (2017).

47. Rock, J. & Hertig, A. T. The human conceptus during the first two weeks of gestation. *Am. J. Obstet. Gynecol.* **55**, 6–17 (1948).

48. Lindenberg, S., Hyttel, P., Sjøgren, A. & Greve, T. A comparative study of attachment of human, bovine and mouse blastocysts to uterine epithelial monolayer. *Hum. Reprod.* **4**, 446–456 (1989).

49. Aplin, J. D. & Ruane, P. T. Embryo–epithelium interactions during implantation at a glance. *J. Cell Sci.* **130**, 15–22 (2017).

50. Weimar, C. H. E., Post Uiterweer, E. D., Teklenburg, G., Heijnen, C. J. & Macklon, N. S. In-vitro model systems for the study of human embryo–endometrium interactions. *Reprod. Biomed. Online* **27**, 461–476 (2013).

51. Christodoulou, N. *et al.* Morphogenesis of extra-embryonic tissues directs the remodelling of the mouse embryo at implantation. *Nat. Commun.* **10**, 3557 (2019).

52. Nichols, J. & Smith, A. Naive and Primed Pluripotent States. *Cell Stem Cell* **4**, 487–492 (2009).

53. Bedzhov, I. & Zernicka-Goetz, M. Self-Organizing Properties of Mouse Pluripotent Cells Initiate Morphogenesis upon Implantation. *Cell* **156**, 1032–1044 (2014).

54. Shahbazi, M. N. *et al.* Pluripotent state transitions coordinate morphogenesis in mouse and human embryos. *Nature* **552**, 239–243 (2017).

55. Christodoulou, N. *et al.* Sequential formation and resolution of multiple rosettes drive embryo remodelling after implantation. *Nat. Cell Biol.* **20**, 1278–1289 (2018).

56. Mossahebi-Mohammadi, M., Quan, M., Zhang, J.-S. & Li, X. FGF Signaling Pathway: A Key Regulator of Stem Cell Pluripotency. *Front. Cell Dev. Biol.* **8**, 79 (2020).

57. Kagawa, H. *et al.* Human blastoids model blastocyst development and implantation. *Nature* **601**, 600–605 (2022).

58. Amadei, G. *et al.* Inducible Stem-Cell-Derived Embryos Capture Mouse Morphogenetic Events In Vitro. *Dev. Cell* **56**, 366-382.e9 (2021).

59. Arias, A. M., Marikawa, Y. & Moris, N. Gastruloids: Pluripotent stem cell models of mammalian gastrulation and embryo engineering. *Dev. Biol.* **488**, 35–46 (2022).

60. Xu, P.-F. *et al.* Construction of a mammalian embryo model from stem cells organized by a morphogen signalling centre. *Nat. Commun.* **12**, 3277 (2021).

61. Veenvliet, J. V. *et al.* Mouse embryonic stem cells self-organize into trunk-like structures with neural tube and somites. *Science* **370**, eaba4937 (2020).

62. Kim, D.-H. *et al.* mTOR Interacts with Raptor to Form a Nutrient-Sensitive Complex that Signals to the Cell Growth Machinery. *Cell* **110**, 163–175 (2002).

63. Hara, K. *et al.* Raptor, a Binding Partner of Target of Rapamycin (TOR), Mediates TOR Action. *Cell* **110**, 177–189 (2002).

64. Yang, H. *et al.* mTOR kinase structure, mechanism and regulation. *Nature* **497**, 217–223 (2013).

65. Sancak, Y. *et al.* PRAS40 Is an Insulin-Regulated Inhibitor of the mTORC1 Protein Kinase. *Mol. Cell* **25**, 903–915 (2007).

66. Haar, E. V., Lee, S., Bandhakavi, S., Griffin, T. J. & Kim, D.-H. Insulin signalling to mTOR mediated by the Akt/PKB substrate PRAS40. *Nat. Cell Biol.* **9**, 316–323 (2007).

67. Wang, L., Harris, T. E., Roth, R. A. & Lawrence, J. C. PRAS40 Regulates mTORC1 Kinase Activity by Functioning as a Direct Inhibitor of Substrate Binding. *J. Biol. Chem.* **282**, 20036–20044 (2007).

68. Peterson, T. R. *et al.* DEPTOR Is an mTOR Inhibitor Frequently Overexpressed in Multiple Myeloma Cells and Required for Their Survival. *Cell* **137**, 873–886 (2009).

69. Frias, M. A. *et al.* mSin1 Is Necessary for Akt/PKB Phosphorylation, and Its Isoforms Define Three Distinct mTORC2s. *Curr. Biol.* **16**, 1865–1870 (2006).

70. Jacinto, E. *et al.* SIN1/MIP1 Maintains rictor-mTOR Complex Integrity and Regulates Akt Phosphorylation and Substrate Specificity. *Cell* **127**, 125–137 (2006).

71. Yang, Q., Inoki, K., Ikenoue, T. & Guan, K.-L. Identification of Sin1 as an essential TORC2 component required for complex formation and kinase activity. *Genes Dev.* **20**, 2820–2832 (2006).

72. Pearce, L. R. *et al.* Identification of Protor as a novel Rictor-binding component of mTOR complex-2. *Biochem. J.* **405**, 513–522 (2007).

73. Dorrello, N. V. *et al.* S6K1- and ßTRCP-Mediated Degradation of PDCD4 Promotes Protein Translation and Cell Growth. *Science* **314**, 467–471 (2006).

74. Brunn, G. J. *et al.* Phosphorylation of the Translational Repressor PHAS-I by the Mammalian Target of Rapamycin. *Science* **277**, 99–101 (1997).

75. Gingras, A.-C. *et al.* Regulation of 4E-BP1 phosphorylation: a novel two-step mechanism. *Genes Dev.* **13**, 1422–1437 (1999).

76. Düvel, K. *et al.* Activation of a Metabolic Gene Regulatory Network Downstream of mTOR Complex 1. *Mol. Cell* **39**, 171–183 (2010).

77. Ben-Sahra, I., Hoxhaj, G., Ricoult, S. J. H., Asara, J. M. & Manning, B. D. mTORC1 induces purine synthesis through control of the mitochondrial tetrahydrofolate cycle. *Science* **351**, 728–733 (2016).

78. Robitaille, A. M. *et al.* Quantitative Phosphoproteomics Reveal mTORC1 Activates de Novo Pyrimidine Synthesis. *Science* **339**, 1320–1323 (2013).

79. Ben-Sahra, I., Howell, J. J., Asara, J. M. & Manning, B. D. Stimulation of de Novo Pyrimidine Synthesis by Growth Signaling Through mTOR and S6K1. *Science* **339**, 1323–1328 (2013).

80. Kim, J., Kundu, M., Viollet, B. & Guan, K.-L. AMPK and mTOR regulate autophagy through direct phosphorylation of Ulk1. *Nat. Cell Biol.* **13**, 132–141 (2011).

81. Martina, J. A., Chen, Y., Gucek, M. & Puertollano, R. MTORC1 functions as a transcriptional regulator of autophagy by preventing nuclear transport of TFEB. *Autophagy* **8**, 903–914 (2012).

82. Roczniak-Ferguson, A. *et al.* The Transcription Factor TFEB Links mTORC1 Signaling to Transcriptional Control of Lysosome Homeostasis. *Sci. Signal.* **5**, (2012).

83. Settembre, C. *et al.* A lysosome-to-nucleus signalling mechanism senses and regulates the lysosome via mTOR and TFEB: Self-regulation of the lysosome via mTOR and TFEB. *EMBO J.* **31**, 1095–1108 (2012).

84. Zhao, J., Zhai, B., Gygi, S. P. & Goldberg, A. L. mTOR inhibition activates overall protein degradation by the ubiquitin proteasome system as well as by autophagy. *Proc. Natl. Acad. Sci.* **112**, 15790–15797 (2015).

85. Rousseau, A. & Bertolotti, A. An evolutionarily conserved pathway controls proteasome homeostasis. *Nature* **536**, 184–189 (2016).

86. Livneh, I. *et al.* Regulation of nucleo-cytosolic 26S proteasome translocation by aromatic amino acids via mTOR is essential for cell survival under stress. *Mol. Cell* **83**, 3333-3346.e5 (2023).

87. Jacinto, E. *et al.* Mammalian TOR complex 2 controls the actin cytoskeleton and is rapamycin insensitive. *Nat. Cell Biol.* **6**, 1122–1128 (2004).

88. Dos D. Sarbassov *et al.* Rictor, a Novel Binding Partner of mTOR, Defines a Rapamycin-Insensitive and Raptor-Independent Pathway that Regulates the Cytoskeleton. *Curr. Biol.* **14**, 1296–1302 (2004).

89. Gan, X. *et al.* PRR5L degradation promotes mTORC2-mediated PKC-δ phosphorylation and cell migration downstream of Gα12. *Nat. Cell Biol.* **14**, 686–696 (2012).

90. Li, X. & Gao, T. mTORC 2 phosphorylates protein kinase Cζ to regulate its stability and activity. *EMBO Rep.* **15**, 191–198 (2014).

91. Thomanetz, V. *et al.* Ablation of the mTORC2 component rictor in brain or Purkinje cells affects size and neuron morphology. *J. Cell Biol.* **201**, 293–308 (2013).

92. García-Martínez, J. M. & Alessi, D. R. mTOR complex 2 (mTORC2) controls hydrophobic motif phosphorylation and activation of serum- and glucocorticoid-induced protein kinase 1 (SGK1). *Biochem. J.* **416**, 375–385 (2008).

93. Dibble, C. C. *et al.* TBC1D7 Is a Third Subunit of the TSC1-TSC2 Complex Upstream of mTORC1. *Mol. Cell* **47**, 535–546 (2012).

94. Inoki, K., Li, Y., Zhu, T., Wu, J. & Guan, K.-L. TSC2 is phosphorylated and inhibited by Akt and suppresses mTOR signalling. *Nat. Cell Biol.* **4**, 648–657 (2002).

95. Manning, B. D., Tee, A. R., Logsdon, M. N., Blenis, J. & Cantley, L. C. Identification of the Tuberous Sclerosis Complex-2 Tumor Suppressor Gene Product Tuberin as a Target of the Phosphoinositide 3-Kinase/Akt Pathway. *Mol. Cell* **10**, 151–162 (2002).

96. Ma, L., Chen, Z., Erdjument-Bromage, H., Tempst, P. & Pandolfi, P. P. Phosphorylation and Functional Inactivation of TSC2 by Erk. *Cell* **121**, 179–193 (2005).

97. Inoki, K. *et al.* TSC2 Integrates Wnt and Energy Signals via a Coordinated Phosphorylation by AMPK and GSK3 to Regulate Cell Growth. *Cell* **126**, 955–968 (2006).

98. Jung, J., Genau, H. M. & Behrends, C. Amino Acid-Dependent mTORC1 Regulation by the Lysosomal Membrane Protein SLC38A9. *Mol. Cell. Biol.* **35**, 2479–2494 (2015).

99. Rebsamen, M. *et al.* SLC38A9 is a component of the lysosomal amino acid sensing machinery that controls mTORC1. *Nature* **519**, 477–481 (2015).

100. Bar-Peled, L. *et al.* A Tumor Suppressor Complex with GAP Activity for the Rag GTPases That Signal Amino Acid Sufficiency to mTORC1. *Science* **340**, 1100–1106 (2013).

101. Wolfson, R. L. *et al.* KICSTOR recruits GATOR1 to the lysosome and is necessary for nutrients to regulate mTORC1. *Nature* **543**, 438–442 (2017).

102. Saxton, R. A. *et al.* Structural basis for leucine sensing by the Sestrin2-mTORC1 pathway. *Science* **351**, 53–58 (2016).

103. Ye, J. *et al.* GCN2 sustains mTORC1 suppression upon amino acid deprivation by inducing Sestrin2. *Genes Dev.* **29**, 2331–2336 (2015).

104. Chantranupong, L. *et al.* The CASTOR Proteins Are Arginine Sensors for the mTORC1 Pathway. *Cell* **165**, 153–164 (2016).

105. Jewell, J. L. *et al.* Differential regulation of mTORC1 by leucine and glutamine. *Science* **347**, 194–198 (2015).

106. Liu, P. *et al.* Sin1 phosphorylation impairs mTORC2 complex integrity and inhibits downstream Akt signalling to suppress tumorigenesis. *Nat. Cell Biol.* **15**, 1340–1350 (2013).

107. Yang, G., Murashige, D. S., Humphrey, S. J. & James, D. E. A Positive Feedback Loop between Akt and mTORC2 via SIN1 Phosphorylation. *Cell Rep.* **12**, 937–943 (2015).

108. Hsu, P. P. *et al.* The mTOR-Regulated Phosphoproteome Reveals a Mechanism of mTORC1-Mediated Inhibition of Growth Factor Signaling. *Science* **332**, 1317–1322 (2011).

109. Shah, O. J. & Hunter, T. Turnover of the Active Fraction of IRS1 Involves Raptor-mTOR- and S6K1-Dependent Serine Phosphorylation in Cell Culture Models of Tuberous Sclerosis. *Mol. Cell. Biol.* **26**, 6425–6434 (2006).

110. Murphy, B. Embryonic Diapause: Advances in Understanding the Enigma of Seasonal Delayed Implantation. *Reprod. Domest. Anim.* **47**, 121–124 (2012).

111. Douglas, D. A., Song, J.-H., Moreau, G. M. & Murphy, B. D. Differentiation of the Corpus Luteum of the Mink (Mustela vison): Mitogenic and Steroidogenic Potential of Luteal Cells from Embryonic Diapause and Postimplantation Gestation. *Biol. Reprod.* **58**, 1163–1169 (1998).

112. Weitlauf, H. M. & Greenwald, G. S. SURVIVAL OF BLASTOCYSTS IN THE UTERI OF OVARIECTOMIZED MICE. *Reproduction* **17**, 515–520 (1968).

113. Arena, R. *et al.* Lipid droplets in mammalian eggs are utilized during embryonic diapause. *Proc. Natl. Acad. Sci.* **118**, e2018362118 (2021).

114. Bulut-Karslioglu, A. *et al.* Inhibition of mTOR induces a paused pluripotent state. *Nature* **540**, 119–123 (2016).

115. Liu, W. M. *et al.* Let-7 derived from endometrial extracellular vesicles is an important inducer of embryonic diapause in mice. *Sci. Adv.* **6**, eaaz7070 (2020).

116. Kamemizu, C. & Fujimori, T. Distinct dormancy progression depending on embryonic regions during mouse embryonic diapause†. *Biol. Reprod.* **100**, 1204–1214 (2019).

117. Batlle-Morera, L., Smith, A. & Nichols, J. Parameters influencing derivation of embryonic stem cells from murine embryos. *genesis* **46**, 758–767 (2008).

118. Chang, M. C. Reciprocal insemination and egg transfer between ferrets and mink. *J. Exp. Zool.* **168**, 49–59 (1968).

119. Ptak, G. E. *et al.* Embryonic Diapause Is Conserved across Mammals. *PLoS ONE* **7**, e33027 (2012).

120. Wilcox, A. J., Baird, D. D. & Weinberg, C. R. Time of Implantation of the Conceptus and Loss of Pregnancy. *N. Engl. J. Med.* **340**, 1796–1799 (1999).

121. Canton, I. *et al.* Mucin-Inspired Thermoresponsive Synthetic Hydrogels Induce Stasis in Human Pluripotent Stem Cells and Human Embryos. *ACS Cent. Sci.* **2**, 65–74 (2016).

122. Hamatani, T., Carter, M. G., Sharov, A. A. & Ko, M. S. H. Dynamics of Global Gene Expression Changes during Mouse Preimplantation Development. *Dev. Cell* **6**, 117–131 (2004).

123. Scognamiglio, R. *et al.* Myc Depletion Induces a Pluripotent Dormant State Mimicking Diapause. *Cell* **164**, 668–680 (2016).

124. Van Der Weijden, V. A. *et al. Metabolic enhancement of mammalian developmental pausing*. http://biorxiv.org/lookup/doi/10.1101/2022.08.22.504730 (2022) doi:10.1101/2022.08.22.504730.

125. Fu, Z. *et al.* Integral Proteomic Analysis of Blastocysts Reveals Key Molecular Machinery Governing Embryonic Diapause and Reactivation for Implantation in Mice1. *Biol. Reprod.* **90**, (2014).

126. Khoa, L. T. P. *et al.* Histone Acetyltransferase MOF Blocks Acquisition of Quiescence in Ground-State ESCs through Activating Fatty Acid Oxidation. *Cell Stem Cell* **27**, 441-458.e10 (2020).

127. Ahmad, K. & Henikoff, S. Centromeres Are Specialized Replication Domains in Heterochromatin. *J. Cell Biol.* **153**, 101–110 (2001).

128. Hu, C. & Brunet, A. The African turquoise killifish: A research organism to study vertebrate aging and diapause. *Aging Cell* **17**, e12757 (2018).

129. Bulut-Karslioglu, A. *et al.* The Transcriptionally Permissive Chromatin State of Embryonic Stem Cells Is Acutely Tuned to Translational Output. *Cell Stem Cell* **22**, 369-383.e8 (2018).

130. Percharde, M., Bulut-Karslioglu, A. & Ramalho-Santos, M. Hypertranscription in Development, Stem Cells, and Regeneration. *Dev. Cell* **40**, 9–21 (2017).

131. Rodgers, J. T. *et al.* mTORC1 controls the adaptive transition of quiescent stem cells from G0 to GAlert. *Nature* **510**, 393–396 (2014).

132. Houghton, F. D. Energy metabolism of the inner cell mass and trophectoderm of the mouse blastocyst. *Differentiation* **74**, 11–18 (2006).

133. Hussein, A. M. *et al.* Metabolic Control over mTOR-Dependent Diapause-like State. *Dev. Cell* **52**, 236-250.e7 (2020).

134. Sousa, M. I., Correia, B., Rodrigues, A. S. & Ramalho-Santos, J. Metabolic characterization of a paused-like pluripotent state. *Biochim. Biophys. Acta BBA - Gen. Subj.* **1864**, 129612 (2020).

135. Treiber, T., Treiber, N. & Meister, G. Regulation of microRNA biogenesis and its crosstalk with other cellular pathways. *Nat. Rev. Mol. Cell Biol.* **20**, 5–20 (2019).

136. O'Brien, J., Hayder, H., Zayed, Y. & Peng, C. Overview of MicroRNA Biogenesis, Mechanisms of Actions, and Circulation. *Front. Endocrinol.* **9**, 402 (2018).

137. Bartel, D. P. & Chen, C.-Z. Micromanagers of gene expression: the potentially widespread influence of metazoan microRNAs. *Nat. Rev. Genet.* **5**, 396–400 (2004).

138. Meuti, M. E., Bautista-Jimenez, R. & Reynolds, J. A. Evidence that microRNAs are part of the molecular toolkit regulating adult reproductive diapause in the mosquito, Culex pipiens. *PLOS ONE* **13**, e0203015 (2018).

139. Hou, L. *et al.* MicroRNA-125a-3p downregulation correlates with tumorigenesis and poor prognosis in patients with non-small cell lung cancer. *Oncol. Lett.* **14**, 4441–4448 (2017).

140. Olejniczak, M., Kotowska-Zimmer, A. & Krzyzosiak, W. Stress-induced changes in miRNA biogenesis and functioning. *Cell. Mol. Life Sci.* **75**, 177–191 (2018).

141. Pabit, S. A. *et al.* Elucidating the Role of Microprocessor Protein DGCR8 in Bending RNA Structures. *Biophys. J.* **119**, 2524–2536 (2020).

142. Wang, Y., Medvid, R., Melton, C., Jaenisch, R. & Blelloch, R. DGCR8 is essential for microRNA biogenesis and silencing of embryonic stem cell self-renewal. *Nat. Genet.* **39**, 380–385 (2007).

143. Bernardi, R. *et al.* PML regulates p53 stability by sequestering Mdm2 to the nucleolus. *Nat. Cell Biol.* **6**, 665–672 (2004).

144. Paquette, A. G. *et al.* Distinct communication patterns of trophoblastic miRNA among the maternal-placental-fetal compartments. *Placenta* **72–73**, 28–35 (2018).

145. Thamotharan, S. *et al.* Differential microRNA expression in human placentas of term intra-uterine growth restriction that regulates target genes mediating angiogenesis and amino acid transport. *PLOS ONE* **12**, e0176493 (2017).

146. Galagali, H. & Kim, J. K. The multifaceted roles of microRNAs in differentiation. *Curr. Opin. Cell Biol.* **67**, 118–140 (2020).

147. Recent Molecular Genetic Explorations of Caenorhabditis elegans MicroRNAs. *Genetics* (2018) doi:10.1534/genetics.118.300291.

148. Bhadra, M., Howell, P., Dutta, S., Heintz, C. & Mair, W. B. Alternative splicing in aging and longevity. *Hum. Genet.* **139**, 357–369 (2020).

149. Raben, N. & Puertollano, R. TFEB and TFE3: Linking Lysosomes to Cellular Adaptation to Stress. *Annu. Rev. Cell Dev. Biol.* **32**, 255–278 (2016).

150. Martina, J. A., Diab, H. I., Brady, O. A. & Puertollano, R. TFEB and TFE 3 are novel components of the integrated stress response. *EMBO J.* **35**, 479–495 (2016).

151. Woll, S. C. & Podrabsky, J. E. Insulin-like growth factor signaling regulates developmental trajectory associated with diapause in embryos of the annual killifish *Austrofundulus limnaeus*. *J. Exp. Biol.* jeb.151373 (2017) doi:10.1242/jeb.151373.

152. Pierce, S. B. *et al.* Regulation of DAF-2 receptor signaling by human insulin and *ins-1* , a member of the unusually large and diverse *C. elegans* insulin gene family. *Genes Dev.* **15**, 672–686 (2001).

153. Ciarmela, P. *et al.* Growth factors and myometrium: biological effects in uterine fibroid and possible clinical implications. *Hum. Reprod. Update* **17**, 772–790 (2011).

154. Peng, L. *et al.* Expression of insulin-like growth factors (IGFs) and IGF signaling: molecular complexity in uterine leiomyomas. *Fertil. Steril.* **91**, 2664–2675 (2009).

155. Lighten, A. D., Moore, G. E., Winston, R. M. & Hardy, K. Routine addition of human insulin-like growth factor-I ligand could benefit clinical in-vitro fertilization culture. *Hum. Reprod.* **13**, 3144–3150 (1998).

156. Reddington, J. P. *et al.* Redistribution of H3K27me3 upon DNA hypomethylation results in de-repression of Polycomb target genes. *Genome Biol.* **14**, R25 (2013).

157. Chondrogianni, N., Georgila, K., Kourtis, N., Tavernarakis, N. & Gonos, E. S. 20S proteasome activation promotes life span extension and resistance to proteotoxicity in *Caenorhabditis elegans*. *FASEB J.* **29**, 611–622 (2015).

158. Park, S. H., Choi, W. H. & Lee, M. J. Effects of mTORC1 inhibition on proteasome activity and levels. *BMB Rep.* **55**, 161–165 (2022).

159. Venturini, V. *et al.* The nucleus measures shape changes for cellular proprioception to control dynamic cell behavior. *Science* **370**, eaba2644 (2020).

160. Xu, X. *et al.* Piezo Channels: Awesome Mechanosensitive Structures in Cellular Mechanotransduction and Their Role in Bone. *Int. J. Mol. Sci.* **22**, 6429 (2021).

161. Clark, A. T. *et al.* Human embryo research, stem cell-derived embryo models and in vitro gametogenesis: Considerations leading to the revised ISSCR guidelines. *Stem Cell Rep.* **16**, 1416–1424 (2021).

162. Cirera-Salinas, D. *et al.* Noncanonical function of DGCR8 controls mESC exit from pluripotency. *J. Cell Biol.* **216**, 355–366 (2017).

163. Paria, B. C., Huet-Hudson, Y. M. & Dey, S. K. Blastocyst's state of activity determines the 'window' of implantation in the receptive mouse uterus. *Proc. Natl. Acad. Sci.* **90**, 10159–10162 (1993).

164. Eakin, G. S. & Hadjantonakis, A.-K. Production of chimeras by aggregation of embryonic stem cells with diploid or tetraploid mouse embryos. *Nat. Protoc.* **1**, 1145–1153 (2006).

165. Friedländer, M. R., Mackowiak, S. D., Li, N., Chen, W. & Rajewsky, N. miRDeep2 accurately identifies known and hundreds of novel microRNA genes in seven animal clades. *Nucleic Acids Res.* **40**, 37–52 (2012).

166. Love, M. I., Huber, W. & Anders, S. Moderated estimation of fold change and dispersion for RNA-seq data with DESeq2. *Genome Biol.* **15**, 550 (2014).

167. Bhattacharya, A. *et al.* An approach for normalization and quality control for NanoString RNA expression data. *Brief. Bioinform.* **22**, bbaa163 (2021).

168. Kulak, N. A., Pichler, G., Paron, I., Nagaraj, N. & Mann, M. Minimal, encapsulated proteomic-sample processing applied to copy-number estimation in eukaryotic cells. *Nat. Methods* **11**, 319–324 (2014).

169. Ni *et al.* Mutations in NDUFS1 Cause Metabolic Reprogramming and Disruption of the Electron Transfer. *Cells* **8**, 1149 (2019).

170. Ritchie, M. E. *et al.* limma powers differential expression analyses for RNA-sequencing and microarray studies. *Nucleic Acids Res.* **43**, e47–e47 (2015).

171. Law, C. W., Chen, Y., Shi, W. & Smyth, G. K. voom: precision weights unlock linear model analysis tools for RNA-seq read counts. *Genome Biol.* **15**, R29 (2014).

172. Liao, Y., Wang, J., Jaehnig, E. J., Shi, Z. & Zhang, B. WebGestalt 2019: gene set analysis toolkit with revamped UIs and APIs. *Nucleic Acids Res.* **47**, W199–W205 (2019).

173. Zhang, X. *et al.* Proteome-wide identification of ubiquitin interactions using UbIA-MS. *Nat. Protoc.* **13**, 530–550 (2018).

174. Kanehisa, M. KEGG: Kyoto Encyclopedia of Genes and Genomes. *Nucleic Acids Res.* **28**, 27–30 (2000).

175. The FANTOM Consortium *et al.* An integrated expression atlas of miRNAs and their promoters in human and mouse. *Nat. Biotechnol.* **35**, 872–878 (2017).

176. Castro-Mondragon, J. A. *et al.* JASPAR 2022: the 9th release of the open-access database of transcription factor binding profiles. *Nucleic Acids Res.* **50**, D165–D173 (2022).

177. Santana-Garcia, W. *et al.* RSAT 2022: regulatory sequence analysis tools. *Nucleic Acids Res.* **50**, W670–W676 (2022).

178. Kaya-Okur, H. S. *et al.* CUT&Tag for efficient epigenomic profiling of small samples and single cells. *Nat. Commun.* **10**, 1930 (2019).

179. Soneson, C., Love, M. I. & Robinson, M. D. Differential analyses for RNA-seq: transcript-level estimates improve gene-level inferences. *F1000Research* **4**, 1521 (2016).

180. Bray, N. L., Pimentel, H., Melsted, P. & Pachter, L. Near-optimal probabilistic RNA-seq quantification. *Nat. Biotechnol.* **34**, 525–527 (2016).

181. Vitting-Seerup, K. & Sandelin, A. The Landscape of Isoform Switches in Human Cancers. *Mol. Cancer Res.* **15**, 1206–1220 (2017).

182. Dobin, A. *et al.* STAR: ultrafast universal RNA-seq aligner. *Bioinformatics* **29**, 15–21 (2013).

183. Garrido-Martín, D., Palumbo, E., Guigó, R. & Breschi, A. ggsashimi: Sashimi plot revised for browser- and annotation-independent splicing visualization. *PLOS Comput. Biol.* **14**, e1006360 (2018).

Appendix

LIST OF REAGENTS

ANTIBODIES			
	Source	*Identifier*	*Final concentration*
NANOG	*ReproCell Tebu bio*	*RCAB002P-F*	*1:100*
CDX2	*Biogenex*	*MU392A-UC*	*1:100*
MBD2	*Abcam*	*ab188474*	*1:1000*
GAPDH	*Cell Signaling*	*2118*	*1:1000*
PML	*Novus / Bio Techne*	*NB100-59787*	*1:200*
SC-35	*Sigma*	*S4045*	*1:2000*
NPM-1	*Invitrogen*	*FC-61991*	*1:400*
DDX6	*Novus / Bio Techne*	*NB200-192*	*1:4000*
CDX2	*Biogenex*	*MU392A-UC*	*1:100*
GAPDH	*Cell Signaling*	*2118*	*1:1000*
Raptor	*Thermo Fisher*	*424000*	*1:1000*
Rictor	*Novus*	*NB100612*	*1:1000*
pS6	*CST*	*4858*	*1:200*
pAKT	*CST*	*4060T*	*1:200*
Ki67	*BD Pharmingen*	*556003*	*1:400*
H3pS10	*Abcam*	*ab5176*	*1:1000*
OCT4	*Santa Cruz*	*Sc5279*	*1:50*
NANOG	*Abcam*	*ab109250*	*1:200*
γH2A.X	*Biolegend*	*613405*	*1:400*
CDX2	*BioGenex*	*MU392-UC*	*1:100*
4EBP1	*CST*	*2855*	*1:100*
Lamin B1	*Abcam*	*ab16048*	*1:100*

GATA3	*R & D*	*AF2605*	*1:200*
Donkey anti-mouse IgG Alexa fluor 680	*Invitrogen*	*A10038*	*1:700*
Donkey anti-mouse IgG highly cross-adsorbed, Alexa fluor plus 488	*Invitrogen*	*A32766*	*1:700*
Donkey anti-rabbit IgG highly cross-adsorbed, Alexa fluor 568	*Invitrogen*	*A10042*	*1:700*
Mouse anti-rabbit-IgG HRP	*Jackson Laboratories*	*211-032-171*	*1:2000*
SuperSignal WestDura	*Thermo Fisher Scientific*	*34075*	
CHEMICALS			
	Source	*Identifier*	*Final concentration*
INK-128	*selleckchem*	*S2811*	*200 nM*
RapaLink-1	*MedChemExpress / Hölzel*	*HY-111373*	*200 nM*
AntimiR-200	*Qiagen*	*339160*	*100 nM*
AntimiR-26b-5p	*Qiagen*	*339130*	*100 nM*
Control antimiR	*Qiagen*	*339136*	*100 nM*
pLKO.1	*Addgene*	*10878*	
pLKO.1-miR92a1	*This study*		
pLKO.1-miR92a2	*This study*		
pLKO.1-miR92b	*This study*		
pCAGGS-EGFP	*Bulut-Karslioglu et al*[77]		
mmu-miR-92a-1-5p	*Applied biosystems*	*mmu481275_mir*	*Taqman probes*
mmu-miR-92a-2-5p	*Applied biosystems*	*mmu482577_mir*	*Taqman probes*
mmu-miR-92a-3p	*Applied biosystems*	*Custom made*	*Taqman probes*
mmu-miR-92b-5p	*Applied biosystems*	*mmu482578_mir*	*Taqman probes*

mmu-miR-92b-3p	*Applied biosystems*	*mmu481277_mir*	*Taqman probes*
mmu-miR-290a-3p	*Applied biosystems*	*mmu481666_mir*	*Taqman probes*
IGF1	*R & D*	*291-G1/CF*	
Matrigel	*Corning*	*354277*	
ROCK inhibitor	*Tocris*	*1254*	*10μM and 5μM*
RSeT^{TM} Feeder-Free Medium	*Stem Cell Technologies*	*05975*	
TrypLE	*Thermo Fisher*	*12604-021*	
PD0325901	*MedChemExpress*	*HY-10254*	*1 μM*
XAV-939	*MedChemExpress*	*HY-15147*	*2 μM*
Gö 6983	*MedChemExpress*	*HY-13689*	*2 μM*
human leukemia inhibitory factor (hLIF)	*in-house made*		*10 ng ml^{-1}*
Rictor siRNA	*Dharmacon , siGenome*	*M-016984-02-0005*	*100nM*
Raptor siRNA	*Dharmacon , siGenome*	*M-004107-01-0005*	*500nM*
Control siRNA	*Dharmacon , siGenome*	*D-001206-14-05*	*100nM and 500nM*
FuGene	*Promega*	*E2311*	
Experimental models: CELL LINES			
	Source		
Wild-type E14 ESCs	*Sarah Kinkley Lab*		
Wild-type TSCs	*Magdalena Zernicka-Goetz Lab*		
Dgcr8 KO ESCs	*Constance Ciaudo Lab*		
E14-EGFP	*This study*		
Dgcr8 KO-EGFP	*This study*		

Zip13k2	*Franz-Josef Müller Lab*		
H9 ES cells	*Austin Smith lab*		
Experimental models: Organisms and Strains			
	Source	*Identifier*	
CD1 (age 8-12 weeks)	*MPIMG*	*030-800129*	
B6D2F1/JRj (age 8-12 weeks)	*Janvier Labs*	*SH-B6D2-F*	
C57Bl/6xCBA	*MPIMG*		
NOG mice (age 6-8 weeks)	*Taconic, Denmark*		
Software and Algorithms			
	Source	*Identifier*	*Version*
Kallisto	*Pachter Lab*	*https://pachterlab.github.io/kallisto/*	kallisto 0.44.0
DESeq2	*Mike Love Lab*		*DESeq2_1.40.2*
IsoformSwitchAnalyzeR	*Veeting-Seerup Lab*		*IsoformSwitchAnalyzeR_2.0.1*
topGO	*Jorg Rahnenführer Lab*		*topGO_2.52.0*
ggsashimi	*Guigo Lab*		

PremiR sequences		
MicroRNA	*Cloned region*	*Sequence cloned*
mmu-miR-92a-1	*chr 14: 115044427-115044506 [+]*	*GTAGAGAAGTAAGGGAAAATCAAACCC**CTTTCTACACAGGTTGGGATTTG TCGCAATGCTGTGTTTCTCTGTATGGTATTGCACT TGTCCCGGCCTGTTG AGTTTGG**TGGGGATTGTGACCAGAAGATGTGAAAAT GACAATATTGCTGA A*
mmu-miR-92a-2	*chr X: 52741838-52741928 [-]*	*CTGCATCGTAATGGACACCTTTATGCACATCTTCAGC ATCCA**TGCCCATTCATCCACAGGTGGGGATTGGTG GCATTACTTGTGTTAGATATAAAGTATTGCACTTG TCCCGGCCTGAGGAAGAAAGAGGGTT**TTTAATCGT CTTTTAGTTTCTGAGTATTGTAAGTTATGTTAGACTGT A*

mmu-miR-92b	*chr3: 89227116-89227198 [-]*	*CAGGCTCTGGCGCACCTCTAAGGTGACCTATACTCC CCAGAGCACTCCAGTCCCTGGGTTCCAGCGGCCCA GGTGGTTAGGGAGCGGGATTCCAGAGCCCC**GGGTG GGCGGGAGGGACGGGACGTGGTGCAGTGTTGTTC TTTCCCCTGCCAATATTGCACTCGTCCCGGCCTCC GGCCCCCTCG**GCCCCCCCGGCGCCCCCTCACCCAG AGTGGGGCAGC*

Isoform specific primers	
Mbd2a fwd	*5'-GTAAACCAGACCTGAACACAAC-3'*
Mbd2b rev	*5'-CTGACGTGGTTGTTCATTCATC-3'*
Mbd2c fwd	*5'-CTGGACCACTTGCTCGCTCC-3'*
Mbd2c rev	*5'-GTCCTTGCTCTCCTGGAGCTC-3'*
Atn1 fwd	*5'-GAATACGCCCGACCTCATGTC-3'*
Atn1 rev	*5'-GCCACCCTTTCTGCATGCTG-3'*
Ubr2 fwd	*5'-AGGGACTGATAAAAGTCATTTC-3'*
Ubr2 rev	*5'-TGGTGGACAGCCAGCAAGCT-3'*
Nfat5 fwd	*5'-TGCCAAAGCAAGCACCGTGC-3'*
Nfat5 rev	*5'-GTGCACTTACTTTCCCAAGC-3'*
Wipi2 fwd	*5'-GTAGCTAAATCTGCTGAGGT-3'*
Wipi2 rev	*5'-CTCCTCGGATGCTCCAGGGC-3'*
Tmem135 fwd	*5'-ACAATGTATTTCAAGGGCATCG-3'*
Tem135 rev	*5'-CTGCCCTTGGTGAGCCTTAA-3'*
Fis1 fwd	*5'-GGGCCTCCACAGGTCGATGC-3'*
Fis1 rev	*5'-GGCCGCCGCCCCTGAAAGCC-3'*
Opa1 fwd	*5'-GTTCAGGTGCTCAAATATACAC-3'*
Opa1 rev	*5'-GTTCATGCTGCACACAGACT-3'*
Retreg1 fwd	*5'-ATGGCGAGCCCGGCGCCCGAG-3'*
Retreg1 rev	*5'-CTCCCGGCGGCCTCCTCCACC-3'*